Self-sensing Algorithms for Active Magnetic Bearings

Thesis submitted for the degree Doctor of Philosophy

at the Potchefstroom campus of the North-West University

Andries C. Niemann

Promoter: Prof. G. van Schoor

November 2008

Declaration

I hereby declare that all the material incorporated in this thesis is my own original unaided work except where specific reference is made by name or in the form of a numbered reference. The word herein has not been submitted for a degree at another university.

Signed:

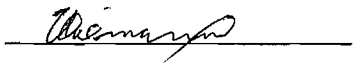

A.C. Niemann

Foreword

I want to thank my lovely wife Elna for all her love and support, without you I could not have persevered. To my family, my sincere thanks for your support and encouragement.

I want to thank my promoter Prof. George van Schoor for his guidance and support.

Thanks to M-Tech industrial who made this project available and their funding through THRIP.

Special thanks to Jacques for his help on the programming during the practical implementation and to Eugén, Pieter, Kenny and all who helped and supported me during this period.

Die wysheid sal sy plek in jou lewe inneem, kennis sal vir jou iets aangenaams word, oordeelkundigheid sal oor jou wag hou en verstandigheid sal jou bewaak.

Spreuke 2:10

Abstract

Active magnetic bearings (AMBs) have become a key technology in industrial applications with a continued drive for cost reduction and an increase in reliability. AMBs require position feedback to suspend the rotor. Conventional contactless position sensors are used to measure the rotor's position. The major disadvantages of conventional position sensors are their cost and that the sensors are viewed as a weak point in an AMB system. A self-sensing sensor is a type of sensor which is cost effective, reduces sensor wire-length and increases reliability, thus ideal for the industry. This type of sensor relies on the current and voltage signals of the AMB's to obtain the rotor position. Due to the rapid and advanced development of digital electronics, it has become more powerful and cheaper, thus self-sensing in mass production will be cost effective. Different self-sensing approaches were developed in the past and can be divided into two main categories: state estimation and amplitude modulation approaches. In this research the focus will be on the amplitude modulation approach. Amplitude modulation makes use of two signals, namely the modulation signal and the carrier signal. In a self-sensing AMB system the carrier can be a high frequency component injected into the system or the switching ripple of the switch mode power amplifier can be used. The modulation signal is the change in rotor position which results in changing inductances. The actuator material introduces nonlinear effects on the estimated position. Due to these nonlinear effects, it is rather difficult to obtain the rotor position. The first industrial application of a self-sensing turbomolecular pump system was implemented in 2005 by S2M. The aim of this thesis is to evaluate existing self-sensing schemes, devise improvements and investigate possible new schemes. Four different demodulation methods and two new self-sensing schemes are evaluated. An AMB transient simulation model which includes saturation, hysteresis, eddy currents and cross-coupling is used to evaluate the schemes in simulation. The self-sensing schemes are implemented in hardware and evaluated on a 7 A rms 500 N AMB. A comparative study was done on the different self-sensing schemes. From the comparative study it was determined that the gain- and phase effects have a direct effect on the sensitivity of the system. It was also proved that self-sensing can be implemented on a coupled AMB with a sensitivity of 10.3 dB.

Keywords: *Self-sensing, sensorless sensor, demodulation, AMB, inductive sensing, bi-state switched mode power amplifier.*

Opsomming

Aktiewe magnetiese laers (AMLs) word 'n belangrike tegnologiese komponent in industriële toepassings met 'n kontinue dryf vir kosteverlaging en 'n verhoging in betroubaarheid. AMLs vereis posisie terugvoer om suksesvolle suspendering te bewerkstellig. Konvensionele kontaklose posisiesensors word gebruik om posisie-inligting te verkry. Die grootste nadeel van konvensionele posisiesensors is hul koste en die feit dat die sensors as 'n swakpunt in die AML stelsel beskou word. 'n Selfwaarnemende sensor is 'n tipe sensor wat koste-effektief is, sensor draadlengte verminder en betroubaarheid verbeter. Dit is dus ideaal vir gebruik in die industrie. Hierdie tipe sensor maak gebruik van die stroom- en spanningseine van die AMLs om die posisie van die rotor te bepaal. As gevolg van die vinnige en gevorderde onwikkeling van digitale elektronika het dit kragtiger en goedkoper geword. Selfwaarnemende sensors sal dus meer koste effektief wees met massa-produksie. Verskillende selfwaarnemende sensor benaderings is ontwikkel in die verlede, en kan verdeel word in twee hoof kategorieë: toestandskatting en amplitudemodulasie. In hierdie navorsing word gefokus op die amplitudemodulasie benadering. Amplitudemodulasie maak gebruik van twee seine, naamlik die modulasiesein en die draersein. In 'n selfwaarnemende AML stelsel kan die draersein 'n hoë-frekwensie komponent wees wat in die stelsel gesuperponeer word, of die skakelrippel van die kragversterkers kan gebruik word. Die modulasiesein is die verandering in die rotorposisie wat induktansie veranderinge tot gevolg het. Die aktueerdermateriaal veroorsaak nie-lineêre effekte op die geskatte posisie wat dit taamlik moeilik maak om die rotor posisie te bepaal. Die eerste industriële toepassing is 'n selfwaarnemende turbo-molekulêre pompstelsel wat in 2005 deur S2M geïmplementeer is. Die doel van die tesis is om bestaande selfwaarnemende skemas te evalueer, verbeterings aan te bring en moontlike nuwe skemas te ondersoek. Vier verskillende demodulasietegnieke en twee nuwe skemas is ge-evalueer. 'n AML transiënte simulasiemodel wat versadiging, histerese, werwelstrome en kruiskoppeling insluit, is gebruik om die skemas te evalueer in simulasie. Die selfwaarnemende skemas is geïmplementeer in hardeware en ge-evalueer op 'n 7 A wgk 500 N AML. 'n Vergelykende studie is gedoen op die verskillende skemas. Vanuit hierdie studie is bevind dat die wins en fase-effekte 'n direkte invloed het op die sensitiwiteit van die stelsel. Dit is ook bewys dat selfwaarneming geïmplementeer kan word op 'n gekoppelde AML met 'n sensitiwiteit van 10.3 dB.

Contents

Foreword ii

Abstract iv

Opsomming v

List of figures xvi

List of tables xvii

List of symbols xvii

List of Abbreviation xxi

1 Introduction 1

1.1 Motivation 1

1.2 Basic background 2

1.3 Areas of contribution 2

1.3.1 Simulation platform 3

1.3.2 Self-sensing configurations 3

1.3.3 Robustness analysis 3

1.3.4 Hardware platform 3

1.4 Problem statement 4

1.5 Research aims and objectives 4
1.6 Research methodology 5
1.7 Contribution of research 6
1.8 Overview of thesis 6

2 Background **8**
2.1 Active magnetic bearings 8
2.2 Magnetic bearing characteristics and applications 11
2.2.1 Advantages 11
2.2.2 Disadvantages 11
2.2.3 Applications 11
2.3 Position sensing 12
2.4 Self-sensing methods 12
2.4.1 State estimation 13
2.4.2 Frequency modulation 13
2.4.3 Amplitude modulation 14
2.5 Self-sensing robustness 15
2.6 Nonlinearities 16
2.6.1 Saturation 16
2.6.2 Cross-coupling 16
2.6.3 Eddy currents 17

3 Self-sensing schemes **19**
3.1 Basic actuator model 19
3.2 Drive and switching waveform 21
3.3 Self-sensing based on Schammass's work 23
3.3.1 Modelling 23

3.4 Demodulation methods 28
3.4.1 Analog demodulation method 28
3.4.2 Digital filtering demodulation method 31
3.4.3 Band-pass sampling demodulation method 32
3.4.4 Fast Fourier Transform (FFT) demodulation method 34
3.5 The gradient self-sensing approach 37
3.5.1 Linear model 37
3.5.2 Nonlinearities 39
3.5.3 Implementation limits 40
3.6 Direct current amplitude measurement method 41
3.6.1 Motivation 41
3.6.2 Direct current measurement 41
3.6.3 Scaling and nonlinear compensation 43
3.7 Performance limitations of the DCM technique 44
3.7.1 Current sensing and digitization 44
3.7.2 Dynamic effect due to sensing cycle 46
3.8 Self-sensing algorithm stability 47
3.8.1 Self-sensing loop linearization 47
3.8.2 Algorithm stability 48
3.9 Cross-coupling 49
3.9.1 Reluctance model 49
3.9.2 Cross-coupling due to flux distribution 49
3.9.3 Cross-coupling due to duty cycle variation 50

4 Self-sensing evaluation in simulation **54**

4.1 Transient AMB model 54

4.1.1 Hysteresis and saturation model 55
4.1.2 Eddy currents 56
4.1.3 Magnetic paths 56
4.2 Magnetic bearing specifications 57
4.3 Nonlinear model identification and scaling 58
4.3.1 Nonlinear model identification 58
4.3.2 Scaling 59
4.4 Self-sensing performance evaluation 59
4.4.1 Static evaluation 59
4.4.2 Dynamic evaluation 60
4.5 Controllers 61
4.6 Self-sensing simulation and evaluation results 63
4.6.1 Analog demodulation method 63
4.6.2 Digital demodulation method 69
4.6.3 Band-pass sampling demodulation method 74
4.6.4 Fast Fourier Transform (FFT) demodulation method 81
4.6.5 Gradient method 85
4.6.6 Direct current measurement method 92
4.6.7 Cross-coupling 98
4.6.8 Overview of results 102

5 Hardware implementation **106**

5.1 Integrated power amplifier 106
5.1.1 Power electronics 106
5.1.2 Digital electronics 108
5.1.3 Analog electronics 109

5.2 Digital demodulation method 111
5.2.1 Demodulation 112
5.2.2 Nonlinear model identification 112
5.2.3 Static evaluation 113
5.2.4 Controller parameters 115
5.2.5 Dynamic evaluation 115
5.3 Direct current measurement technique 116
5.3.1 Signal conditioning 117
5.3.2 Nonlinear model identification 119
5.3.3 Static evaluation 120
5.3.4 Controller parameters 120
5.3.5 Dynamic evaluation 122
5.3.6 Cross-coupling 125

6 Conclusions and recommendations **132**
6.1 Summary 132
6.2 Unique contributions 133
6.3 Future work 134
6.4 Closure 134

A Cross-coupling **140**

List of Figures

2.1 AMB current and position to force relation 9

2.2 Basic AMB system 9

2.3 Differential driving mode 10

2.4 State estimation scheme 13

2.5 Frequency modulation scheme 14

2.6 Basic amplitude modulation self-sensing scheme 15

3.1 Eight pole AMB system [1] 20

3.2 Basic actuator model 20

3.3 Current waveform due to switch mode power amplifier 22

3.4 Amplitude variation due to changing duty cycle 22

3.5 Amplitude modulation method 23

3.6 Frequency shifted model 24

3.7 Inverse frequency shifted model block diagram 27

3.8 Demodulation process 28

3.9 Modulated current 29

3.10 Phase shift due to BPF 29

3.11 Phase shift due to LPF 30

3.12 Digitization process 31

3.13 Sampling of analog signal 31

3.14 Band-pass sampling method 33
3.15 FFT demodulation method 34
3.16 Current ripple with low frequency control current 35
3.17 FFT with and without detrending 36
3.18 256 and 7 point detrending 37
3.19 Sampled gradient 38
3.20 Hysteresis loops 39
3.21 Gradient self-sensing technique 40
3.22 Position sensing and control cycle 43
3.23 High frequency ripple component 43
3.24 Block diagram of DCM self-sensing technique 44
3.25 Current sensor output 45
3.26 Low frequency elimination methods 46
3.27 Self-sensing algorithm block diagram 48
3.28 Reluctance network 50
3.29 Reluctance gain evaluation: x-axis 51
3.30 Reluctance gain evaluation: y-axis 52

4.1 Eddy current magnetic model 56
4.2 Actuator flux path model 57
4.3 Switching waveforms 58
4.4 Simplified AMB system 61
4.5 Controller block diagram 62
4.6 PID input filter response 62
4.7 PI current controller 63
4.8 Block diagram of the analog demodulation self-sensing scheme 64
4.9 Analog BPF frequency response 64

4.10 LPF effect due to BPF 65
4.11 Demodulator LPF 65
4.12 $G_d(z)$ frequency response: Analog demodulation method 66
4.13 Nonlinear effects on self-sensing scheme 67
4.14 Nonlinear compensated output 67
4.15 Static evaluation: Analog method 68
4.16 Gain and phase response: Analog demodulation method 69
4.17 Sensitivity plot: Analog method 70
4.18 Block diagram of the digital demodulation self-sensing scheme 70
4.19 Frequency response of FIR LPF 71
4.20 $G_d(z)$ frequency response: Digital demodulation method 72
4.21 Nonlinear effects on self-sensing scheme 72
4.22 Nonlinear compensated output 73
4.23 Static evaluation: Digital method 74
4.24 Gain and phase response: Digital method 75
4.25 Sensitivity plot: Digital method 75
4.26 Block diagram of the band-pass sampling demodulation self-sensing scheme 76
4.27 Frequency response of band-pass sampling demodulation method with out BPF 77
4.28 $G_d(z)$ frequency response: Band-pass sampling demodulation method . 77
4.29 Nonlinear effects on self-sensing scheme 78
4.30 Nonlinear compensated output 78
4.31 Static evaluation 79
4.32 Gain and phase response: Band-pass sampling method 80
4.33 Sensitivity plot: Band-pass sampling method 80

4.34 Block diagram of the FFT demodulation self-sensing scheme which makes use of digital detrending 81

4.35 Frequency response of FFT modelling transfer function 83

4.36 $G_d(z)$ frequency response: FFT with BPF demodulation method 84

4.37 $G_d(z)$ frequency response: FFT with detrending demodulation method . 85

4.38 Nonlinear effects on self-sensing scheme: Band-pass filtered 85

4.39 Nonlinear effects on self-sensing scheme: Detrended 86

4.40 Nonlinear compensated output: Band-pass filtered 86

4.41 Nonlinear compensated output: Detrended 87

4.42 Static evaluation: Band-pass filtered FFT method 87

4.43 Static evaluation: Detrended FFT method 88

4.44 Gain and phase response: FFT method 88

4.45 Sensitivity plot: FFT method 89

4.46 Block diagram of the gradient self-sensing scheme 89

4.47 Frequency response of sample and hold 90

4.48 Nonlinear effects on self-sensing scheme 90

4.49 Nonlinear compensated output 91

4.50 Static evaluation: Gradient method 92

4.51 Gain and phase response: Gradient method 93

4.52 Sensitivity plot: Gradient method 93

4.53 Block diagram of the DCM self-sensing scheme 94

4.54 8^{th} order noise reduction FIR filter 95

4.55 Nonlinear effects on self-sensing scheme 95

4.56 Nonlinearity due to saturation 96

4.57 Nonlinear compensated output 97

4.58 Static evaluation: DCM method 97

4.59 Frequency response of PID derivative path filter 98

4.60 Gain and phase response: DCM method 99

4.61 Sensitivity plot: DCM method 99

4.62 Cross-coupling effect on top coil: Analog demodulation self-sensing scheme, bottom coil excited with 2 A, 200 Hz current reference 100

4.63 Cross-coupling effect on top coil: Analog demodulation self-sensing scheme, bottom coil excited with 2 A, 500 Hz current reference 101

4.64 Amplitude dependency: Cross-coupling effect on top coil with bottom coil excited with 100 Hz (left) and 200 Hz (right) and constant duty cycle variation in bottom coil 101

4.65 Cross-coupling effect on top coil: Analog demodulation self-sensing scheme, left horizontal coil excited with 2 A, 500 Hz current reference 102

4.66 Cross-coupling effect on top coil: DCM self-sensing scheme, bottom coil excited with 2 A, 200 Hz current reference 103

4.67 Cross-coupling effect on top coil: DCM self-sensing scheme, bottom coil excited with 2 A, 500 Hz current reference 103

4.68 Cross-coupling effect on top coil: DCM self-sensing scheme, left horizontal coil excited with 2 A, 500 Hz current reference 104

5.1 Integrated power amplifier 107

5.2 Power electronics block diagram 107

5.3 Power electronics board 108

5.4 Block diagram of digital electronics circuit 109

5.5 Digital electronics board 110

5.6 Block diagram of analog board 111

5.7 Self-sensing analog implementations methods 111

5.8 Analog electronics board 112

5.9 FIR filter frequency response 113

5.10 Nonlinearity due to saturation 113

5.11 Nonlinear compensated output 114

5.12 Static evaluation: Digital filtering method 114
5.13 FFT of estimated position with static rotor suspension 115
5.14 Gain and phase response: FIR demodulation method 116
5.15 Sensitivity plot: Digital demodulation method 117
5.16 Sample and hold circuit 117
5.17 Hardware output of amplified sample and hold circuit 118
5.18 Hardware output of amplified sample and hold circuit 119
5.19 Nonlinearity due to saturation 119
5.20 Nonlinear compensated output 120
5.21 Static evaluation: DCM method 121
5.22 Frequency response of PID input filter 122
5.23 FFT of estimated position with static rotor suspension 123
5.24 Gain and phase response: DCM method $Kp = 10000$ 123
5.25 Gain and phase response: DCM method $Kp = 12000$ 124
5.26 Gain and phase response: DCM method $Kp = 10000$ 124
5.27 Sensitivity plot: DCM method 125
5.28 Sensitivity plot: DCM method 125
5.29 FFT of real and estimated position 126
5.30 Sensitivity plot of coupled and decoupled stator 127
5.31 Cross-coupling due to 2 A 130 Hz current reference 128
5.32 Cross-coupling due to 3.5 A 130 Hz current reference 129
5.33 Cross-coupling due to 5 A 130 Hz current reference 129
5.34 Cross-coupling due to 5 A 160 Hz current reference 130
5.35 Cross-coupling due to 5 A 210 Hz current reference 130

A.1 Reluctance network 140

List of Tables

4.1 Hysteresis model constants 55

4.2 Practical model specifications 58

4.3 Sensitivity classification 61

4.4 Control constants: Analog scheme 69

4.5 Control constants: Digital method 74

4.6 Control constants: Band-pass sampling method 79

4.7 Control constants: Gradient method 91

4.8 Control constants: DCM method 98

4.9 Self-sensing schemes benchmarking 105

5.1 Power amplifier capabilities 108

5.2 Control constants: Digital demodulation method 115

5.3 Control constants: DCM method 121

5.4 Phase effects due to filter order 126

5.5 Cross-coupling measurement 127

List of symbols

Latin symbols

A	Cross-sectional area of flux path	[m^2]
A_P	Cross-sectional area of pole	[m^2]
A_R	Cross-sectional area of rotor	[m^2]
A_S	Cross-sectional area of stator back iron	[m^2]
B	Flux density	[T]
B_e	Estimated flux density	[T]
$E(\omega)$	Frequency response error component	
F_s	Sampling frequency	[Hz]
$F(s)$	Estimated frequency response of FFT	
f_a	Aliasing frequency	[Hz]
f_c	Cutoff frequency	[Hz]
f_m	Actuator force	[N]
g	Gravity of earth	[m/s]
g_0	Nominal air gap length	[m]
$G_S(S)$	Sensitivity function	
$G_x(\omega)$	Frequency response ratio of estimated to real position	
$h(k)$	Digital filter coefficients	
$H(z)$	Digital filter transfer function	
i_1	Current flowing through top vertical coil	[A]
i	Current flowing through coil	[A]
i_0	Constant operating current	[A]
$\underline{I_d}$	Demodulated current	[A]
i_L	Low frequency control current	[A]
I_r	Extracted ripple component from sensing cycle	[A]
I_{sense}	Sensing cycle forced to 50 % duty cycle	[A]
$\underline{I_u}$	Demodulated current divided by demodulated voltage	[S]
K_p	Position controller proportional gain	
$K_{p_{AMP}}$	Power amplifier controller proportional gain	
K_d	Position controller derivative gain	

k_x	Position scaling constant	
L_0	Nominal coil inductance	[H]
L_s	Leakage inductance of coil	[H]
l_m	Material path length	[m]
l_P	Pole path length	[m]
l_R	Rotor path length	[m]
l_S	Stator's back iron path length	[m]
m	Mass of the rotor	[kg]
N	Number of coil turns	
R	Coil resistance	[Ω]
r_eC	Eddy current coil resistance	[Ω]
l	Mean length of magnetic material	[m]
l_{lam}	Lamination thickness	[m]
l_{stack}	Total laminated material thickness	[m]
S	Number of delayed samples	
T_1	FFT window width	[s]
T_2	Interval of FFT evaluation	[s]
u	Voltage across the coil	[V]
u_0	Low frequency voltage applied to coil	[V]
$\underline{U_d}$	Demodulated voltage	[V]
u_z	High frequency voltage applied to coil	[V]
V_1	Voltage across top vertical coil	[V]
V_{coil}	Voltage applied to coil	[V]
V_s	Power amplifier switching voltage	[V]
w	Lamination width	[m]
$X(\omega)$	Real position frequency response	
$X_e(\omega)$	Estimated position frequency response	
$X_{ref}(\omega)$	Frequency response reference position	
x	Change in rotor position from nominal position	[m]
x_{ge}	Estimated position without nonlinear compensation (x-axis)	[m]
x_{est}	Scaled estimated position (x-axis)	[m]
x_m	Estimated position due to nonlinear effects (x-axis)	[m]
y_{ge}	Estimated position without nonlinear compensation (y-axis)	[m]
y_{est}	Scaled estimated position (y-axis)	[m]
y_m	Estimated position due to nonlinear effects (y-axis)	[m]

Greek symbols

α	Amplifier duty cycle	
δ	Skin depth	[m]
θ	Phase shift	[degree]
μ_0	Permeability free space	[H/m]
μ_r	Relative permeability of material	
ρ	Resistivity of magnetic material	[Ωm]
ϕ	Magnetic flux	[Wb]
ϕ_1	Flux flowing through top vertical pole	[Wb]
ϕ_{ec}	Flux linked to eddy current coil	[Wb]
ω_s	Power amplifier switching frequency	[rad/s]
$\Re$	Total reluctance trough material and air gap	[H^{-1}]
$\Re_g$	Air gap reluctance	[H^{-1}]
$\Re_m$	Material path reluctance	[H^{-1}]
$\Re_P$	Pole path reluctance	[H^{-1}]
$\Re_S$	Stator back iron reluctance	[H^{-1}]
$\Re_R$	Rotor path reluctance	[H^{-1}]

List of abbreviations

ac	Alternating current
ADC	Analog to digital converter
AMB	Active magnetic bearing
BPF	Band-pass filter
DAC	Digital to analog converter
dc	Direct current
DCM	Direct current measurement
DSP	Digital signal processing
FFT	Fast Fourier transform
FIR	Finite impulse response
FPGA	Field programmable gate array
FWR	Full wave rectifier
IIR	Infinite impulse response
LP	Linear periodic
LPF	Low-pass filter
LTI	Linear time invariant
PID	Proportional integral derivative
PWM	Pulse width modulation
rms	Root mean square
TSM	Transient simulation model
ZOH	Zero-order hold

Chapter 1

Introduction

The human race is constantly evolving such that the search for new technology is a necessity. In industry active magnetic bearings (AMBs) is one such technology.

1.1 Motivation

Currently the field of active magnetic bearings (AMBs) is intensively researched to obtain the full potential of these magnetic bearing systems. AMBs are not new, since the first suspension was obtained as early as 1937 where electromagnetic forces and sensor feedback were applied [2].
Due to the increase in demand for high speed industrial applications such as turbo machines, vacuum pumps and blowers, the bearing systems are pushed to their limits. The characteristics of AMBs are ideal for these high speed applications and thus industrialization of AMBs is on the increase.

The major disadvantage of AMBs is the initial cost due to their complexity. Another disadvantage of AMBs is reliability, since the AMB consists of many subsystems which are usually placed far apart. If some of these subsystems can be eliminated or integrated the cost can be reduced and reliability increased. One such subsystem that has been identified is the position sensors used as rotor position feedback.

Most AMB systems employ conventional contactless position sensors, which usually make use of optical, inductive, eddy currents or capacitive measurement methods [3]. The position sensors used in an AMB system are one of the most critical and expensive subcomponents. By replacing these sensors with a self-sensing scheme, costs can be reduced and reliability increased.
Self-sensing uses the current and voltage signals of the power amplifier to estimate the rotor's position. Self-sensing techniques form an integrated part of the power ampli-

fier which results in a compact design and an increase in reliability. Due to the rapid and advanced development of digital electronics, processors and controllers have become more powerful and cheaper. Self-sensing implemented in mass production will therefore become more cost-effective. Another advantage of self-sensing is that the sensor-wiring is reduced and the sensor is not located inside the mechanical system. This reduces wiring cost and further increases reliability.

1.2 Basic background

Different self-sensing techniques are available from literature, but from their results it was found that the implementation of these self-sensing schemes is cumbersome. The only company currently able to implement a self-sensing AMB system for an industrial application is S2M [4].
Self-sensing can be divided into two groups, namely state estimation and modulation [5]. The state estimation approach make use of an observer to estimate the rotor position. The inputs to the observer are the current and voltage signals of the AMB system. In the case of the amplitude modulation approach, a component of the current signal is modulated by the changing position of the rotor. This amplitude modulated current component is at a much higher frequency than the AMB's bandwidth, so it does not affect the operation of the AMB. The rotor position is obtained by isolating the high frequency component and by passing the signal through a demodulation process.
The high frequency amplitude modulated current component is usually isolated by means of a band-pass filter (BPF). The isolated signal is passed through a synchronous demodulator and then passed through a low-pass filter to shift the high frequencies to low frequencies. The output of the demodulator is the rotor's position if all nonlinearities are neglected.
In most cases the demodulation process is done by analog electronics, but in some cases digital processors are used to assist with the demodulation process and to compensate for nonlinearities. In this research the self-sensing schemes rely mostly on digital demodulation methods and are defined as self-sensing algorithms.
These self-sensing algorithms will be evaluated on an AMB system which includes magnetic coupling between one pole to another through the stator's back iron. In AMB research magnetic coupling through the back iron is also known as cross-coupling.

1.3 Areas of contribution

In a self-sensing AMB system the following four areas were identified for possible contributions: 1) A nonlinear simulation platform on which the self-sensing schemes can be evaluated, 2) different self-sensing configurations to enhance performance, 3)

stability analysis to obtain a theoretical understanding of the overall AMB system robustness limitations and 4) a hardware platform on which the self-sensing schemes can be practically implemented and evaluated.

1.3.1 Simulation platform

An accurate simulation platform is required to evaluate the feasibility of specific self-sensing schemes before hardware development can be initiated. By evaluating the feasibility of the different self-sensing schemes in simulation, hardware development costs can be reduced and a more theoretical approach can be followed. New nonlinear compensation methods can also be evaluated in simulation to evaluate feasibility for real-time implementations [5].

1.3.2 Self-sensing configurations

A self-sensing scheme must be found to minimize the phase effects on the estimated position since it affects the performance of the self-sensing AMB system.

New self-sensing algorithms may also be derived with the aim to increase sensor sensitivity by implementing a new nonlinear compensation method [5].

A new self-sensing scheme must be developed to measure axial bearing position, since position sensitivity is low due to the unlaminated rotor material [5].

1.3.3 Robustness analysis

Self-sensing robustness analysis is another contribution in the self-sensing field. By using linear AMB models the theoretical robustness is much lower than practically obtained [5], [6]. According to Maslen *et al* [7], the higher robustness can be explained by linear periodic signals.

1.3.4 Hardware platform

A high performance hardware platform must be established to implement and evaluate different self-sensing schemes. Some of the self-sensing schemes may be computationally intensive due to high bandwidth models and algorithm complexity and thus it may place high processing demand on the hardware platform.

A self-sensing hardware platform should be designed to form a reliable integrated package which can be used in industry.

The current sensing method forms a critical component of the hardware design. In some self-sensing cases, in-house transformer technology is used to sense the current [5], [8], [9], but due to high control currents, these sensors become bulky in order to prevent saturation of the transformer material. Ideally a current sensor with high current sensing capability, high resolution, high bandwidth and compact packaging is required for self-sensing. The high resolution and high bandwidth is required to be able to measure the high frequency amplitude modulated current.

1.4 Problem statement

The aim of this thesis is to evaluate existing self-sensing schemes, devise improvements and investigate possible new self-sensing schemes.
These self-sensing schemes must be modelled by using a simulation platform and must be implemented in hardware. A comparative performance study must be conducted to benchmark the self-sensing algorithms. The aim is to deliver a self-sensing scheme with high performance and reliability which is applicable to industrial applications which include cross-coupling effects.

1.5 Research aims and objectives

The following aims and objectives must be addressed:

- Obtain an accurate AMB simulation platform, which include nonlinearities.
- Identify different self-sensing schemes from literature.
- Investigate the effect of subcomponents of self-sensing schemes in simulation.
- Determine evaluation methods which can be used in simulation and practical setups.
- Develop new self-sensing schemes or new subcomponents of existing schemes in order to improve performance.
- Evaluate self-sensing schemes practically.
- Compare results and benchmark algorithms.

1.6 Research methodology

In the research methodology the methods to implement or satisfy the aims and objectives of the previous section are discussed.

Simulation platform: An accurate simulation platform must be identified to obtain an accurate simulation. The simulation platform will be implemented in MATLAB®. The simulation must include hysteresis, saturation, eddy currents and cross-coupling effects to obtain accurate simulation results. The simulation platform identified for this research is derived in [1].
Self-sensing schemes: Literature will be used as a basis for identifying the different self-sensing schemes. In this research the focus will be on amplitude modulation schemes using the self-sensing scheme proposed by Schammass [5] as a starting point. The self-sensing scheme will be simulated with a coupled reluctance network and the results will be compared.
Subcomponent effects: The self-sensing schemes will be simulated and where different subcomponents are used it will be compared to determine the influence of the different subcomponents. This will only be done in simulation due to ease of measurements. For this objective the focus will be on the demodulation methods.
Performance evaluation methods: The ISO 14839-3 standard will be used as a primary performance evaluation method [10]. Gain and phase relation will also be used as a performance measurement [5]. The advantage is that for these methods the estimated, real, error and reference position are digitally available in the hardware implementation.
Improvements and new self-sensing schemes: Most amplitude modulated self-sensing schemes make use of analog electronics for demodulation; by replacing the analog electronics with digital algorithms the performance may be increased. The digital algorithms will make use of finite impulse filters (FIRs), fast fourier transforms (FFTs) and sampling techniques to devise improvements.
New self-sensing schemes will be derived using theoretical knowledge gained from literature as well as practical experience. The new methods will first be mathematically derived to see if the self-sensing schemes are theoretically feasible. The new self-sensing schemes will then be evaluated in simulation to compare existing self-sensing schemes with the new self-sensing schemes. All of these schemes will focus on digital algorithm implementation.
Self-sensing evaluation: The self-sensing schemes will be practically evaluated on an in-house developed hardware. The in-house developed hardware platform consists of power amplifier, digital controller and self-sensing electronics. This hardware platform is capable of suspending one degree of freedom without any additional hardware.
Comparative study: By using the simulation and practical performance evaluation results of the different self-sensing schemes a comparative study can be compiled to benchmark the different self-sensing schemes and algorithms according to the performance measures.

1.7 Contribution of research

The contribution of this research lies in the evaluation and improvement of existing self-sensing schemes and the development of new self-sensing schemes.
The existing self-sensing scheme proposed by Schammass [5], [8] is used as basis and by applying different digital demodulation algorithms phase and noise effects are reduced. From a comparative study it was proved that phase effects can be directly linked to sensitivity performances.
Two new self-sensing algorithms, namely the direct current measurement (DCM) scheme and the gradient scheme, are introduced. Both methods are simulated and the theoretical concept is proved. From simulation it is determined that the gradient method is not practically feasible due to signal deformation. The effect of any low order filter deforms the signal such that the gradient is not a true representation of the rotor position. The DCM scheme outperformed all the other schemes in practice and simulation. The major advantage of the DCM scheme is that it performs well in a coupled AMB system.
The self-sensing schemes are simulated and practically evaluated on a 500 N AMB system which includes cross-coupling effects. The AMB system has a current range of 0 to 10 A. Such a high current self-sensing AMB system is a step closer to an industrial self-sensing application.

1.8 Overview of thesis

This thesis focuses on the improvement of existing and development of new self-sensing schemes to enhance performance for industrial application.
Chapter 2 presents a detailed literature study on self-sensing schemes and the basic operation of AMBs. The advantages, disadvantages and applications of AMBs are discussed. Self-sensing is divided into two groups, namely the state estimation and modulation self-sensing approach. The basic operation of each self-sensing approach is discussed in short. The focus of this thesis will be on the amplitude modulation approach. Nonlinear components which affect the operation of a self-sensing system are also introduced.
In **chapter 3** a basic AMB model is derived from which the current equation is obtained. This basic model is used as basis for the derivation of the different self-sensing schemes. A bi-state switch mode power amplifier current signal is analyzed using Fourier transform analysis and it is determined that the high frequency current component due to the switching frequency is nonlinearly dependent on the duty cycle. The self-sensing scheme proposed by Schammass [5] is discussed in detail. Different demodulation methods which can be used to evaluate Schammass's self-sensing scheme are discussed. Two new self-sensing schemes are derived and discussed. The effect of cross-coupling on a self-sensing AMB system is investigated.
In **chapter 4** the schemes derived in chapter 3 are simulated. The nonlinear transient simulation model (TSM) which is used to simulate the AMB is discussed in short. The nonlinear model identification method, which is dependent on the AMB system, is discussed for all the self-sensing schemes. Gain and phase relation and sensitivity are identified as performance measures and the evaluation of these measures are discussed in detail. Different controller implementation techniques to reduce noise effects are discussed. The nonlinear model identi-

fication method is applied to each self-sensing scheme and scaling is applied with the results shown graphically. The self-sensing schemes are statically and dynamically evaluated in terms of the performance measures. After all the self-sensing schemes are simulated the schemes are compared. The effect of cross-coupling on the FIR and DCM self-sensing techniques is simulated and compared.
In **chapter 5** the analog, FIR, band-pass sampling and band-pass filtered FFT demodulation techniques and the new DCM self-sensing technique are practically implemented. Alterations on the self-sensing techniques due to implementation feasibility are discussed in detail for the FIR and DCM self-sensing techniques. The performance of the practically implemented self-sensing techniques are obtained and discussed. The effect of cross-coupling is investigated on the practical AMB system.
In **chapter 6** the contributions and recommendations are discussed. From the results obtained it is determined that self-sensing remains a challenging subject. It was proved that self-sensing can be applied to a coupled AMB system and it still meets industrial standards under certain control parameters. There is, however, still plenty of room for improvement in the self-sensing research field.

Chapter 2

Background

In this chapter the basic operation of the active magnetic bearing (AMB) will be discussed as well as the advantages and disadvantages of AMBs. The focus will be on sensors and self-sensing methods implemented with AMB systems. The effect of magnetic material nonlinearities is discussed in terms of self-sensing position estimation.

2.1 Active magnetic bearings

Active magnetic bearings make use of the attracting forces of an electromagnet which are controlled in such a way that the ferromagnetic body is suspended at a specific position without any mechanical contact between the body and electromagnet. The ferromagnetic body and electromagnet are also known as a rotor and actuator respectively. Throughout the document the term rotor and actuator or stator will be used.

A stable one pole AMB system suspending the rotor at a specific position requires that the total force acting on the rotor must be zero. This is obtained when the force produced by the actuator (f_m) is equal to the gravity force (mg), where m is the mass of the rotor and g is gravitational acceleration. The magnetic force is dependent on the nominal air gap (g_0), the displacement (x) from the nominal air gap and the current (i) through the coil. The force is determined as follows

$$f_m = c\frac{i^2}{(g_0 + x)^2}, \tag{2.1}$$

where c is determined by the magnetic material, the number of turns and the geometry of the pole pair. In case one the current is kept constant at i_0 and the position is changed. The force-displacement plot is shown in figure 2.1 (a) [2]. An increase in air gap ($g_0 + x$) will result in a decrease in force. The force is inversely proportional to the square of the air gap. This inverse action results in instability when the system deviates from equilibrium. From this analysis it is determined that AMBs have negative stiffness (k_s) when current feedback is used. Due to this AMBs are naturally unstable and require a controller which provide positive stiffness. Figure 2.1 (b) shows the force-current relation where the air gap is kept constant at g_0. The force is a

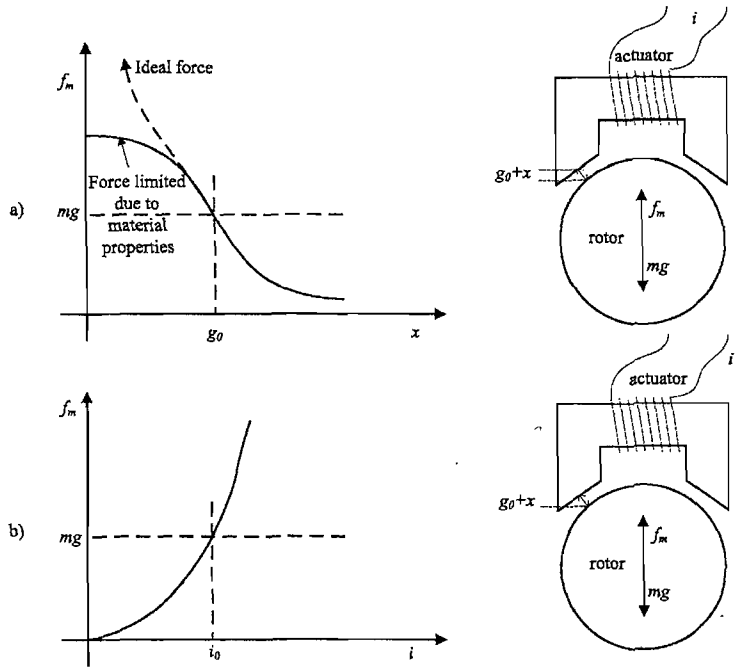

Figure 2.1: AMB current and position to force relation

quadratic function of the current. By regulating the current through the coil, the attracting force can be controlled which will regulate the force. With the use of a controller and the linearization of the AMB at a working point, the rotor can be suspended at a stable position [2].

Figure 2.2 shows the closed loop control of a one degree of freedom AMB system with only one actuator. The operation of an AMB system will be discussed by using this simplified AMB system. Negative feedback is required to obtain stability. A contactless position sensor is used

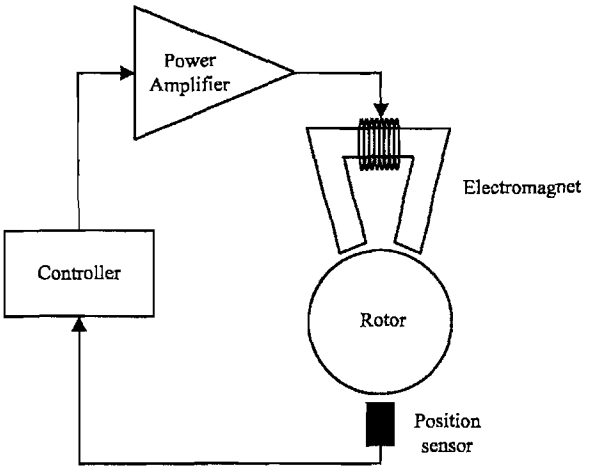

Figure 2.2: Basic AMB system

to sense the position of the rotor in the vertical direction. The position is fed to a PD controller where the output is a controlled current reference. The current reference is fed to a power amplifier, which converts the current reference signal to current which drives the actuator. The actuator exerts an upwards force on the rotor, which keeps the rotor at a specific position. If the position deviates from the desired position the controller will detect it and the force will be adjusted accordingly [2].

In the previous paragraph as shown in figure 2.2 the actuator exerts only an upwards force where the downward force is due to gravity. This downward force is not controllable. One way to overcome this problem is to implement a differential driving mode which enables the AMB system to control the upward and downward forces with equal stiffness and damping. A bias current is added to the control, which forces the system to a working point which improves the linearity of the AMB system. A differential driving mode AMB system is shown in figure 2.3 [2]. By adjusting the proportional and derivative gains of the controller the stiffness

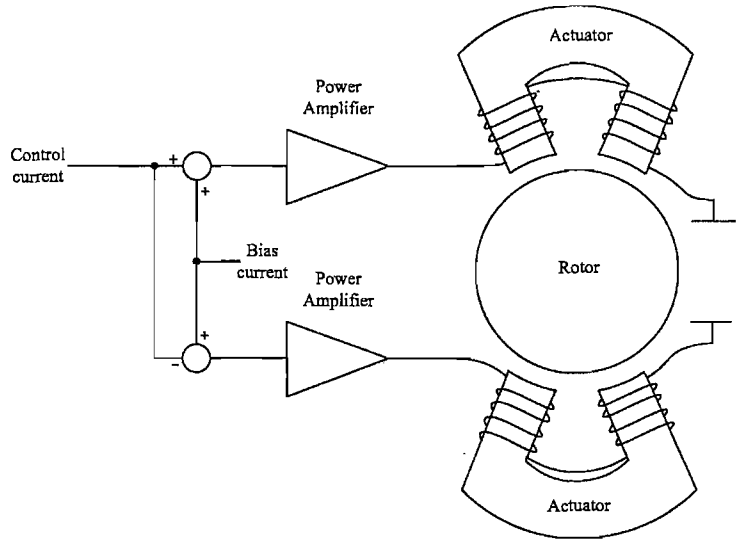

Figure 2.3: Differential driving mode

and damping can be adjusted. The stiffness is defined as the position deviation due to a certain force and damping minimizes the degree of oscillation. The stiffness as well as the damping upper limits are determined by the amount of noise present in the feedback loop of the AMB system which will lead to instability. The lower limit for the damping is due to nonlinearities. Ideally a system with zero damping will theoretically oscillate unattenuated, but due to nonlinearities the system will become instantly unstable. The lower limit of the stiffness constant (k) is determined by the magnitude of the AMB's negative stiffness k_s. The stiffness constant (k) and k_s must be in the same order of magnitude [2].

2.2 Magnetic bearing characteristics and applications

In this section the advantages and disadvantages of AMBs will be discussed. Typical applications of AMBs are also introduced.

2.2.1 Advantages

The rotor and actuator have no mechanical contact thus no lubrication is required. Due to no mechanical contact AMBs operate well at high speeds.
The bearing losses are much lower for AMBs than for conventional bearings, therefore reducing heat.
AMBs have lower maintenance due to low mechanical wear [2].
The stiffness and damping of the AMB can be adjusted using different control constants.
The position sensors and current signals can be used for system monitoring.

2.2.2 Disadvantages

AMBs are more expensive than conventional bearings due to their complexity [2], [9].
The design knowledge of AMBs is not available to the user, thus it is difficult to integrate knowledge about conventional bearings with AMBs [2]. The role of an industrial standard for AMBs will eliminate this pitfall [11].
The physical size of AMBs are much larger than conventional bearings for the same application, thus AMBs are more space consuming.

2.2.3 Applications

AMBs have become a key technology in high speed industrial applications and the elimination of lubricants make AMBs suitable for various contamination free applications such as vacuum applications and the transport of pure or aggressive materials [2].
AMBs are used as positioning systems in silicon manufacturing due to nm accuracy. Contamination is minimized since no lubrication is present [12].
AMBs are used with high speed applications such as flywheel storage systems, vacuum pumps and turbomolecular pumps [11]. Flywheel systems require high speed operation and low bearing losses, which both are advantages of AMBs [2], [11].
AMB applications in machine tools are also on the increase due to high-speed machining and due to the increase of metal cutting productivity. The stiffness of AMBs is higher than conventional bearings at higher rotating speed. AMBs also have the capability of enhancing cutting process stability by counteracting harmonic forces through advanced control methods [2], [13].
AMBs are used to form hybrid magnetic bearings which combines passive and active magnetic bearings [14].

2.3 Position sensing

Position sensors form an important part of the integration of AMB systems. The efficiency of an AMB is dependent on the efficiency of the position sensor used to measure the rotor position [2]. Eddy current sensors are commonly used with AMB systems due to their high resolution, fast response time, high stability and compactness [3]. The major disadvantage of conventional position sensors is the cost and the sensor is viewed as the weakest point in an AMB system with respect to reliability [15]. Due to sensor cost there is a continued drive for new and cheaper position sensing methods.

One such type of sensor which is intriguing to AMB systems, is sensorless sensors, also known as self-sensing. Self-sensing relies on the AMB's actuator to sense the position and to convert electrical energy to mechanical energy. This combination of position extraction and position control is cumbersome since the control signal is much larger than the position sensing signal and nonlinearities have a large effect on the self-sensing accuracy. Modern methods of measuring and control enable compensation for nonlinearities. To make optimal use of advanced control methods DSPs and FPGAs are used to implement the high processing demand. The use of digital controllers is another step closer to an integrated AMB system [16].

The first industrial application of a self-sensing turbomolecular pump system was implemented in 2005 by S2M [4] and the second industrial application is in elevator guideways [17].

Self-sensing increases reliability due to the reduction in component count. Self-sensing can also be used for redundancy, where the conventional sensors are used as main feedback and self-sensing is used as backup sensors.
Self-sensing eliminates collocation problems and reduces rotor length when conventional sensors are not used. Collocation is the effect due to sensor and actuator misalignment. By eliminating conventional sensors the rotor length can be reduced since the sensing area is not required anymore. The reduction in rotor length results in a first bending mode at a higher rotation speed [9].
Self-sensing enables AMBs to operate in hostile conditions without additional modifications to the self-sensing sensor, where expensive conventional position sensors must be used to withstand the hostile conditions.

2.4 Self-sensing methods

Different types of AMB self-sensing methods were developed in the past which can be divided into three main categories; 1) State estimation , 2) Frequency modulation and 3) Amplitude modulation.

2.4.1 State estimation

State estimation makes use of the current and voltage signals of the power amplifier as inputs to a state model or observer. The output of the observer is an estimated position. Figure 2.4 is an illustration of a state estimation AMB system. The construction of an observer is based on

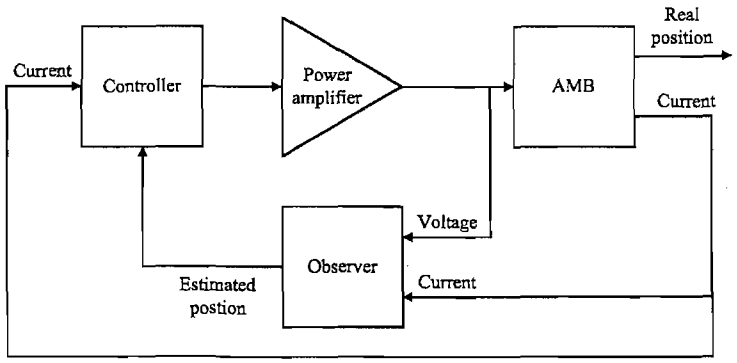

Figure 2.4: State estimation scheme

a system model. In a high order system the observer has a complicated structure and due to practical model uncertainties it is rather difficult to match the model with the physical system and thus the observer accuracy is affected [18]. The state model must be observable and robust. Research on state feedback was done by Vischer [19], Mizuno [20], Sasaki [21] and Li *et al* [9]. Stable suspension was obtained with a full observer. From literature it was found that the state estimation is sensitive to parameter variations [22], [23], thus state estimation is not robust.

2.4.2 Frequency modulation

The frequency modulation scheme relies on an oscillation component, of which the frequency is dependent on the inductance of the AMB actuator. Hysteresis amplifiers were used due to their frequency dependance on the load. When two hysteresis power amplifiers are applied to a differential driving mode AMB system, the switching frequency of the power amplifiers will change according to the actuator inductances.
If one of the coil's switching frequency increases, the opposing coil's switching frequency will decrease. By converting the two switching frequencies of the power amplifiers to a voltage signal and feeding it to a controller, the rotor position can be estimated. Figure 2.5 shows the implementation of a differential mode AMB system driven by two hysteresis amplifiers. Frequency modulation research was done by Mizuno *et al* [24]. From practical results it was determined that the self-sensing scheme has low bandwidth due to the phase lag on the feedback signal. Another disadvantage is that hysteresis amplifiers are not commonly used in AMB applications.

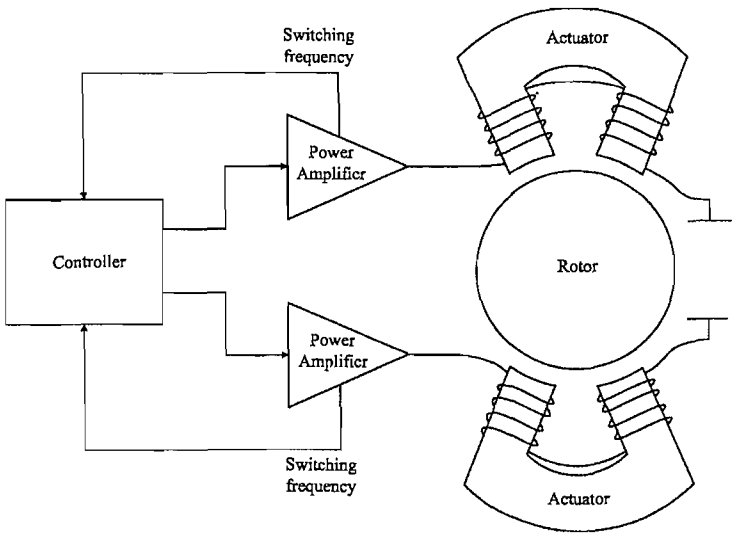

Figure 2.5: Frequency modulation scheme

2.4.3 Amplitude modulation

Amplitude modulation makes use of two signals namely the modulation signal and the carrier signal [25]. The carrier frequency is at a much higher frequency than the modulation signal. In a self-sensing AMB system, the carrier can be a high frequency current component superimposed on the control current. The switching ripple of the switch mode power amplifier can also be used. The modulation signal is the change in position which is at low frequencies due to the mechanical bandwidth. The result of the amplitude modulation is a high frequency component of which the envelope is modulated by the position. The amplitude modulation of the current is incorporated in the change in the inductance when the rotor position deviates.

The envelope amplitude variation of the high frequency current component can be demodulated to estimate the rotor position. This method is investigated by a large group of researchers, such as Maslen, Noh, Montie, Schammass, Sivadasan and Yim *et al* to name a few. Literature shows amplitude modulation has the most promising results and the robustness is higher than previous self-sensing approaches.

Amplitude modulation can be divided into two research groups: 1) The high frequency signal injection method where a high frequency component is superimposed on the control current [26], [27] and 2) where the switching ripple of switch mode power amplifiers is used as the high frequency component [5], [8], [28], [29], [30], [31], [32].

The high frequency signal injection method uses a superimposed signal with a higher frequency than the AMB bandwidth and a lower frequency than the power amplifier bandwidth. Linear power amplifiers are commonly used with this approach. The envelope amplitude of the superimposed current varies according to the changing inductance due to position variations.
Due to the frequency bounds the injection component frequency is relatively low. The maxi-

mum bandwidth of this self-sensing method may be affected due to the frequency closeness of the control and sensing component, thus this method will not be investigated further.

In most cases switch mode power amplifiers are standard components in an AMB system due to their high efficiency. An amplitude modulated self-sensing technique which makes use of the power amplifier switching ripple is ideal for an industrialized self-sensing AMB system, since no additional hardware are required and no additional current components are added to the control current.
Figure 2.6 illustates the basic operation of an amplitude modulation method. The control current consists of two frequency components, 1) the low frequency control current and 2) the high frequency switching ripple due to the power amplifier. The high frequency component is position modulated. By performing amplitude demodulation on the high frequency current the position can be estimated. The duty cycle of a switch mode power amplifier changes constantly

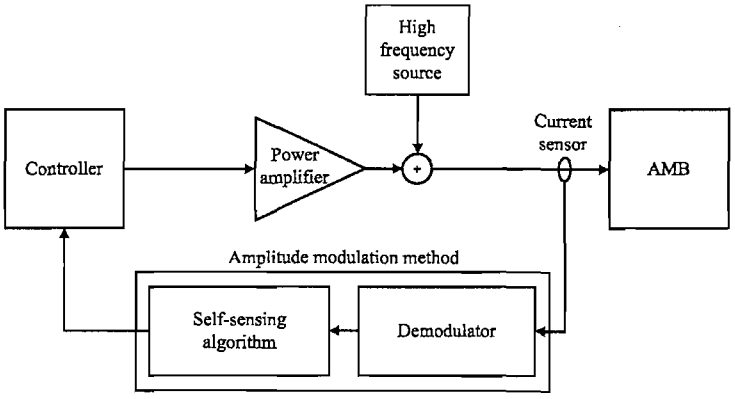

Figure 2.6: Basic amplitude modulation self-sensing scheme

to maintain the current reference. The change in duty cycle has a large effect on the demodulated position estimation. Duty cycle compensation can be done using a nonlinear controller as implemented by [28], [29], [30], [31], [33], [34] or by demodulating the voltage signal and dividing the demodulated current with the demodulated voltage [8], [35].

From the literature it was decided to investigate the amplitude modulation method which makes use of the power amplifier switching ripple, since switch mode power amplifiers are commonly used with AMB systems and also due to the higher robustness of these self-sensing schemes.

2.5 Self-sensing robustness

Robustness is one of the most challenging components in self-sensing research. Literature has shown that self-sensing research is divided into two paths. The first group makes use of Linear Time Invariant (LTI) models where the second group makes use of nonlinear models. A point of consensus between the two groups is to measure the sensitivity of an AMB system to determine

the robustness of the system. The reason for sensitivity as measure of robustness is due to ease of measurement and the connection to the Nyquist criterium [31]. The sensitivity of an AMB system must be below 2.5, or converted to dB scale it must be below 8 dB for a new commissioned industrial system according to the ISO 14839-3 AMB standard [10].

According to the results of Morse *et al* [6], which uses LTI models, it was proved that self-sensing sensitivity has a minimum of 5 or 14 dB. According to these results self-sensing is not feasible for industrial applications. In the case where a more practical approach is followed, which includes nonlinear effects, the minimum sensitivity of 3.5 or 10.8 dB was determined from practical results . From these results self-sensing can be used for industrial applications. The lower sensitivity was obtained by using the amplitude modulation approach. This increase in robustness may be due to the high frequency current which can be modelled as a Linear Periodic (LP) system [7]. From these results it is encouraging that self-sensing can be optimized for industrial applications.

2.6 Nonlinearities

In most cases the models used for AMB modelling are based on a linearized model. From literature it is found that nonlinearities have large effects on modelling iron cores [36]. In this research the effects of saturation, eddy currents and cross-coupling are investigated.

2.6.1 Saturation

Saturation is one of the most prominent nonlinear effects in a self-sensing system. Since self-sensing relies on the change in air gap reluctance, saturation will result in the decrease of the permeability. When the material permeability decreases, the reluctance of the material becomes large enough to affect the air gap reluctance. In extreme cases of saturation the estimated position shows position reversal. In less severe saturation a position error is made. Research was done on saturation in self-sensing techniques by researchers such as Noh, Skricka and Schammass [5], [28], [37].

2.6.2 Cross-coupling

The poles of an AMB's actuator are coupled to each other with the back iron. Due to this back iron the poles are magnetically coupled and cross-coupling occurs. Cross-coupling is the effect that each individual pole has on another. The effect can easily be eliminated by cutting the stator to have independent poles, thus forming an uncoupled AMB system. This technique is applied by numerous researchers such as Schammass [5]. By cutting the stator the mechanical manufacturing costs increase drastically.

In the case of a coupled AMB system cross-coupling is dependent on geometric changes, thus

geometric cross-coupling and flux distribution due to back iron.

Geometric cross-coupling

Geometric cross-coupling is the effect that a change in rotor position has on a specific self-sensing pole due to the position change in the remaining poles. This can be explained in terms of the change in the mutual inductance components when the rotor position changes. It is also important to note that the movement in any direction will effect all poles due to the circular stator configuration. The effect of cross-coupling due to the curved poles is investigated by Skricka [37].

Cross-coupling due to flux distribution

Due to the back iron all poles are interconnected with each other and thus a change in one coil's electromotive force mmf will have an overall effect on all the coils. In this case even when the rotor is forced to a specific position a change in the current through a coil will affect all the others. This is due to the interconnected reluctance network of a coupled AMB system. This effect is researched by many researches due to the force errors which are made when normal controllers are used in high speed applications [38], [39], [40].

2.6.3 Eddy currents

Eddy currents are frequency dependent, which affects the current ripple of a switch mode power amplifier. Eddy currents persist when currents are flowing through the stator material due to the changing magnetic fields produced by the AMB system. The simplest form of explanation is that a second single turn short circuited coil exist within each AMB coil . This results in an instantaneous current change when the power amplifier switches. The effect of eddy currents are investigated with the single turn coil and a more realistic continuous model [41]. Eddy currents have a lowering effect on the permeability of the material [42]. When the permeability decreases the reluctance of the material increases and thus it will effect the current ripple. When a ripple with a large amount of eddy current is used for self-sensing, the air gap reluctance is not dominant and thus the self-sensing resolution is affected. The eddy current effects can be reduced by using a thin laminated material for the actuator and by reducing the switching frequency.

In this chapter the basic operation of the active magnetic bearing was discussed. It was found that AMBs are inherently unstable due to the negative stiffness. Stability can be obtained by using a controller and the rotor position as negative feedback. The advantages and disadvantages of AMBs were highlighted. From the disadvantages cost was identified as a major drawback of AMBs. Since conventional sensors

form a major part of the costs in small AMB systems, self-sensing was identified as a possible method to reduce rotor position sensor costs. Self-sensing also has the capability of increasing reliability due to the reduced sensor wire length and the fact that the sensors are not located at the mechanical system. Three different self-sensing schemes were identified from literature namely 1) the state estimation scheme, 2) the frequency modulation scheme and 3) the amplitude modulation scheme. The amplitude demodulation scheme, which makes use of the power amplifier ripple, was identified for this research due to the higher performance obtained from literature and since switch mode power amplifiers are commonly used with AMB systems. The focus of this research will be on digital implementation methods. The basic operation of the amplitude demodulation method was discussed and from literature it was found that in most cases analog methods are used to estimate the rotor position. The effect of nonlinearities on self-sensing schemes was also introduced.

Chapter 3

Self-sensing schemes

In this chapter a basic AMB system will be discussed together with all its subcomponents. The focus will be on the actuator and the switch mode power amplifier which drives the actuator. A basic actuator model will be derived, which will be used as basis for the different self-sensing schemes. Each of the self-sensing schemes and models will be discussed in detail.

3.1 Basic actuator model

In a self-sensing AMB system the actuator not only determines the performance of the mechanical forces, but also the performance of the estimated position. The actuator of an AMB is highly nonlinear due to the material properties as stated in section 2.6. Figure 3.1 shows an eight-pole actuator which is configured in four pole pairs with NSSNNSSN convention. This actuator configuration will be used to evaluate the self-sensing schemes. For simplicity, a basic horseshoe model will be derived and nonlinearities will be introduced at a later stage. Figure 3.2 shows the mechanical and magnetic configuration of the simplified actuator. The material of the actuator is assumed to be linear, thus the material permeability is assumed to be constant and thus saturation and hysteresis are neglected. Flux leakage and eddy current effects are also neglected. By applying Faraday's law on the coil, (3.1) is obtained,

$$u = N\frac{d\phi}{dt} + Ri \tag{3.1}$$

where u is the voltage across the coil, N is the number of turns, ϕ is the flux, R is the resistance of the copper wire and i is the current through the coil.
By considering the magnetic circuit in figure 3.2 the reluctance of the air gap is obtained by (3.2),

$$\Re_g = \frac{2(g_0 + x)}{\mu_0 A} \tag{3.2}$$

where g_0 is the nominal air gap length, x is the rotor position deviation from the nominal air gap, μ_0 is the permeability of free space and A is the cross-sectional area of the material.

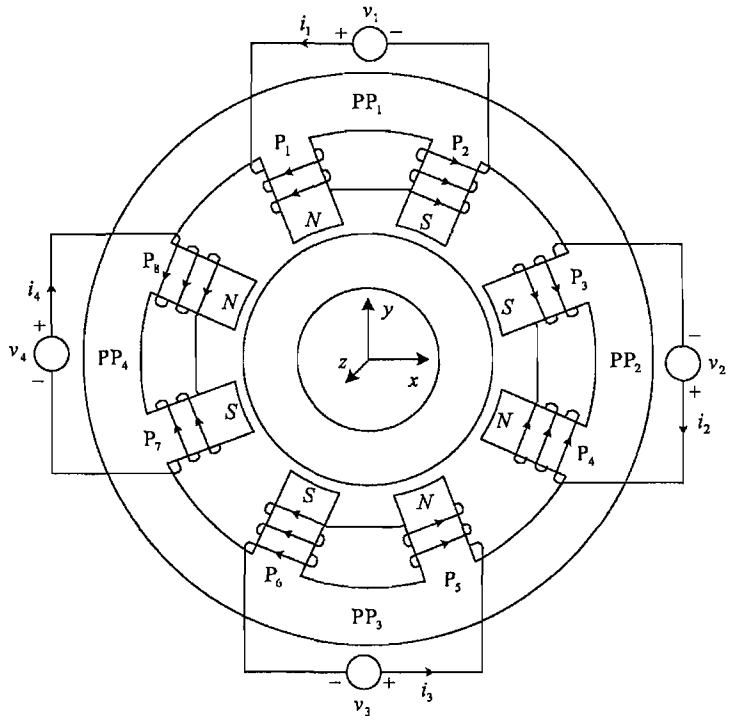

Figure 3.1: Eight pole AMB system [1]

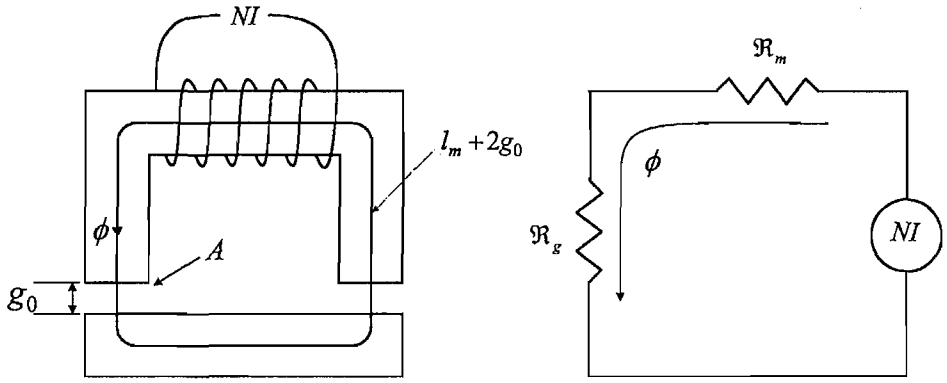

Figure 3.2: Basic actuator model

Fringing effects are neglected in this case. The reluctance of the material flux path is calculated as follows,

$$\Re_m = \frac{l_m}{\mu_0 \mu_r A} \tag{3.3}$$

where l_m is the path length through the material and μ_r is the relative permeability of the material. The total reluctance is obtained by adding (3.2) and (3.3).

$$\Re = \frac{2(g_0 + x) + l_m/\mu_r}{\mu_0 A} \tag{3.4}$$

If it is assumed that the flux through the material and the air gap is the same then the flux can be obtained by (3.5).

$$\phi = \frac{Ni}{\Re} \tag{3.5}$$

By substituting (3.4) into (3.5) the flux flow governed by the reluctance can be determined as follows:

$$\phi = \frac{\mu_0 NA}{2(g_0 + x) + l_m/\mu_r} i. \tag{3.6}$$

By substituting (3.6) into (3.1) the voltage across the coil is given by:

$$u = \frac{\mu_0 N^2 A}{2(g_0 + x) + l_m/\mu_r} \cdot \frac{di}{dt} + Ri. \tag{3.7}$$

By rewriting (3.7) the derivative of the current through the coil is given by (3.8).

$$\frac{di}{dt} = \frac{2(g_0 + x) + l_m/\mu_r}{\mu_0 N^2 A}(u - Ri) \tag{3.8}$$

Equation (3.7) and (3.8) will be used as basis for the self-sensing schemes in the following sections.

3.2 Drive and switching waveform

Before any self-sensing scheme can be introduced, the drive used to convert the control signals to current must be discussed. From literature it was decided to make use of the amplitude modulation self-sensing scheme which relies on the switch mode power amplifier's current ripple component. Bi-state pulse width modulated (PWM) signals are used in this research. As the name states, the bi-state power amplifier has two states, namely the positive-polarity state and negative-polarity state and due to this switching convention, the ripple is maximum which increases self-sensing robustness. The PWM switching frequency is set at 20 kHz, since the current ripple sensitivity increases as the switching frequency decreases [5].
When a switching voltage with a changing duty cycle is applied to the coil model (3.8), the current through the coil contains a low frequency control component and a high frequency ripple component. The high frequency ripple component is a sawtooth waveform as shown in figure 3.3. When a force is applied on the rotor of a closed loop AMB system, the current through the coil continuously changes according to the force. The controller then adjusts the duty cycle in order to stabilize the rotor. The bandwidth of the AMB system is much lower than the switching frequency, thus the control signal is analyzed as a low frequency component. By using Fourier series analysis the dc voltage component is determined by (3.9),

$$u_0 = u_z(2\alpha - 1) \tag{3.9}$$

where u_z is the supply voltage of the power amplifier and α is the duty cycle which can change from 0 to 1.
Since the current signal is used to estimate position, the effect of duty cycle variation must be investigated for bi-state power amplifiers. When the position is kept constant and the duty

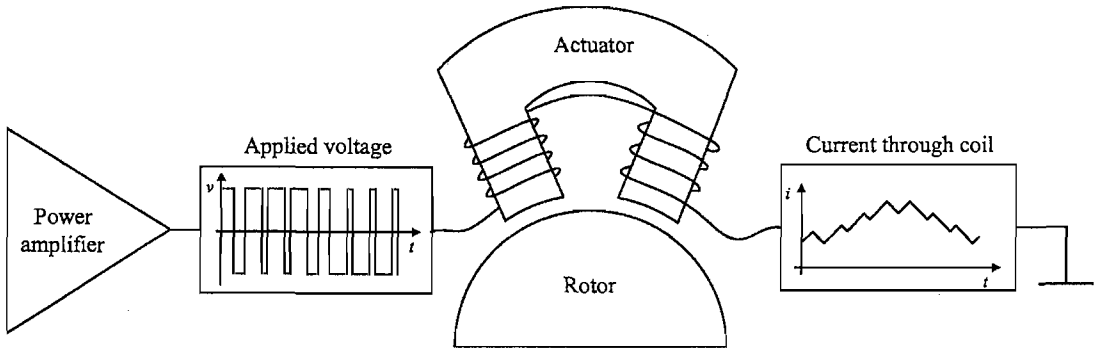

Figure 3.3: Current waveform due to switch mode power amplifier

cycle is varied over the full range, it was determined that duty cycle variation has a large effect on the modulated current ripple amplitude. The modulated amplitude is therefore position and duty cycle dependent [5], [28]. From Fourier series analysis the amplitude of the high frequency switching voltage amplitude is described by (3.10).

$$u_s = \frac{4u_z}{\pi}\sin(\pi\alpha) \tag{3.10}$$

at the fundamental frequency.
It is assumed that the switching frequency is much higher than the change rate of the duty cycle. Figure 3.4 shows the influence of duty cycle variation on the low frequency and high frequency switching voltage. From figure 3.4 it is clear that the high frequency amplitude envelope of the

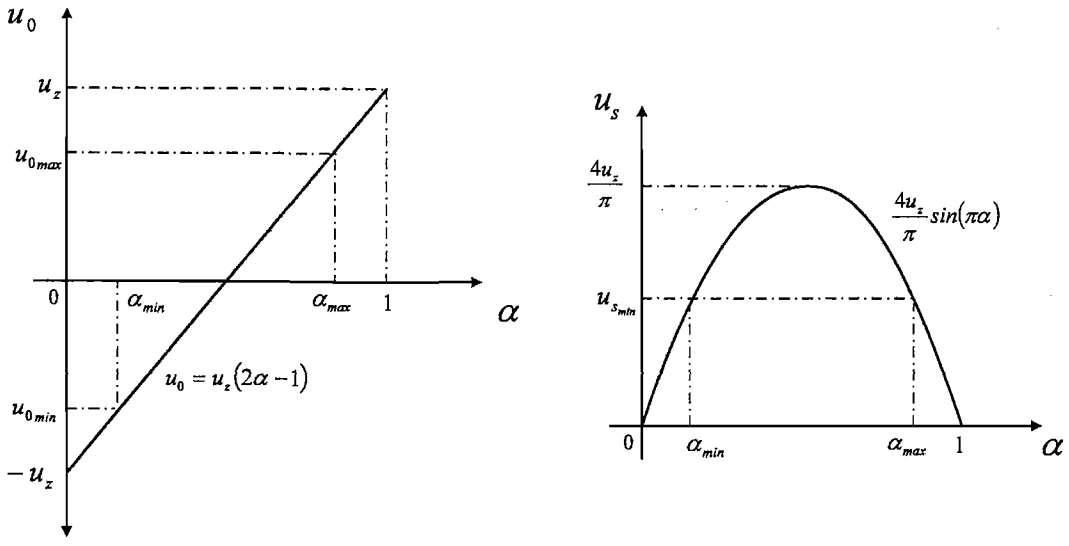

Figure 3.4: Amplitude variation due to changing duty cycle

fundamental component is 0 when the duty cycle is 0 or 1. To ensure that demodulation is

always possible the duty cycle must be limited. In this research the duty cycle α_{min} and α_{max} is limited between 0.25 and 0.75 which results in a 0.5 operating range. Due to the 0.5 duty cycle range the slew rate of the power amplifier is decreased. The supply voltage u_z may, however, be increased to compensate for the reduced slew rate.

3.3 Self-sensing based on Schammass's work

This section will focuss on the method proposed by Schammass, which makes use of an inverse frequency shifted model [5], [8]. An overview of the frequency shifted model will be given. The focus of this research will be on the demodulation methods used to determine the inputs of the frequency shifted model.

3.3.1 Modelling

Figure 3.5 shows a basic block diagram of the amplitude modulation method. The current through the coil is sensed and passed through a band-pass filter (BPF) to extract the fundamental component of the switching ripple. The fundamental component is shifted to low frequencies by the demodulation method. The demodulated component is used as an estimated rotor position if all demodulation and AMB components are assumed to be linear. Since the AMB

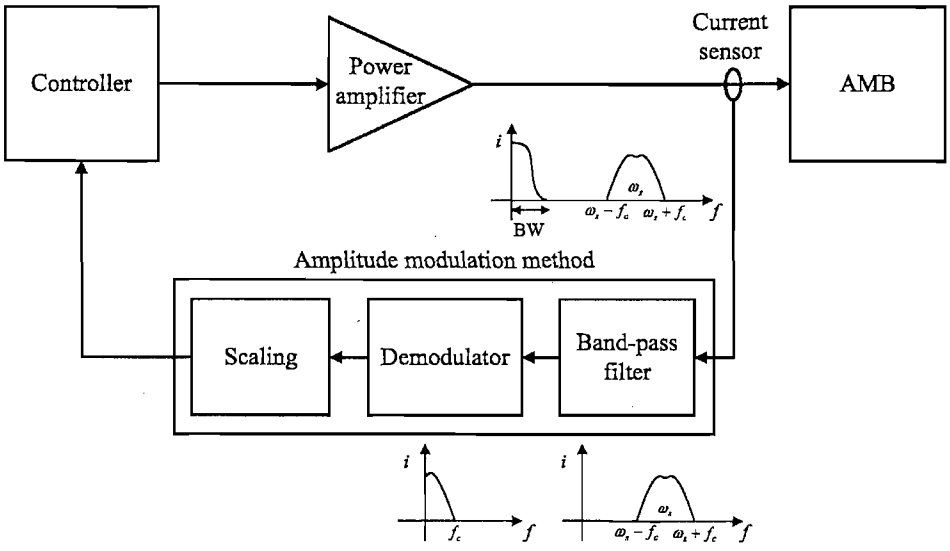

Figure 3.5: Amplitude modulation method

is a highly nonlinear system, the AMB nonlinearities must be investigated. In the next section the linear frequency shifted model will be introduced along with some nonlinearities.

Frequency shifted linear model

As stated in the previous section, the rotor position is estimated by demodulating the current signal. The high frequency current is shifted to low frequencies using the demodulator. The idea is to shift the AMB model to low frequencies, since this will reduce the processing intensity of the AMB model. The advantage of the shifted model is that nonlinearities which are modelled at low frequencies, can be included.
Figure 3.6 shows the difference between the high and low bandwidth AMB models. In the high

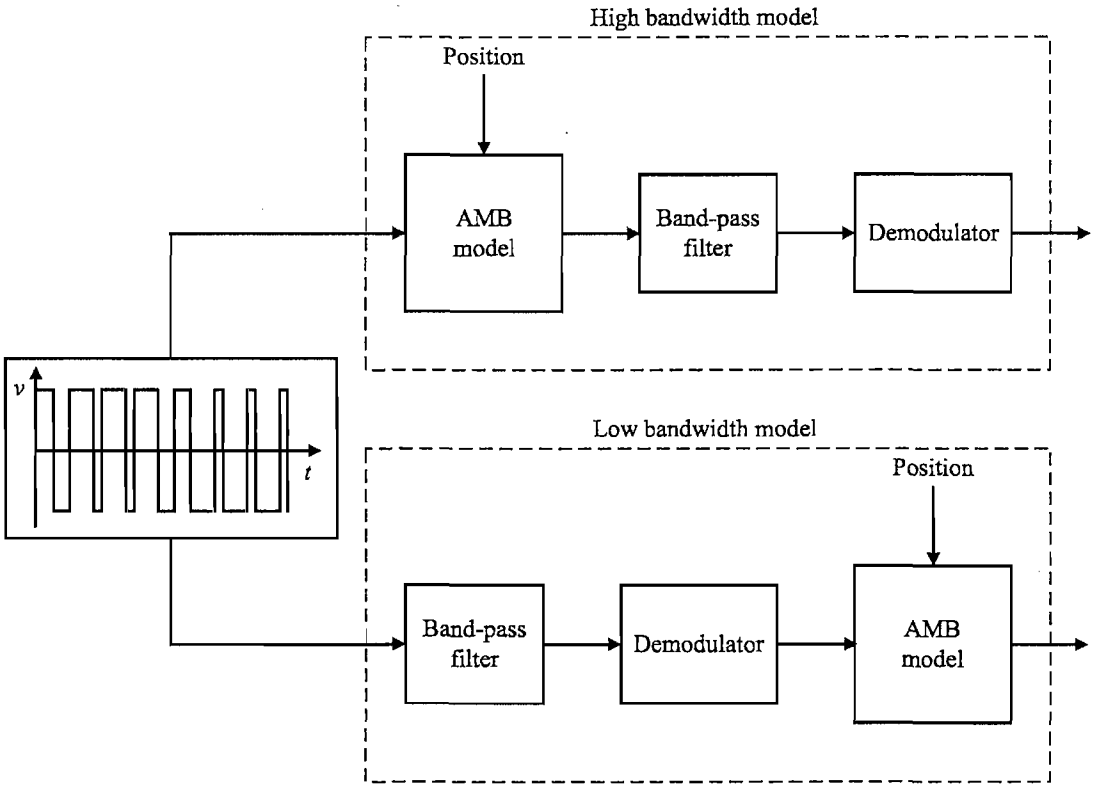

Figure 3.6: Frequency shifted model

bandwidth model the inputs are the high frequency PWM switching voltage and the position of the rotor. The model for such a setup requires a high bandwidth, since the switching voltage consists of an infinite bandwidth. The low bandwidth model's inputs are the demodulated voltage signals and the rotor position. These signals have maximum bandwidth of approximately 1000 Hz, which is the mechanical bandwidth of the AMB system.
The coil model (3.8) derived in section 3.1 is used as the basis for the derivation of the frequency shifted model. In a typical AMB system the coil resistance (R) is much lower than the inductive reactance ($\omega_s L_0$), where ω_s is the switching frequency and L_0 is the nominal inductance. If $R \ll \omega_s L_0$, the influence of R can be neglected and the current through the coil can be estimated by (3.11),

$$i = \frac{1}{K}(2(g_0 + x) + l_m/\mu_r) \int u \, dt \tag{3.11}$$

where $K = \mu_0 N^2 A$ and μ_r is assumed to be constant.
If the switching voltage u is replaced with the fundamental component of the voltage $u_d \sin(\omega_s t)$, where the term u_d is the high frequency duty cycle modulated signal, as discussed in section 3.2, (3.11) can be written as:

$$i = -\frac{1}{K\omega_s}(2(g_0 + x) + l_m/\mu_r)\, u_d \cos(\omega_s t). \tag{3.12}$$

The high frequency component is shifted to a low frequency when it is passed through the demodulator which includes a low-pass filter (LPF). By passing (3.12) through the demodulator the low frequency AMB model is obtained, as given by (3.13).

$$\underline{I_d} = -\frac{1}{K\omega_s}(2(g_0 + x) + l_m/\mu_r)\, \underline{U_d} \tag{3.13}$$

This frequency shifted AMB model will be used as basis for this research. In the next section the low frequency modelled nonlinearities will be investigated .

Modelling of nonlinear material permeability

In the previous section the relative permeability of the material μ_r was assumed to be a constant, but this is not true in practice. The relative permeability of the material is dependent on the flux density B, which results in material saturation. Different hysteresis models are available like the Preisach and the Jiles-Attherton models [43], [44], [45]. For the purposes of this research, however, the same simplified magnetic material model as derived by Schammass [5] is used. This magnetic material model includes saturation and eddy current effects, but not hysteresis. Eddy currents are compensated for since it is a dc error in the demodulated signal [5]. From (3.13) it is clear that the the inverse of μ_r is required for the saturation model. A quadratic function is used to model the inverse material permeability. The order of the nonlinear function can be increased to model the nonlinearities more accurately. Equation (3.14) shows the inverse quadratic permeability function.

$$1/\mu_r \approx f(B) = a_{m2}B^2 + a_{m1}B + a_{m0} \tag{3.14}$$

where a_{m2}, a_{m1} and a_{m0} are coefficients of the polynomial. By substituting (3.14) into (3.13) the nonlinear frequency shifted current model is obtained as follows,

$$\underline{I_d} = (k_x x + k_{b2}B^2 + k_{b1}B^2 + k_{b0})\underline{U_d} \tag{3.15}$$

where $k_x = -2/(K\omega_s)$, $k_{b2} = l_m a_{m2}/(K\omega_s)$, $k_{b1} = l_m a_{m1}/(K\omega_s)$ and $k_{b0} = l_m a_{m0}/(K\omega_s)$. Since it is difficult to measure the flux density B it is therefore estimated. The estimation includes only the change in the low frequency flux density which is dependent on the current and the air gap. This estimation is given by (3.16),

$$B \approx (\frac{\mu_0 N}{g_0 + x} + \frac{L_s}{NA})i_L \tag{3.16}$$

where L_s is the leakage flux and i_L is the low frequency current component.

Static model identification

From the previous section the nonlinear frequency shifted model was derived with $k_x, k_{b2}, k_{b1}, k_{b0}$ as inductor model coefficients. In this section the calculation of these coefficients is illustrated by using simulation and practical measurements to identify the nonlinear characteristics of the simulated and practical inductor model.
The coefficients k_{b2}, k_{b1}, k_{b0} are derived by changing the flux density through the coil and keeping the position at the center position ($x = 0$). The current through the coil is changed from the minimum to the maximum value in order to change the flux density over the full operating range. By using (3.16) the flux density through the material can be estimated and the demodulated current $\underline{I}_{dk}$ and voltage signals $\underline{U}_{dk}$ measured. Equation (3.17) is used to evaluate these measurements,

$$\begin{aligned} B_k &= (\tfrac{\mu_0 N}{g_0} + \tfrac{L_s}{NA}) i_{Lk} \\ B_k^2 k_{b2} + B_k k_{b1} + k_{b0} &= \tfrac{\underline{I}_{dk}}{\underline{U}_{dk}} = \underline{I}_{uk} \end{aligned} \tag{3.17}$$

where $k = 1, 2, 3...n$, represents the number of measurements. By using least squares these coefficient constants can be determined as described in (3.18).

$$\begin{bmatrix} B_1^2 & B_1 & 1 \\ B_2^2 & B_2 & 1 \\ \vdots & \vdots & \vdots \\ B_n^2 & B_n & 1 \end{bmatrix} \begin{bmatrix} k_{b2} & k_{b1} & k_{b0} \end{bmatrix} = \begin{bmatrix} \underline{I}_{u1} \\ \underline{I}_{u2} \\ \vdots \\ \underline{I}_{un} \end{bmatrix} \tag{3.18}$$

The constant k_x is determined using the constants obtained in (3.18) and by keeping the current of the AMB constant at the bias level and changing the position x from the minimum to the maximum position, again taking n measurements. Equation (3.19) is used to obtain the data as required by (3.18).

$$\begin{aligned} B_k &= (\tfrac{\mu_0 N}{g_0 + x} + \tfrac{L_s}{NA}) i_{Lk} \\ x_k k_x &= \tfrac{\underline{I}_{dk}}{\underline{U}_{dk}} - B_k^2 k_{b2} - B_k k_{b1} - k_{b0} \end{aligned} \tag{3.19}$$

By using least squares as shown in (3.20) k_x can be calculated.

$$\begin{bmatrix} x_1 \\ x_2 \\ \vdots \\ x_n \end{bmatrix} \begin{bmatrix} k_x \end{bmatrix} = \begin{bmatrix} \underline{I}_{u1} - k_{b2} B_1^2 - k_{b1} B_1 - k_{b0} \\ \underline{I}_{u2} - k_{b2} B_2^2 - k_{b1} B_2 - k_{b0} \\ \vdots \\ \underline{I}_{un} - k_{b2} B_n^2 - k_{b1} B_n - k_{b0} \end{bmatrix} \tag{3.20}$$

Position estimation

The self-sensing algorithm is derived from the frequency shifted AMB model as described in (3.13), which is nonlinearly dependent on the PWM duty cycle and the nonlinear magnetic material. The self-sensing algorithm proposed by Schammass [5] compensates digitally for both nonlinearities. A block diagram of the self-sensing algorithm is shown in figure 3.7. The

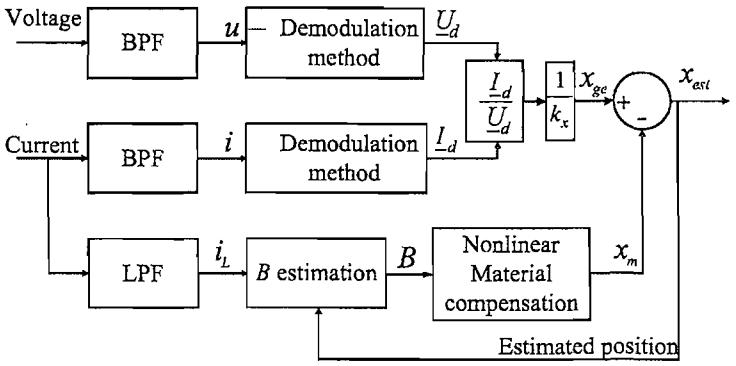

Figure 3.7: Inverse frequency shifted model block diagram

current and voltage signals are band-pass filtered to obtain the fundamental component. The fundamental components are demodulated and shifted to low frequencies by the demodulation process, thus (3.13) can be directly applied. The demodulated current and voltage signals are digitized and the self-sensing algorithm is digitally implemented. If the nonlinear material is neglected at first, then (3.21) is obtained.

$$x_{ge} = \frac{1}{k_x}\frac{\underline{I}_d}{\underline{U}_d} \tag{3.21}$$

Since both the current and voltage signals are affected by the same nonlinear duty cycle component, the division of the two components eliminates the effect of the duty cycle modulation. It is assumed that the demodulated voltage can never be zero.
If the effect due to the nonlinear material on the estimated position is investigated separately, (3.22) is obtained.

$$x_m = \frac{1}{k_x}(k_{b2}B_e^2 + k_{b1}B_e + k_{b0}) \tag{3.22}$$

The magnetic flux B_e is required to evaluate (3.22). By passing the current through a LPF the current i_L is obtained. This LPF consists of the combination of two LPFs of which one has the same response as the power amplifier and the second filter has approximately the same gain and phase effects as the demodulation process. The filter is required so that x_m has the same phase shift as x_{ge}. This LPF effect due to the demodulation process is discussed in the subsequent section.
The magnetic flux can be estimated using (3.16) where x is replaced by one delayed sample of the estimated position x_{est}. Thus the magnetic flux is determined by (3.23).

$$B_e = (\frac{\mu_0 N}{g_0 + x_{est}} + \frac{L_s}{NA})i_L \tag{3.23}$$

The estimated position of the total self-sensing algorithm is the combination of (3.21) and (3.22).

$$x_{est} = x_{ge} - x_m = \frac{1}{k_x}(\frac{\underline{I}_d}{\underline{U}_d} - k_{b2}B_e^2 - k_{b1}B_e - k_{b0}) \tag{3.24}$$

3.4 Demodulation methods

In section 3.3.1 the inverse frequency shifted model proposed by Schammass was discussed in detail. The self-sensing algorithm performance is strongly dependent on the demodulation method.
The rest of this section will focus on four different demodulation techniques, with the aim to increase the performance of the inverse self-sensing algorithm. The four demodulation methods which will be investigated are the analog, digital sampling, band-pass sampling and FFT methods.

3.4.1 Analog demodulation method

The current and voltage signals are sensed using an LAH25-NP LEM current sensor and a basic voltage divider respectively. The sensed signals are then passed through the demodulator. The analog demodulation method is the same as the proposed method of Schammass as shown in figure 3.7 [5]. The dc components of the sensed signals are removed by passing the signals through a BPF. The analog demodulation process consists of a synchronous demodulator and a LPF as shown in figure 3.8. Each of the subcomponents are discussed in detail. The BPF iso-

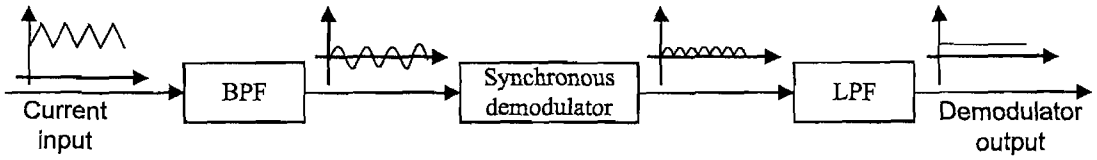

Figure 3.8: Demodulation process

lates the fundamental component of the modulated high frequency component and removes all other frequencies. The synchronous demodulator consists of an absolute value and a LPF. The high frequency component is passed through the demodulator which shifts the high frequency fundamental component to low frequencies. The analog demodulation is most commonly used since it simplifies the programming of the self-sensing algorithm implementation on the controller and also due to digital sampling limitations. According to Schammass, the bandwidth of the self-sensing algorithm is limited due to the analog filtering of the demodulation method [5].

The effect of the band-pass filter on the modulated envelope component can be modelled as a first order low-pass filtering effect as described in (3.25),

$$LPF = G\frac{1}{s + \Delta\omega} \tag{3.25}$$

where G is a gain constant and $\Delta\omega$ is half the pass-band of the BPF [5].
The phase effects of the BPF is of concern, since the filter introduces phase shifts and limits the performance of the demodulation process. The effect of this filter is investigated. Figure 3.9 shows an over exaggerated modulated current with a sinusoidal envelope component. This modulated current signal is passed through the demodulation process. The frequency effect

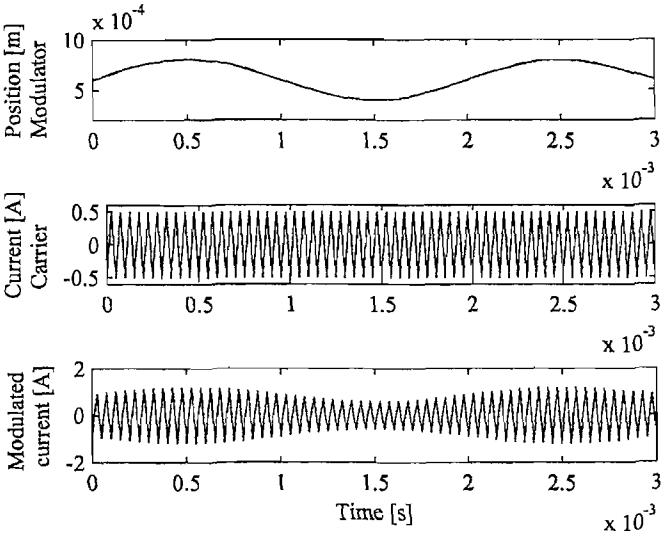

Figure 3.9: Modulated current

of the BPF on the low frequency envelope component is shown in figure 3.10. The BPF has a pass band of 3 kHz thus $\Delta\omega$ of the LPF model is at 1.5 kHz. The phase shift is approximately

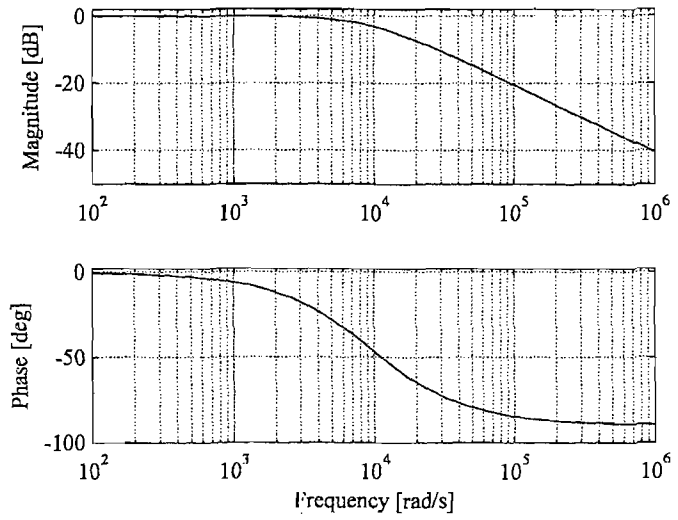

Figure 3.10: Phase shift due to BPF

18 degrees at 500 Hz. From the frequency response it is clear that the BPF pass-band must be chosen at the maximum bandwidth, where the system is still stable and the attenuation is still satisfactory.

Different demodulation techniques are available, which make use of active full wave rectifiers (FWR), wide-band ac to dc converters, synchronous demodulators and rms to dc converters. A

synchronous demodulator is used in this work. The synchronous demodulation technique has two crucial advantages over the diode based demodulators, namely that the internal voltage drop and the nonlinear effects of the diodes are eliminated. The FWR and wide band ac to dc converters make use of diodes. The choice is therefore between the RMS to dc converter and synchronous demodulator. From literature both demodulators were applied in self-sensing research. For this research the synchronous demodulator which make use of an absolute value and a LPF is chosen. The effect of the absolute calculation in the demodulation method will be assumed to be ideal, thus the model of the absolute calculation will not be investigated further.

The high frequency fundamental components are shifted to low frequencies using the demodulator which make use of a LPF. The effect of the LPF will be evaluated in the same way as the BPF. Figure 3.11 shows the frequency response of the second order LPF with a cutoff frequency at 900 Hz. From the results it is clear that the real filter adds a large phase shift to the demod-

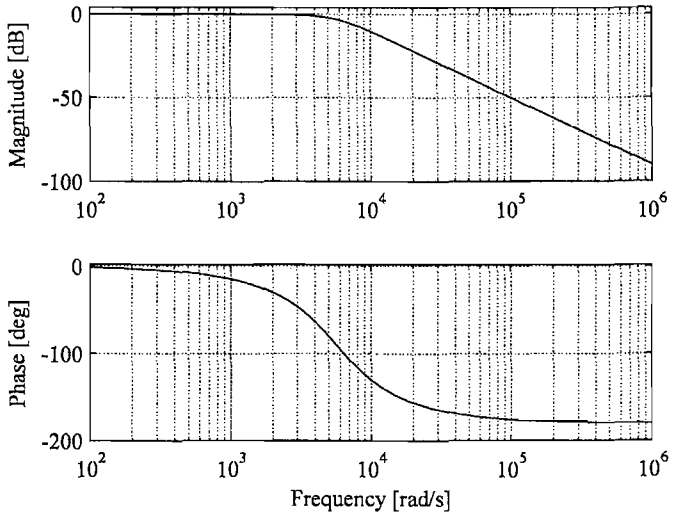

Figure 3.11: Phase shift due to LPF

ulated current envelope. At 500 Hz the phase is approximately 50 degrees. This large phase shift will decrease the performance of the self-sensing AMB system even more.

From the two basic evaluation methods the total open loop phase shift is estimated to be 68 degrees at 500 Hz. This is a very large phase shift in the feedback loop.
Another disadvantage of analog electronics is that it is temperature sensitive which may negatively influence the self-sensing method. The following sections aim to minimize the phase shift and to increase temperature stability.

3.4.2 Digital filtering demodulation method

Figure 3.12 shows the basic operation of the digital filtering demodulation method. The analog signal is passed through an anti-aliasing filter and then the signal is digitized. The digitized signals are passed to the demodulation algorithm which is implemented on the processor. To be able to digitize the current signal, a fast analog to digital converter (ADC) is required since the fundamental component frequency is at 20 kHz. A 1 MHz ADC was chosen to digitize the

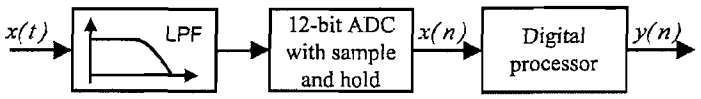

Figure 3.12: Digitization process

high bandwidth analog signal. In the top plot of figure 3.13 the analog current with exaggerated switching noise is used as the analog signal. The analog signal is passed through a 200 kHz anti-aliasing filter and then sampled by the 1 MHz ADC. The results are shown in the bottom plot of figure 3.13. It is assumed that the anti-aliasing filter comprises a first order and a second

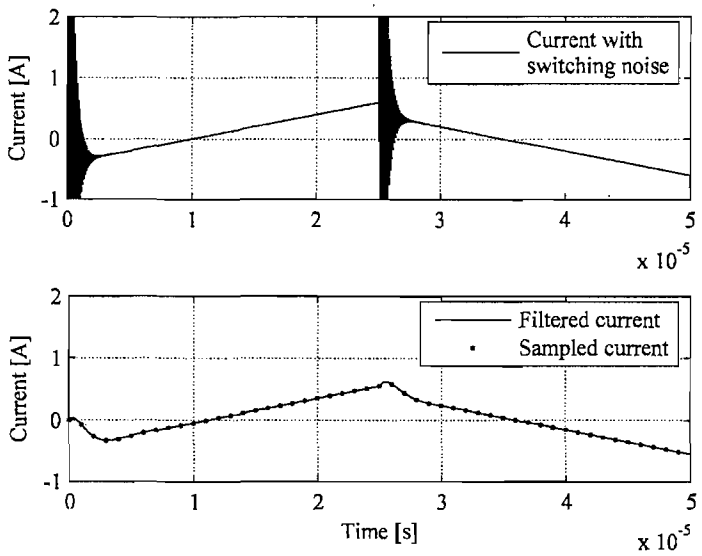

Figure 3.13: Sampling of analog signal

order Butterworth LPF. The first order filter is a LPF with a 200 kHz cutoff frequency which represents the bandwidth of the current sensor used in the practical setup. The second order filter is an analog LPF with a 200 kHz cutoff frequency which is situated after the current sensor to further reduce aliasing. The spectrum magnitude of the combined Butterworth filters is governed by (3.26),

$$|H_{LPF}(f)| = \frac{1}{\sqrt{1+(f/f_c)^{2n}}} \tag{3.26}$$

where f_c is the cutoff frequency and f is the frequency where the magnitude is required. Using (3.26) the aliasing level can be calculated, where f is replaced with $f_a = F_s - f_c = 800$ kHz which is the aliasing frequency. F_s = 1MHz is the sampling frequency and $n = 3$ is the filter order. By substituting the values into (3.26) the aliasing level of 0.0156 is obtained, which results in $(0.0156/0.707)100 = 2.2$ % aliasing in the pass-band.
From the results in figure 3.13 and the 2.2 % pass-band aliasing level estimation the sampling rate is adequate to reproduce the analog signal in digital format.

The advantage of the digitized signal is that different signal conditioning methods can be applied. The digital filtering method is a digital replica of the analog demodulation method, except that the analog filters and demodulation method are replaced with digital filters and a digital demodulation method.

The digital filters can be implemented with IIR or FIR filters. In this work FIR filters are used, since FIR filters are commonly used with Field Programable Gate Arrays (FPGAs). Equation (3.27) shows the transfer function of a FIR filter,

$$H(z) = \sum_{k=0}^{N-1} h(k) z^{-k} \tag{3.27}$$

where $k = 1,2,3...N-1$, N is the filter length, $h(k)$ is the impulse response coefficients. FIR filters have the additional advantage of linear phase shifts.
The analog synchronous demodulation method is replaced by a digital absolute value function.

The main advantage of the demodulation method is that it is not noise or temperature sensitive, and the digital filters are easy to change due to software programmability. The disadvantage of the overall demodulation method is that the phase shifts introduced by the filters are the same as the analog method.

3.4.3 Band-pass sampling demodulation method

The aim of the band-pass sampling method is to eliminate the use of filters in the demodulation path. The band-pass sampling technique makes use of synchronous sampling, which is synchronized with the maximum and minimum values of the fundamental component. This band-pass sampling method was proposed by Schammass and a graphical representation of the method is shown in figure 3.14 [5]. The high frequency current and voltage signals are passed through a BPF to extract the fundamental components. The envelope can be obtained by sampling the peak values of the fundamental components. Since the power amplifier is digitally implemented on the same controller circuit where the sampling takes place, the sampling times can directly be determined from the PWM duty cycle. An update will take place at double the rate of the switching frequency of the power amplifier. Consider the complex band-passed signal in (3.28),

$$r(t) = r_c(t)\cos(\omega_s t) + r_s(t)\sin(\omega_s t) + r_0(t) \tag{3.28}$$

where $r_c(t)$ and $r_s(t)$ are the complex envelope components and r_0 is the low frequency component with the same bandwidth of the band-pass filter. The filtered signal is sampled at the

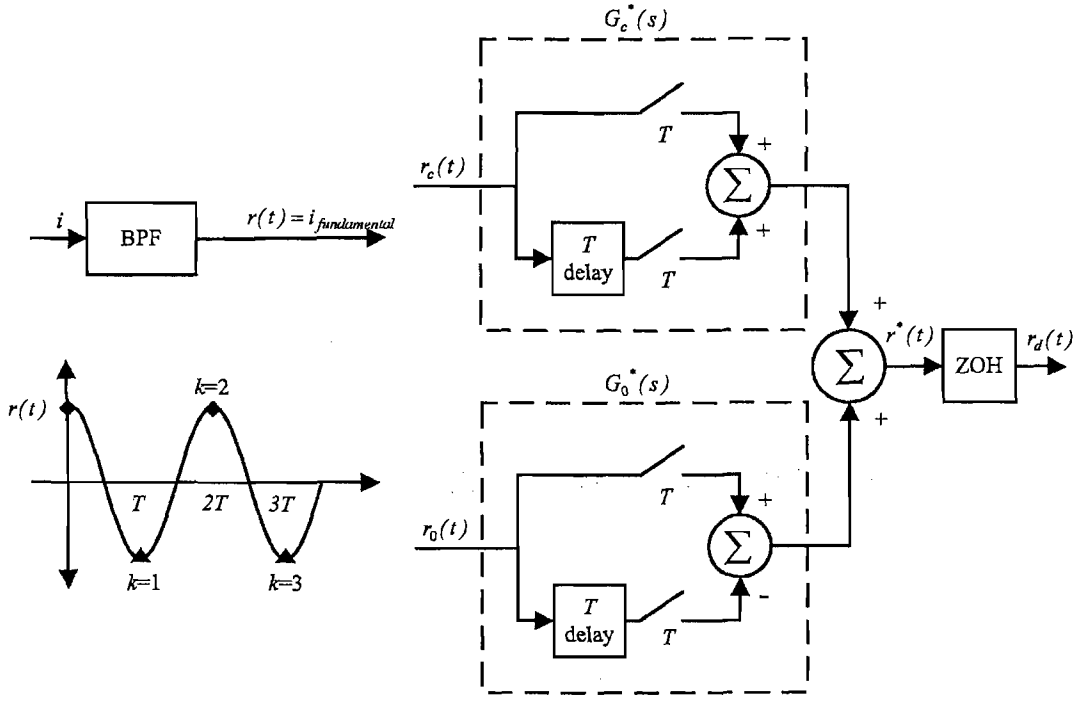

Figure 3.14: Band-pass sampling method

positive [$\diamond$] and negative [$\bigtriangledown$] peak values as shown in figure 3.14. Since low-frequency components influence the band-pass sampling method the effect of low-frequency components is included in the analysis. The signal $r_c(t)$ must be obtained and $r_0(t)$ must be subtracted to eliminate the low-frequency effect. The sampled signal is obtained in (3.29),

$$r_k = (-1)^k[r_c(kT)\cos(k\pi) + r_c(kT-T)\cos((k-1)\pi) + r_0(kT) - r_0(kT-T)] \tag{3.29}$$

where T is $1/(2f_s)$, f_s is the switching frequency and k is the sampling number. In (3.28) it is clear that the signal is inverted with every sample, thus (3.29) can be simplified to

$$r_k = r_c(kT) + r_c(kT-T) + r_0(kT) - r_0(kT-T)]. \tag{3.30}$$

The sampling of the signal and the zero-order hold (ZOH) as shown in figure 3.14, can be represented as an impulse function and a linear function respectively. An equation for $r^*(t)$ is obtained as a series of impulses.

$$r^*(t) = \sum_{k=-\infty}^{\infty} [r_c(t) + r_c(t-T) + r_0(t) - r_0(t-T)]\delta(t-kT) \tag{3.31}$$

From the frequency analysis the transfer functions for $G_c(s)$ and $G_0(s)$ are obtained for the fundamental component as follows [5]:

$$\begin{aligned} G_c^*(s) &= \frac{R^*(s)}{R_c(s)} = \frac{1+e^{-Ts}}{T} \\ G_0^*(s) &= \frac{R^*(s)}{R_0(s)} = \frac{1-e^{-Ts}}{T} \end{aligned} \tag{3.32}$$

By including the ZOH (3.33) is obtained.

$$\begin{aligned} G_{dc}(s) &= \frac{R_d(s)}{R_c(s)} &= \frac{(1+e^{-Ts})(1-e^{-Ts})}{Ts} \\ G_{d0}(s) &= \frac{R_d(s)}{R_0(s)} &= \frac{(1-e^{-Ts})^2}{Ts} \end{aligned} \tag{3.33}$$

From the results obtained the low frequency control component is not only filtered by the BPF, but is additionally filtered by the band-pass sampling demodulation method [5]. The demodulation method eliminates the use of a second order LPF, which is one step closer to eliminating the phase shift due to the LPF used in the digital and analog demodulation methods.

3.4.4 Fast Fourier Transform (FFT) demodulation method

The FFT demodulation method makes full use of the digitized signals by transforming the time domain to frequency domain. The amplitude information at a specific frequency can therefore be easily obtained. The fundamental components of the current and voltage signals are obtained from the FFT calculation as shown in figure 3.15. The rest of the self-sensing technique stays the same as proposed by Schammass. The main purpose of this method is to eliminate all filters in the demodulation path and to eliminate the phase shifts due to the filters. Before

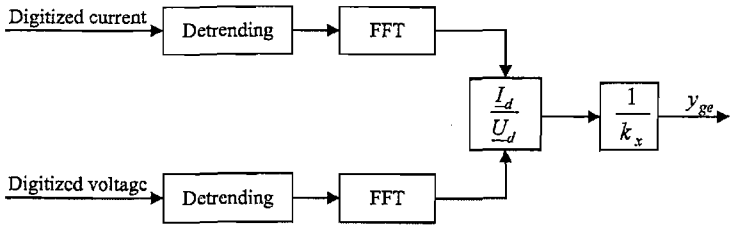

Figure 3.15: FFT demodulation method

the demodulation method is implemented the effect of the sampling rate, aliasing, frequency resolution, sampling length, trend removal and biasing effects on the FFT will be discussed. Each of the above mentioned can have an effect on the accuracy of the FFT and thus on the performance of the self-sensing method.

Sampling rate and aliasing
The effect of an insufficient sampling rate leads to aliasing. Since the fundamental component of the signal is 20 kHz and the maximum sampling rate is at 1 MHz, a third order Butterworth anti-aliasing filter with a cutoff frequency at 200 kHz will be used. By using the Nyquist theorem the sampling frequency must be at least double the maximum frequency component. The sampling rate was found to be sufficient and the same analysis was used as described in section 3.4.2.

Frequency resolution and sampling length
Frequency resolution is defined as the space in frequency between each calculated harmonic

amplitude.

$$f_{res} = \frac{Sampling\ Rate}{FFT\ Points} \tag{3.34}$$

The frequency resolution is of major importance in the FFT method because if it is too low, the harmonic amplitude at the fundamental component may be missed and will result in a picket-fence effect [46]. From (3.34) it is clear that the ratio between the number of FFT points and the sampling rate influences the frequency resolution. Since the hardware is designed for a 1 MHz sampling rate, a 256 point FFT will be implemented due to computational limits. With a sampling frequency of 1 MHz, 5 switching ripple periods can be used in a 256 point FFT calculation. The frequency spacing for a 1 MHz sample rate and a 256 point FFT is 3.98 kHz between each calculated harmonic, with the nearest component to the fundamental frequency (20 kHz) at 1.992 kHz.

Trend and biasing effects

The current signal comprises a low frequency control current and a high frequency switching current as shown in figure 3.16. The scenario where a current signal consists of a control current of 10 A peak to peak with a frequency of 500 Hz and the 20 kHz ripple, will be investigated. If an FFT is obtained from the data as shown in figure 3.16 then the low frequency current

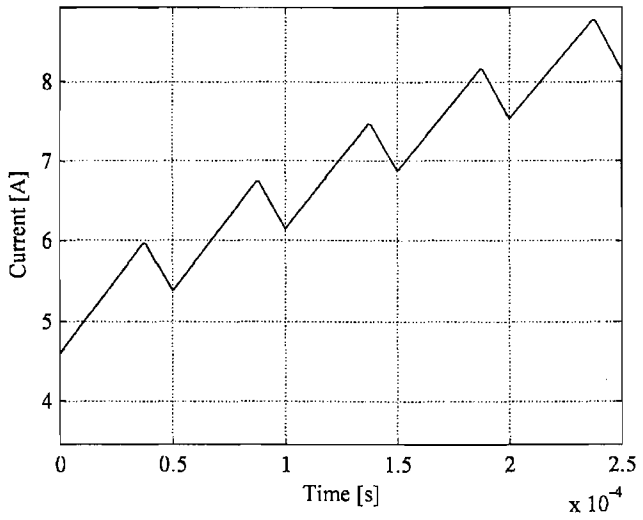

Figure 3.16: Current ripple with low frequency control current

component tends to override the 20 kHz ripple component and the wrong frequency content is obtained. To avoid the effect due to the low frequency current component the sampled current must be detrended. Detrending is the process of obtaining a linear estimation of the trend hidden in the current signal and removing it by subtracting the estimated linear trend. By using linear detrending a more accurate FFT calculation at the switching frequency is obtained. Figure 3.17 shows the effect of detrending. The control current is varied with a 500 and 1500 Hz 10 A sinusoidal current reference and the frequency contents are obtained by a 256 point FFT. From figure 3.17 it is clear that the 500 Hz control current tends to override the 20 kHz switching

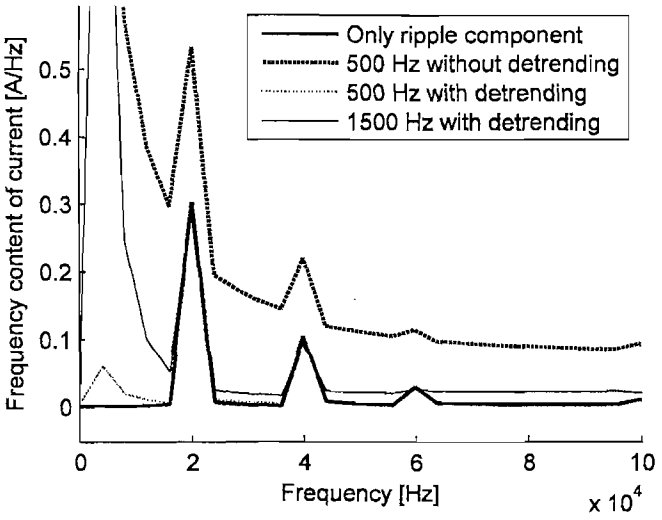

Figure 3.17: FFT with and without detrending

component when no detrending is applied. As stated earlier, detrending is a linear estimation of the trend hidden in a signal. In MATLAB® a detrend function is available to calculate the linear trend. Since the algorithm is implemented on a FPGA, the detrend function must be investigated. The aim of this investigation is to derive a linear detrending function which is optimized to lower the computational intensity on the FPGA. If figure 3.16 is investigated it is clear that the high frequency current is superimposed onto a trend. This trend is the 500 Hz sinusoidal signal. The trend can be estimated by using least squares estimation which is obtained by (3.35)

$$\begin{aligned} y &= a + bz \\ a &= \frac{\sum y \sum z^2 - \sum z \sum zy}{n\sum z^2 - (\sum z)^2} \\ b &= \frac{n\sum zy - \sum z \sum y}{n\sum z^2 - (\sum z)^2} \end{aligned} \tag{3.35}$$

where a and b are coefficients of the linear estimation function, z is the input, y is the output and n is the number of samples [47]. In this case the input is at constant intervals of the sampling rate and the output is the current level at the sampling interval. The number of samples is the same as the number of FFT points. The calculation of the linear function is computationally intensive due to the number of points, but exactly the same result is obtained using the MATLAB® function. One way to reduce the calculation intensity is to reduce the number of samples used to determine the linear estimation. In figure 3.18 a 256 point FFT is used where 256 samples and 7 samples are used to determine the detrending function. The second peak is at the switching frequency which is of concern and from both results an accurate peak value is obtained. A 10 A 1000 Hz sinusoidal reference was used for this evaluation. By using the 7 samples the computational intensity is reduced by a factor of 36.
Now that the FFT calculation is fully understood the position estimation algorithm can be implemented. The FFT calculation replaces the BPF, the synchronous demodulator and the LPF.

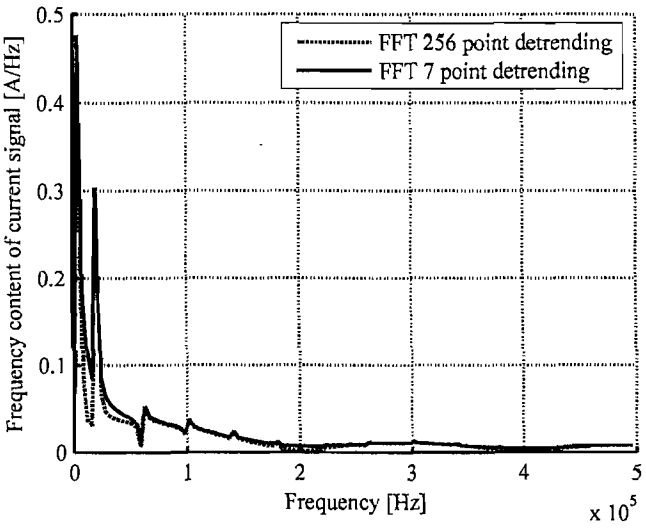

Figure 3.18: 256 and 7 point detrending

The rest of the self-sensing algorithm stays the same as proposed by the digital implementation method.

3.5 The gradient self-sensing approach

The gradient self-sensing approach makes use of a high bandwidth inverse model and high speed sampling. The self-sensing algorithm will be derived and the implementation of the method will be discussed in detail. The self-sensing algorithm is divided into two sections namely the linear model and the nonlinearities.

3.5.1 Linear model

By using (3.8) and obtaining its inverse it is clear that the position of the rotor can be determined. In this case it is assumed that the relative permeability of the material (μ_r) is a constant and all other nonlinear effects are omitted. The inductance of the coil is obtained by (3.36).

$$L = N\frac{\partial \phi}{\partial i} = \frac{\mu_0 N^2 A}{2(g_0 + x) + l_m/\mu_r} \tag{3.36}$$

By rewriting (3.8) the inverse can be written as follows,

$$L = \frac{(u - Ri)}{di/dt} \tag{3.37}$$

where L is described in (3.36). From (3.36) and (3.37) the position can be obtained directly by measuring the change of the current i through and the voltage u across the the coil.

The effect of the coil resistance must be investigated to predict the effect on the estimated position. The maximum low frequency current of the AMB system is 10 A and the coil resistance is approximately 0.2 ohm. By neglecting the coil's resistance and the the low frequency current, a maximum error of 2 % is made. The maximum high frequency change in the current is approximately 400 mA. This introduces an error of 0.08 % if the coil resistance is neglected. The high and low frequency current components are neglected in the algorithm. By rewriting (3.37) the following is obtained.

$$L = \frac{(u)}{di/dt} \tag{3.38}$$

In figure 3.19 the sampling of the current is shown. The 75 % to 100 % range of the current's period is used for sampling since the power amplifier's duty cycle is limited to between 25 % and 75 %. The last 25 % of the current is sampled, since the least change of transients will take place at the end. The only case of transients present is when the duty cycle operates near 75 %. By using (3.38) the position of the rotor can be determined by the change rate alone. The power

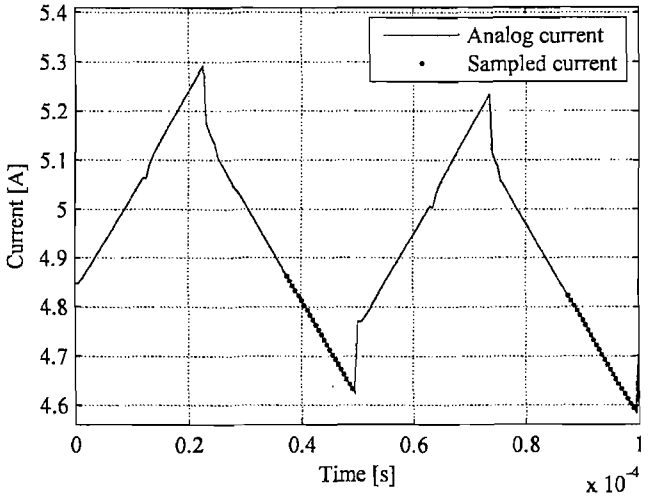

Figure 3.19: Sampled gradient

amplifier voltage u applied to the coils will be assumed to be a constant value.

The self-sensing algorithm estimates a position output once every switching period. By using (3.38) and (3.36) and solving the equation relative to the change in position, (3.39) is obtained.

$$x_{est} = \frac{\mu_0 N^2 A}{\frac{2u}{di/dt}} - (2g_0 - l_m\mu_r)/2 \tag{3.39}$$

In (3.39) it is assumed that μ_r is a constant value. Since the nonlinear effect due to μ_r is neglected it must be investigated.

3.5.2 Nonlinearities

In this section the nonlinear effects due to μ_r will be investigated and a compensation method will be derived. The following effects will be investigated: 1) the eddy currents and 2) the change in amplitude due to hysteresis and saturation.

Eddy currents.
Eddy currents can be viewed as abrupt changes at the instance where the switch mode power amplifier switches from one stage to another. By sampling at convenient sampling intervals as described in figure 3.13 the gradient can be isolated and the abrupt changes due to the eddy currents can be eliminated. By using this method the effect due to the eddy currents is automatically eliminated.

Relative magnetic material permeability.
The changing effect due to μ_r on the position cannot easily be eliminated, since it is dependent on the specific AMB design and on the material used to construct the AMB. In simulation a high bandwidth hysteresis model can be implemented to model the effect of μ_r. The same model may be used to estimate the hysteresis in the real system. The problem with this method is that the hysteresis model is computationally intensive, thus it will increase performance demand on the processor and the model may drift away from the practical system. This method will not be investigated further.
The second method is to use a nonlinear function to model the saturation of the magnetic material as proposed in 3.3.1. The major difference between the method proposed in this section and in section 3.3.1 is that the model in this section is not implemented with an inverse frequency shifted model. The effect of the high bandwidth method must first be investigated.
The effect due to the 20 kHz current ripple on the hysteresis loop is only very small minor loops, where the control current with a bandwidth of 500 Hz has a large effect on the major loops. A typical effect due to the 20 kHz current ripple and the 500 Hz control current is shown in figure 3.20. From figure 3.20 and by using the ripple amplitude to maximum control cur-

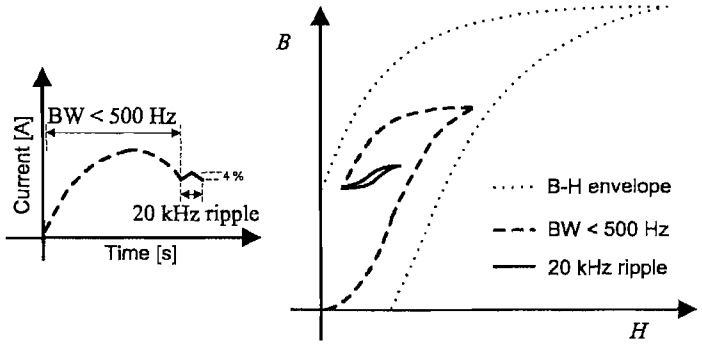

Figure 3.20: Hysteresis loops

rent ratio it is clear that the control current has a much larger effect on the hysteresis curve. The ripple is approximately 4 % of the total current range. Thus the assumption to neglect the high frequency current component can be justified. Saturation due to low frequency currents

will be included, but hysteresis of the low frequencies will be neglected due to computational intensiveness.

The same material compensation method is applied as discussed in section 3.3. The input of the nonlinear saturation function is the estimated flux, which is estimated by using (3.23). The same method is followed as discussed in section 3.3.1 to obtain the nonlinear position change (3.22) due to the nonlinear magnetic material. Figure 3.21 shows the basic block diagram of the gradient self-sensing scheme. The inverse model is as derived in (3.39).

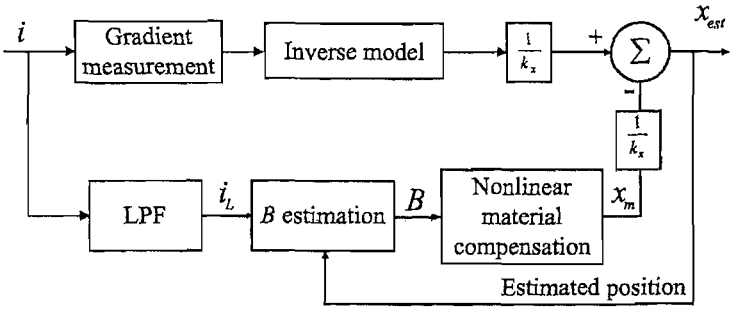

Figure 3.21: Gradient self-sensing technique

3.5.3 Implementation limits

In this section the theoretical limitations of the hardware will be discussed.
The ripple to current ratio is approximately in the range of 4%. Due to this ratio the accuracy of measurements will have a large effect on the performance of the position estimation algorithm. Thus the effect due to the finite word length of the ADCs must be investigated.
In the hardware implementation digitization consists of a true bipolar 12 bit ADC with an input range of ±5 V. The analog current has an operating range of 0-10 A which is sensed by a LEM sensor and scaled to ±5 V to match the ADC inputs. Since the current and the ADC both have a range of 10, the resolution of the current can directly be obtained by (3.40).

$$\begin{aligned} ADC_{res} &= \frac{\Delta I}{2^B} \\ &= \frac{10}{2^{12}} \\ &= 2.44\,\text{mA} \end{aligned} \tag{3.40}$$

As stated before, the ripple is approximately 4% of the total current which leads to a 400 mA ripple component. It is assumed the current change is 50 %, thus the minimum ripple is 200 mA. From this assumption the ripple amplitude has a changing range of 200 mA. From (3.40) the ADC has a resolution of 2.44 mA, which leads to a ripple resolution of 82 levels. From this the maximum obtainable position resolution is 14 μm. A general formula for the position resolution is shown in (3.41),

$$x_{res} = \frac{\Delta x}{\Delta V_{ripple}/(\frac{\Delta V_{ADC}}{2^B})} \tag{3.41}$$

where Δx is total change in position, ΔV_{ripple} is the change in the current ripple converted to voltage and ΔV_{ADC} is the current converted to the ADC's input voltage range. The same conversion is used for ΔV_{ADC} and ΔV_{ripple}.

A better position resolution can be obtained by subtracting the low frequency control current from the total current to isolate the ripple component. The ripple component can then be amplified and digitized. Since the subtraction and amplification must be implemented with analog electronics the analog electronics bandwidth was simulated. From the simulation results it is found that the slightest filtering effect has an enormous effect on the gradient. From these simulation results it is found that the gradient method will be difficult to implement in practice.

3.6 Direct current amplitude measurement method

The motivation for the direct current ripple measurement method is to reduce phase shift produced by demodulation methods. In the DCM self-sensing scheme a new PWM switching method is implemented, which enables the estimation of the rotor position with only one current measurement. The DCM technique has also the added benefit of less sensitivity for cross-coupling effects. In the following sections the PWM switching method, the method to eliminate the control current, scaling and limitations are discussed.

3.6.1 Motivation

From literature and practical experience it is known that the high frequency current ripple produced by switch mode power amplifiers is modulated by the position. In most research the high frequency components are demodulated by some sort of amplitude demodulation method. Most of the demodulation methods make use of filtering. Assuming all electronic components are ideal and temperature insensitive, phase shifts exist due to the filters and have a large effect on the self-sensing performance. Thus by eliminating all filters, the performance of the self-sensing method can be improved. The proposed self-sensing method makes use of basic mathematical operations and no low frequency filters will be used in the demodulation process.
The aim of this method is to use as little external components as possible to increase reliability and simplify the analog circuitry. In the DCM self-sensing technique only the current through a coil is measured to estimate the rotor position. The proposed direct current measurement (DCM) method will be discussed in the next section.

3.6.2 Direct current measurement

The basic AMB model derived in (3.8) will be used as basis for the DCM method. From (3.8) it is clear that the position of the rotor can be obtained by model inversion. In this case it is assumed that the relative magnetic material permeability μ_r of the material is constant and all

other nonlinear effects are omitted at this stage. The effect of the coil resistance will also be neglected, thus current through the coil is as follows:

$$\frac{di}{dt} = \frac{2x_g + l_m/\mu_r}{\mu_0 N^2 A}(u). \tag{3.42}$$

The DCM method also relies on the modulated amplitude of the high frequency current ripple component. Since the DCM method relies only on the current, the effect of duty cycle modulation must be eliminated without using a nonlinear controller and the voltage measurement. In the following subsections the effect of the duty cycle modulation and the demodulation process will be discussed.

Current waveform and duty cycle effects

Figure 3.16 shows a typical current response of an AMB system where a desired control current is required and the duty cycle changes continuously to maintain the desired current level. The control component has a maximum of 10 A and is much larger than the high frequency ripple component which has a maximum of 400 mA approximately.

When the duty cycle changes the amplitude of the ripple current is nonlinearly modulated as proved in section 3.2. Thus the current ripple cannot be directly used to obtain an estimated position. A novel method to overcome the nonlinear duty cycle modulation effect is to force the duty cycle to 50 %. By using the change in the high frequency current ripple amplitude the rotor position can be estimated. If the duty cycle is always 50 % controllability will be lost, but by switching one cycle at 50 % for position sensing purposes and another cycle for control, the nonlinear duty cycle dependency is overcome and controllability is maintained.
Since the method forces one switching cycle to 50 % it will have some effect on the maximum performance of the AMB. Figure 3.22 illustrates the PWM switching of one position sensing cycle forced to 50 % duty cycle and one control cycle at 75 % duty cycle.

Control current elimination (Demodulation)

The control current is usually eliminated by passing the current through an analog BPF, but in this analysis a different method is used to eliminate possible phase shifts. The mean value of each position sensing cycle is calculated and it is subtracted from the same position sensing cycle. The result is only the high frequency ripple current as described by (3.43),

$$i_r = i_{sense} - mean(i_{sense}) \tag{3.43}$$

where i_{sense} is the sampled data from the sensing cycle. Figure 3.23 shows the remaining high frequency ripple when the mean value is subtracted from the position sensing cycle. The maximum value $I_{r_{max}}$ of I_r can be rescaled to estimate the position, since the amplitude of $I_{r_{max}}$ is dependent on the change in position.

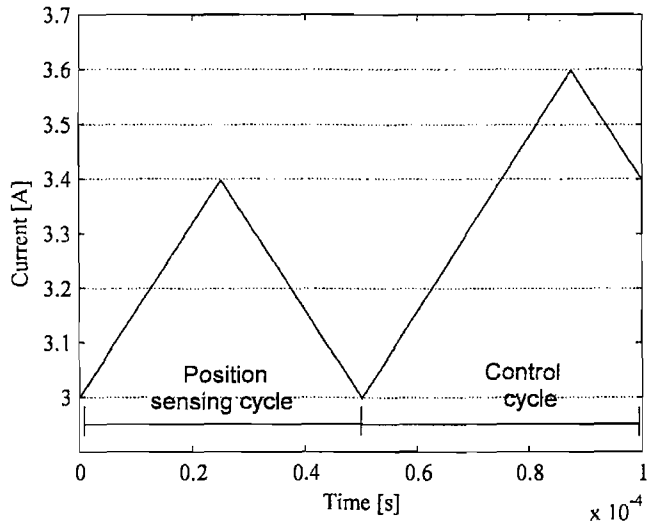

Figure 3.22: Position sensing and control cycle

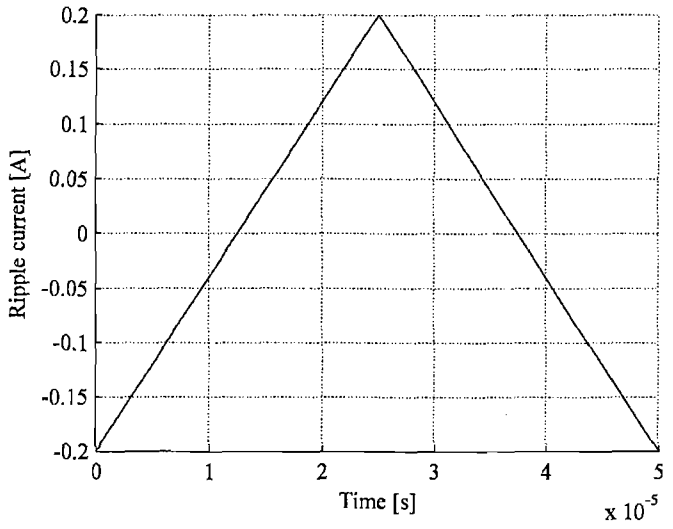

Figure 3.23: High frequency ripple component

3.6.3 Scaling and nonlinear compensation

For this research the same least squares method is used as proposed in section 3.3.1 due to saturation and eddy current effects. The only difference is that $\underline{I_u} = \underline{I_d}/\underline{U_d}$ is replaced by $I_{r_{max}}$. With the nonlinear effects neglected (3.21) can be rewritten and (3.44) is obtained.

$$x_{ge} = \frac{1}{k_x} I_{r_{max}} \tag{3.44}$$

With the nonlinearities included (3.45) is obtained where the nonlinear effect on the ripple component $I_{r_{max}}$ due to the changing flux is subtracted from the linear estimation.

$$x_{est} = x_{ge} - x_m = \frac{1}{k_x}(I_{r_{max}} - k_{b2}B_e^2 - k_{b1}B_e - k_{b0}) \tag{3.45}$$

Figure 3.24 shows the basic block diagram of the DCM self-sensing technique. The mean and maximum are determined in each 50 % sensing cycle.

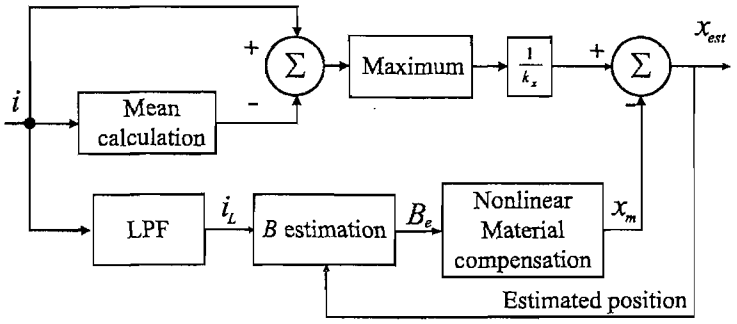

Figure 3.24: Block diagram of DCM self-sensing technique

3.7 Performance limitations of the DCM technique

In this section some practical implications will be discussed together with their effects on the performance of the self-sensing method. A practical difficulty is the current measurements and how to use the ADC to its maximal resolution. As mentioned before the self-sensing method relies on one position sensing cycle where the duty cycle is at 50 % and the next cycle is used for control. The effect on the AMB's performance due to the 50 % PWM forced sensing cycle will also be investigated.

3.7.1 Current sensing and digitization

For the self-sensing technique the current is measured using an LAH25-NP current LEM sensor. The bandwidth of the LEM sensor is approximately 200 kHz. Practical measurements were obtained using a current probe with the oscilloscope sampling time set to 250 MS/s. The current probe measurements are viewed as the real current. The real current is put through a 1st order low-pass filter with a cutoff frequency at 200 kHz, which simulates the LEM sensor bandwidth. The LEM sensor output is assumed to be the same as the filtered output. From figure 3.25 the output of the LEM sensor is sufficient for the self-sensing application. There is a small deviation due to the 200 kHz bandwidth. The benefit of the 200 kHz bandwidth is that most of the high frequency noise is removed by the sensor. The filtering effect of the LEM sensor and a second order LPF with a 200 kHz cutoff frequency acts as an anti-aliasing filter

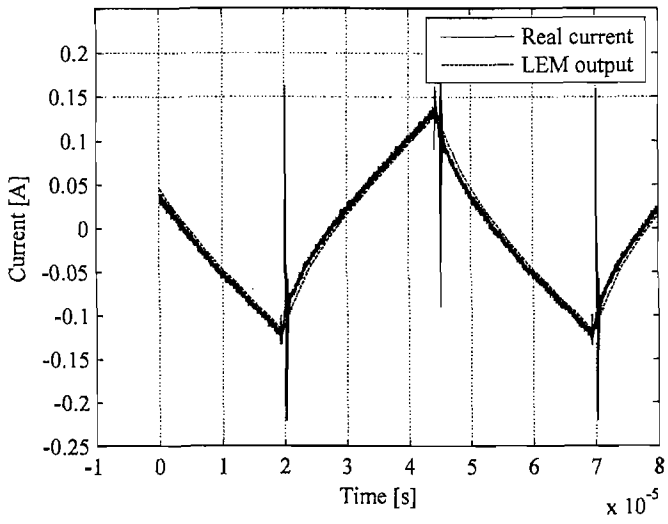

Figure 3.25: Current sensor output

before the signal is digitized by the ADC.
The filtered LEM sensor output is passed through a true bi-polar 12 bit plus sign bit ADC. In the AMB system the control current will vary from 0 to 10 A. Due to the control current to ripple ratio the resolution of the ripple component is relatively low.
Two possible implementations are investigated to increase the resolution. The implementation of the two methods are shown in figure 3.26.

Method 1
In the analysis the amplitude of the current is low-pass filtered and subtracted from the full bandwidth current before digitizing. The low-pass filter used in the subtraction must be designed to minimize phase shift in the control frequency range and the ripple must be attenuated enough so that the switching ripple is eliminated. The result of the subtraction is only the high frequency ripple component which can be amplified to the ADC input range. It is suspected that the filter dynamics will have an effect on the stability.

Method 2
This analysis is also based on method 1 where the amplitude of the control current is subtracted from the high frequency component before digitization. In this method the LPF is replaced by a digital to analog converter (DAC). The digitized control feedback signal of the power amplifier is used to obtain the dc level at the specific instance. The control current level is converted to an analog value using the DAC. This analog value is then subtracted from the full bandwidth sensing cycle. The result is the high frequency ripple component. The ripple component can then be amplified to the ADC's full input range. The advantage of the DAC method is that dynamic effects of the LPF are eliminated. The disadvantage of the DAC method is that a DAC with digital paths must be routed to the analog circuit and the layout becomes more complex.

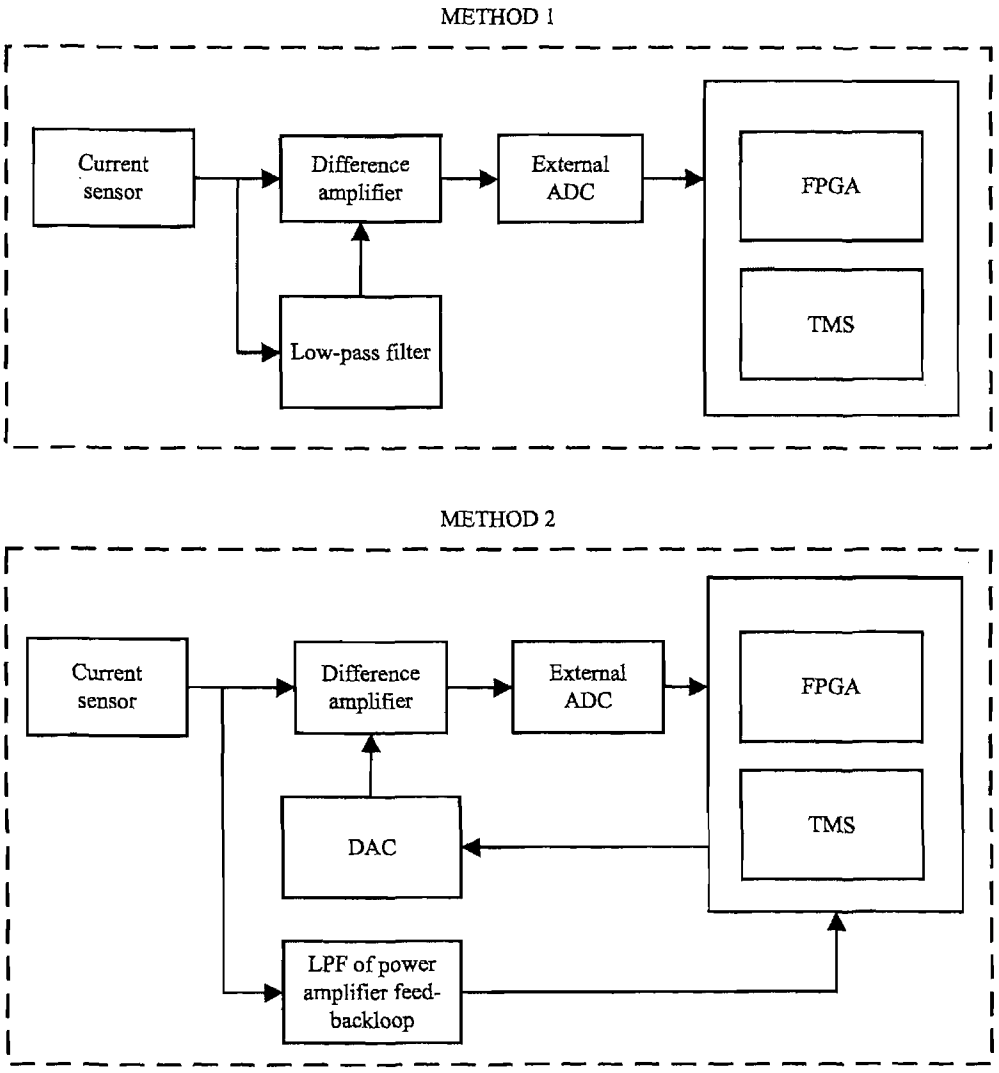

Figure 3.26: Low frequency elimination methods

3.7.2 Dynamic effect due to sensing cycle

The DCM self-sensing method requires a 50 % duty cycle when the current ripple is sensed. If this is viewed in terms of the dynamics of the AMB the maximum dynamic force applied over time will be affected. The voltage across the coil is analyzed. For normal operation the voltage across the coil per control cycle is as follows,

$$V_{coil} = V_s(2\alpha - 1) \tag{3.46}$$

where V_s is the switching voltage and α is the duty cycle. In the DCM method one PWM cycle is at 50 % duty cycle which is used as the position sensing cycle and one cycle is for control.

The voltage across the coil for the two cycles is calculated as follows.

$$\begin{aligned} V_{coil} &= V_s \frac{(2 \cdot 0.5 - 1) + (2\alpha - 1)}{2} \\ &= V_s \frac{(2\alpha - 1)}{2} \end{aligned} \tag{3.47}$$

From (3.47) the power amplifier's average voltage is two times lower when the DCM self-sensing technique is implemented with a sensing cycle at 50 % duty cycle. This is a drawback, but the self-sensing method's performance is estimated to be high. In all the other self-sensing schemes the duty cycle is limited between 25 % and 75 % which also halves the slew rate. Thus the 50 % sensing cycle of the DCM technique does not decrease the performance more than the other self-sensing schemes.

3.8 Self-sensing algorithm stability

In this section the stability of the self-sensing algorithm is investigated. To determine the stability of the algorithm the self-sensing loop must be linearized. The first section describes the linearization of the algorithm and the second section describes the stability of the algorithm.

3.8.1 Self-sensing loop linearization

In all the self-sensing schemes a nonlinear compensation function is used to compensate for the material nonlinearities. In this nonlinear compensation method a delayed sample of the position is used to determine the estimated flux. Before the loop can be analyzed, the nonlinear system must be linearized. To linearize the estimation loop the nonlinear material compensation function $f_m(B) = k_{b2}B^2 + k_{b1}B^2 + k_{b0}$ must be linearized. By linearizing the nonlinear function around the center position and around the bias current level (i_{c0}), the demodulated current can be written in linearized form as shown in (3.48).

$$f_m(i_{i_{c0},g_0}) = k_{mi} i_{co} + k_{mx} x \tag{3.48}$$

k_{mi} and k_{mx} are obtained by the linearization process as follows:

$$\begin{aligned} k_{mi} &= 2k_{b2}\left(\frac{\mu_0 N}{2g_0} + \frac{L_s}{NA}\right)^2 i_0 + k_{b1}\left(\frac{\mu_0 N}{2g_0} + \frac{L_s}{NA}\right) \\ k_{mx} &= 2k_{b2}\left(\frac{\mu_0 N}{2g_0} + \frac{L_s}{NA}\right)\frac{\mu_0 N}{2g_0^2} i_0^2 + k_{b1}\frac{\mu_0 N i_0}{2g_0^2} \end{aligned} \tag{3.49}$$

The linearized estimated position can be written as in (3.50).

$$x_m = \frac{1}{k_x} f_m(i_{ec0_{LPF}}, x_{est}) = \frac{k_{mi}}{k_x} i_{ec0_{LPF}} + \frac{k_{mx}}{k_x} x_{est} \tag{3.50}$$

$i_{ec0_{LPF}} = i_{e0} + i_0$ is the estimated control current which is passed through a LPF which represents the low-pass effect of the demodulation method. Since one delayed estimated position sample is used to determine the flux, the z-transform of (3.50) must be determined. Figure 3.27 shows

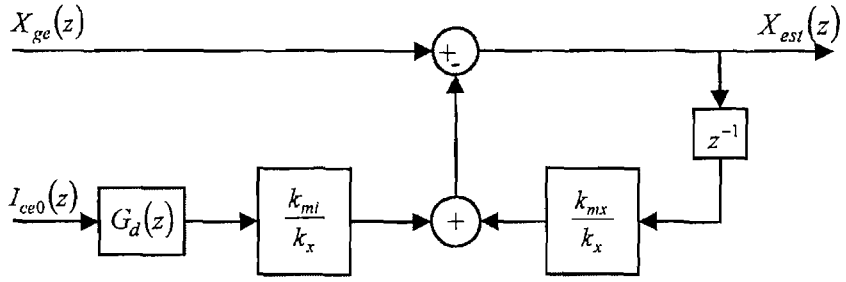

Figure 3.27: Self-sensing algorithm block diagram

the block diagram of the self-sensing algorithm in the z-domain. $G_d(z)$ represents the LPF due to the demodulation effect in the z-domain. From figure 3.27, (3.51) is obtained.

$$X_m(z) = \frac{k_{mi}}{k_x} I_{ec0}(z) G_d(z) + z^{-1} \frac{k_{mx}}{k_x} X_{est}(z) \tag{3.51}$$

Rewriting (3.24) by using the linearized material compensation function, (3.52) is obtained.

$$\begin{aligned} X_{est}(z) &= X_{ge}(z) - X_m(z) \\ &= X_{ge}(z) - \frac{k_{mi}}{k_x} I_{ec0}(z) G_d(z) - z^{-1} \frac{k_{mx}}{k_x} X_{est}(z) \end{aligned} \tag{3.52}$$

Since a linearized self-sensing algorithm is obtained the stability of the algorithm can be analyzed.

3.8.2 Algorithm stability

By using the results obtained in (3.52) the closed loop transfer function can be obtained. From figure 3.27 it is clear that the algorithm is dependent on the demodulated position $X_{ge}(z)$ and the current $I_{ec0}(z)$. The closed loop transfer function $T_{X_{ge}}(z)$ in (3.53) is obtained by setting $I_{ec0}(z) = 0$ and $T_{I_{ec0}}(z)$ in (3.54) is obtained by setting $X_{ge}(z) = 0$.

$$T_{X_{ge}}(z) = \frac{X_{est}(z)}{X_{ge}(z)} = \frac{z}{z + \frac{k_{mx}}{k_x}} \tag{3.53}$$

$$T_{I_{ec0}}(z) = \frac{X_{est}(z)}{I_{ec0}(z)} = -\frac{k_{mi}}{k_x} G_d(z) \frac{z}{z + \frac{k_{mx}}{k_x}} \tag{3.54}$$

In (3.53) the characteristic equation is $\lambda = z + \frac{k_{mx}}{k_x}$, thus the algorithm will always be stable if the ratio of $\frac{k_{mx}}{k_x}$ results in a pole placement inside the unity circle. The input $X_{ge}(z)$ is a bounded input due to the 25 % and 75 % duty cycle limits, thus $X_{ge}(z)$ will not lead to an unstable input.

In (3.54) the characteristic equation is the same as in (3.53). The algorithm will always be stable if the ratio of $\frac{k_{mx}}{k_x}$ results in a pole placement inside the unity circle and $G_d(z)$ is bounded. The input $I_{eco}(z)$ is a bounded input due to the power amplifier limits and $G_d(z)$ is a LPF which is designed to be stable.

From the two sensitivity analyses it was found that the characteristic equation determines the stability. From this the ratio $\frac{k_{mx}}{k_x}$ must be smaller than one to ensure that the system is Schur stable [48]. The digital implementation of $G_d(z)$ for the different self-sensing schemes will be discussed in chapter 4 for each self-sensing technique.

3.9 Cross-coupling

In this section the effect of cross-coupling on different self-sensing techniques are investigated and the negative effect is quantified using mutual inductance terms. The effect of flux distribution and duty cycle variation will be investigated.

3.9.1 Reluctance model

Figure 3.28 shows the reluctance network of the eight pole radial magnetic bearing as shown in figure 3.1. The model is arranged in a NSSNNSSN configuration . For this analysis the magnetic material is assumed to be linear, thus fringing effects and cross-coupling due to the stator geometric curve are neglected. Due to the linearity assumption and the symmetrical properties of a radial bearing, the reluctances of the network can be reduced to three material reluctances ($\Re_S, \Re_P, \Re_R$) and four air gap reluctances ($\Re_{g_1}, \Re_{g_2}, \Re_{g_3}, \Re_{g_4}$) as described in appendix A. Since the magnetic circuit is equivalent to an electric circuit, the mesh-current method can be used to solve the network. Nine flux paths are identified and by applying Kirchhoff's voltage law around the nine meshes, nine equations are obtained as shown in appendix A equation (A.1). The flux through mesh 1, 2, 3 and 4 is of importance for this analysis. The mesh results obtained from the symbolic analysis are as follows:

$$\phi_k = G_{(k,l)}(t)\Im_1(t) + G_{(k,l)}(t)\Im_2(t) + G_{(k,l)}(t)\Im_3(t) + G_{(k,l)}(t)\Im_4(t) \tag{3.55}$$

where $G_{(k,l)}(t)$ is the l^{th} gain due to the material reluctance, air gap reluctance and $\Im_l$ which is the l^{th} mmf. k is equal to the specific meshes which cross-coupling is investigated. The derivation of (3.55) is shown in appendix A.

3.9.2 Cross-coupling due to flux distribution

Cross-coupling is a quantifiable amount of flux coupling which takes place between the four coils when currents are applied to the coils. For this analysis ϕ_1 will be evaluated over the position range of -200 μm to 200 μm. Figure 3.29 shows the changing gains when the position is varied in the horizontal x-axis. The mmf of the coil at the plot position is set to one and the rest are set to zero to obtain the influence of the specific mmf on ϕ_1. The gain $G_{(1,l)}(t)$ is plotted at the coil position where the mmf is set to one. The mmf's are oriented in the same way as in figure A.1. Figure 3.30 shows the changing gains when the position is varied in the y direction. Again the mmf is set to one and the rest are set to zero and $G_{(1,l)}(t)$ is plotted at the

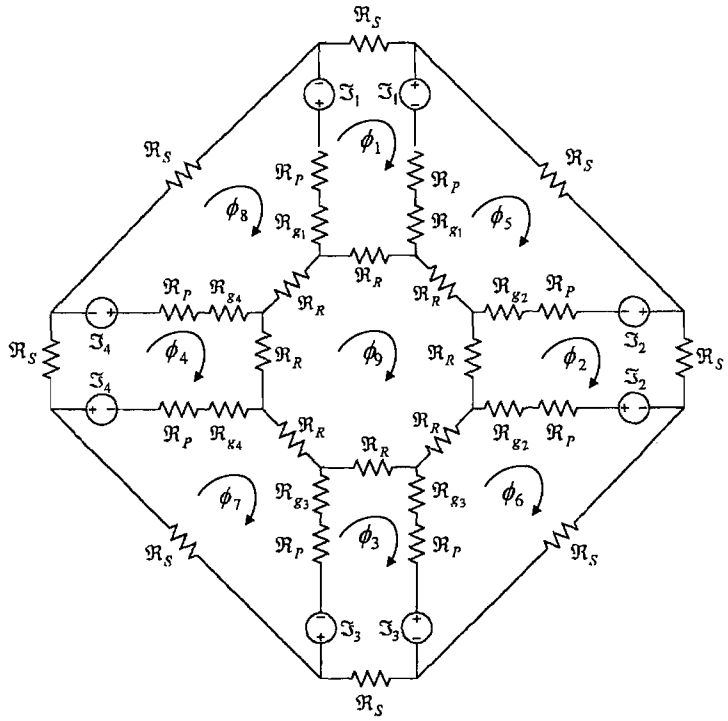

Figure 3.28: Reluctance network

mmf set to one. From figure 3.29 and 3.30 the gains are nearly constant in the axis that is not varied. This is due to the linear reluctance model assumption and axis air gap independency. From this analysis it is clear that an increase in *mmf* in one coil affects all flux paths. This flux distribution is purely dependent on the reluctances and the *mmf* level.

3.9.3 Cross-coupling due to duty cycle variation

Since the DCM self-sensing technique estimates the position in a cycle in which all duty cycles are at 50 %, the cross-coupling effect due to duty cycle variation is investigated. By using Faraday's law the voltage across the coil is determined by the following equation:

$$v_1(t) = N\frac{d\phi_1(t)}{dt} + Ri_1(t) \tag{3.56}$$

where R is the coil resistance and $i_1(t)$ is the current through the coil.

Substituting $\phi_1(t)$ of (A.5) into (3.56), (3.57) is obtained.

$$v_1(t) = N\frac{d}{dt}\left(G_{(1,1)}(t)\Im_1(t) + G_{(1,2)}(t)\Im_2(t) + G_{(1,3)}(t)\Im_3(t) + G_{(1,4)}(t)\Im_4(t)\right) + Ri_1(t) \tag{3.57}$$

Substituting $\Im_l = Ni_l(t)$ into (3.57), (3.58) is obtained.

$$v_1(t) = N^2\frac{d}{dt}\left(G_{(1,1)}(t)i_1(t) + G_{(1,2)}(t)i_2(t) + G_{(1,3)}(t)i_3(t) + G_{(1,4)}(t)i_4(t)\right) + Ri_1(t) \tag{3.58}$$

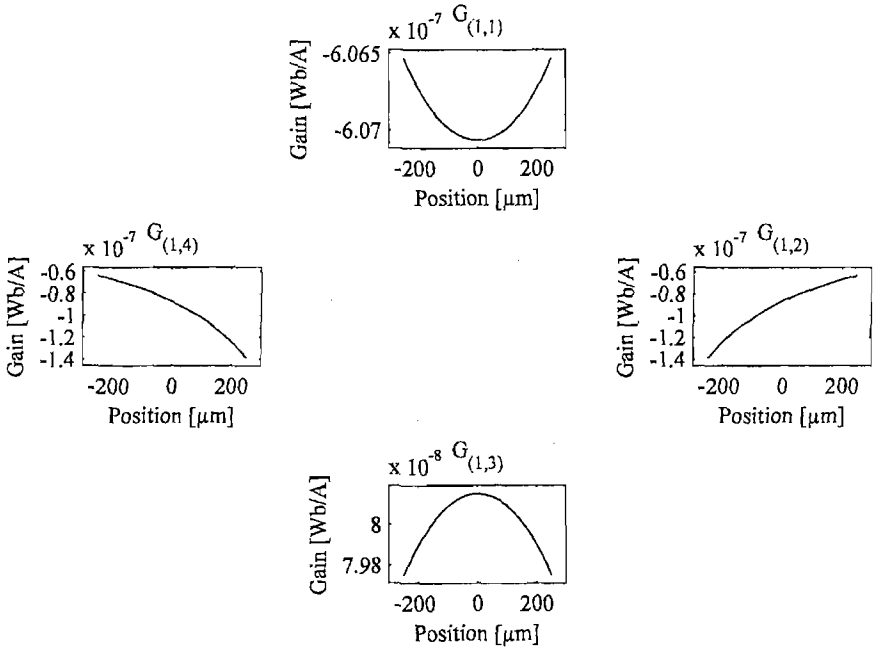

Figure 3.29: Reluctance gain evaluation: x-axis

Since $L = \frac{N^2}{\Re}$ and $N^2G_{(1,1)}(t) = L_1(t)$, $N^2G_{(1,2)}(t) = M_{(1,2)}(t)$, $N^2G_{(1,3)}(t) = M_{(1,3)}(t)$ and $N^2G_{(1,4)}(t) = M_{(1,4)}(t)$, (3.58) can be written in terms of mutual inductances.

$$\begin{aligned} v_1(t) = L_1(t)\frac{di_1(t)}{dt} + M_{(1,2)}(t)\frac{di_2(t)}{dt} + M_{(1,3)}(t)\frac{di_3(t)}{dt} \\ + M_{(1,4)}(t)\frac{di_4(t)}{dt} + Ri_1(t) \end{aligned} \tag{3.59}$$

Rewriting (3.59) in term of fluxes, ϕ_1 is determined by (3.60).

$$\frac{d\phi_1(t)}{dt} = \frac{v_1(t) - Ri_1(t)}{N} - \frac{d\phi_{M_{(1,2)}}(t)}{dt} - \frac{d\phi_{M_{(1,3)}}(t)}{dt} - \frac{d\phi_{M_{(1,4)}}(t)}{dt} \tag{3.60}$$

By rewriting Faraday's law the current through coil 1 is determined by (3.61).

$$i_1(t) = \frac{V_1(t)}{R} - \frac{N}{R}\frac{d\phi_1}{dt} \tag{3.61}$$

Substituting (3.60) into (3.61) the current through coil 1 is expressed in terms of the fluxes and mutual inductances.

$$i_1(t) = \frac{v_1(t)}{R} - \frac{N}{R}\left(\frac{v_1(t) - Ri_1(t)}{N} - \frac{d\phi_{M_{(1,2)}}(t)}{dt} - \frac{d\phi_{M_{(1,3)}}(t)}{dt} - \frac{d\phi_{M_{(1,4)}}(t)}{dt}\right) \tag{3.62}$$

From (3.62) the change in duty cycle variation will result in a change in the sum of the fluxes which will have an effect on all gradients of the current ripples. Lets assume for this analysis that coil 1 is used for self-sensing and it is switched at 50 % duty cycle. If one of the other coils

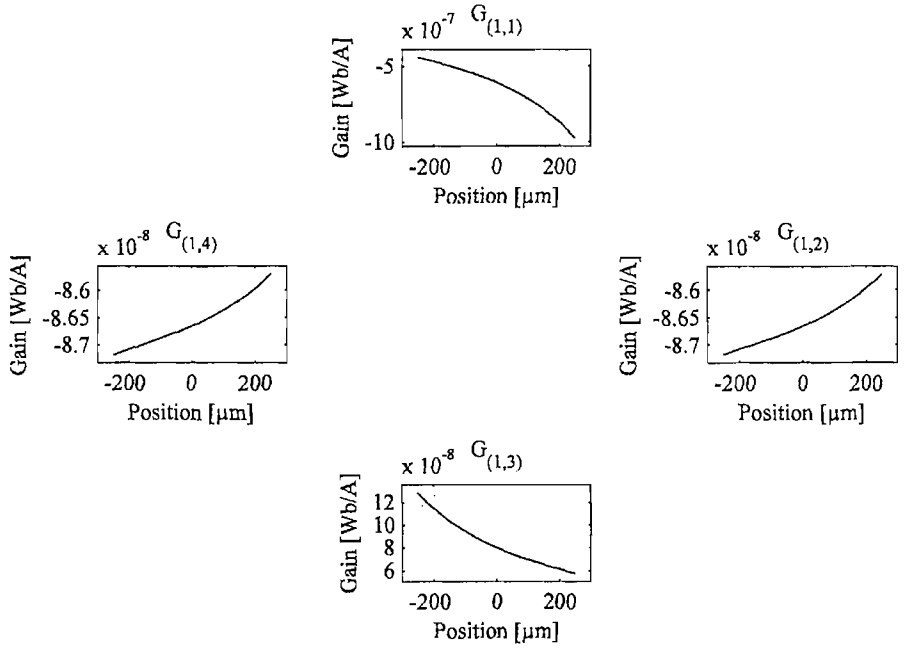

Figure 3.30: Reluctance gain evaluation: y-axis

is switched at a different duty cycle, it will couple in onto the sensing ripple. The amount of coupling is dependent on the mutual coupling constant and the duty cycle variation from the 50 % sensing cycle. By switching all the coils at a constant duty cycle, the effect of varying duty cycle cross-coupling estimated position can be kept constant. With the top coil used for self-sensing it is expected that cross-coupling in the y-axis will be at its minimum when the air gap is most positive in the y-axis, since the bottom coil's mutual component is at its minimum (figure 3.30) and the inductance of the top coil is at a maximum. The effect of the horizontal axis on the cross-coupling will always be the same due to the horizontal gains. From figure 3.29 the mutual effect on the top coil can be explained . When the rotor moves to the left the left coil gain increases and the right coil gain decreases and vice versa. Thus the total coupling effect on the top coil is always constant where material properties are neglected. For the DCM self-sensing technique the major cross-coupling component is due to the coil opposing the sensing coil.

In this chapter the basic model which is used as basis for the different self-sensing schemes was derived. The low and high frequency components of the voltage signal were analyzed using Fourier analysis. From the Fourier analysis it was determined that the low frequency component is linearly dependent on the duty cycle. The high frequency component is nonlinearly dependent on the duty cycle. The self-sensing method proposed by Schammass was discussed. Different demodulation methods were derived

with the aim to reduce phase shift effects. Two new self-sensing schemes were also derived. Possible practical limitations on the self-sensing schemes were discussed. The gradient method eliminates the effect of eddy currents, but the resolution was found to be poor due to the small sampling window and the gradient of the sensed current is sensitive for the slightest filtering. The DCM technique makes use of only the current component which eliminates the nonlinear duty cycle effect with the novel PWM switching method. Resolution was also identified as a limitation, but due to the implementation method the resolution can be increased. The two possible methods were discussed, but the costs increase on component count. Cross-coupling was investigated in terms of flux distribution and duty cycle variation. From the analysis the effect of duty cycle variation is reduced using the DCM self-sensing technique. In the next chapter the different self-sensing schemes will be simulated to evaluate the theory of the schemes.

Chapter 4

Self-sensing evaluation in simulation

In this chapter the transient AMB model is introduced. The different self-sensing schemes will be evaluated on this transient AMB model. The characteristics of the AMB model is given based on the practical system.

A nonlinear model identification method is introduced which includes compensation for nonlinear effects and position scaling. The nonlinear model identification method will be applied to all the self-sensing schemes.

The performance evaluation method is discussed in detail beforehand and then each self-sensing scheme is simulated and evaluated according to the performance evaluation method. The performance evaluation method constitutes a static and a dynamic evaluation method. In the case of the static evaluation method the linearity of the self-sensing scheme will be evaluated, which is an open loop evaluation. The dynamic evaluation method consists of two evaluation methods, namely the gain and phase relation and the robustness evaluation methods. The method to obtain the frequency and phase content of the position signals is also discussed.

Since the nonlinear model identification, scaling and performance evaluation methods apply to all the self-sensing schemes, each self-sensing scheme will be simulated and only the results of each self-sensing scheme will be discussed. After all the simulation results are obtained the different self-sensing schemes are compared.

The effect of cross-coupling is compared on the self-sensing scheme which makes use of digital FIR filter demodulation and the DCM self-sensing scheme. The effect of cross-coupling due to the current change rate and amplitude, which results in duty cycle variation, are investigated.

4.1 Transient AMB model

Self-sensing schemes in AMB systems are largely affected by the nonlinear effects due to the material properties. In simulation the accuracy of the self-sensing schemes compared to reality is dependent on

the AMB model's ability to simulate the nonlinear effects. A transient simulation model (TSM), which include hysteresis, magnetic material saturation, eddy currents and cross-coupling effects, will be used to simulate the practical AMB system [1], [37], [42], [49]. In the following subsections the different nonlinear effects in the TSM will be discussed in short.

4.1.1 Hysteresis and saturation model

Hysteresis and saturation forms an integral part of the nonlinear accuracy in an AMB model, since hysteresis and saturation are highly nonlinear effects. The saturation in the AMB simulation is modelled by two equations as shown in (4.1). The two asymptotes form the major loop. The smaller loops inside the major loop are modelled by the minor loops as given by (4.2). The envelope components of the hysteresis curve is determined by (4.1),

$$\begin{aligned} H_1(B) &= \frac{B}{\mu_0\mu_{r0}} + \frac{\sigma}{\mu_0}\left(1-\frac{1}{\mu_{r0}}\right)\log\left(1+\eta\cdot e^{\frac{B-B_s}{\sigma}}\right) + H_r \\ H_2(B) &= \frac{B}{\mu_0\mu_{r0}} - \frac{\sigma}{\mu_0}\left(1-\frac{1}{\mu_{r0}}\right)\log\left(1+\eta\cdot e^{\frac{-B-B_s}{\sigma}}\right) - H_r \end{aligned} \tag{4.1}$$

where B is the flux in the material, B_s the maximum flux level which determines the saturation level, and σ, H_r and η are material property constants. These constants are determined from practical measurements to ensure consistency between the practical and simulation AMB model.

Equation (4.2) is used to determine the minor loops inside the major loop region.

$$H(B) = \left\{ \begin{array}{ll} H_1(B) - [H_1(B_0) - H(B_0)]\cdot e^{-\beta|B-B_0|} & \text{if } B \geq 0 \\ H_2(B) - [H_2(B_0) - H(B_0)]\cdot e^{-\beta|B-B_0|} & \text{if } B < 0 \end{array} \right\} \tag{4.2}$$

The point of sign change in the derivative of the flux is used to determine the direction of the minor loop. The value B_0 is the flux at the point where the derivative's sign changes and β is a material constant determined from practical measurements. The lamination material used in the practical system is M400-50A silicon sheet steel. The model parameters are adjusted to fit the practical results [1]. The material constants are determined as shown in table 4.1.

Table 4.1: Hysteresis model constants

μ_r	4000
μ_{r0}	12000
η	0.015537
σ	0.19159
B_s	1.6025
β	5.4215
H_r	78.35

4.1.2 Eddy currents

Eddy currents have a large effect on the ripple component's form. At high switching frequencies, the eddy current component is more dominant than the ripple component due to the material reluctance. The simulation will include eddy currents to determine the effect of eddy currents on the self-sensing schemes.
Figure 4.1 shows one pole of a magnetic bearing with flux flowing through the magnetic material, due to the current (i) and the N turn coil. Eddy currents can be modelled by a single

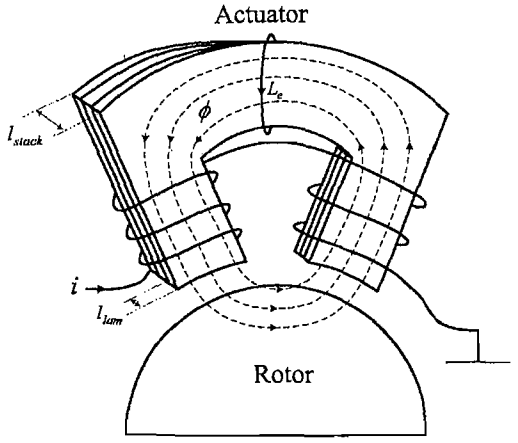

Figure 4.1: Eddy current magnetic model

turn coil with a resistance equal to the eddy current resistance [49]. The flux linked to the eddy current coil is determined by (4.3),

$$\phi_{ec} = \left(\frac{l_{lam} - \delta}{l_{stack}}\right)\phi \tag{4.3}$$

where l_{lam} is the lamination thickness, δ is the skin depth, l_{stack} is the total thickness of the laminations and ϕ is the flux generated by the current through the magnetic bearing's coil. The single turn eddy current coil's resistance is determined by (4.4),

$$r_{ec} = \frac{2\rho w}{l\delta} \tag{4.4}$$

where ρ is the resistivity of the magnetic material, w is the lamination width and l is the mean length of the magnetic path. By using this method the eddy currents are modelled as an abrupt change from one level to another when the bridge voltage is switched from positive to negative or vice versa. This eddy current model is adequate to model the effect of eddy currents on the self-sensing schemes.

4.1.3 Magnetic paths

From literature it was found that cross-coupling has a negative effect on self-sensing schemes. The effect due to cross-coupling on self-sensing schemes will be investigated, thus it will be

included in the simulation model.
Figure 4.2 shows the magnetic path model used to simulate the magnetic bearing as shown in 3.1, where ϕ_k is the flux through the material and k is the k^{th} path. Since the model includes all flux flow possibilities, one pole's flux can couple with another through the stator's back iron, thus including cross-coupling. The following equations are derived from the reluctance model

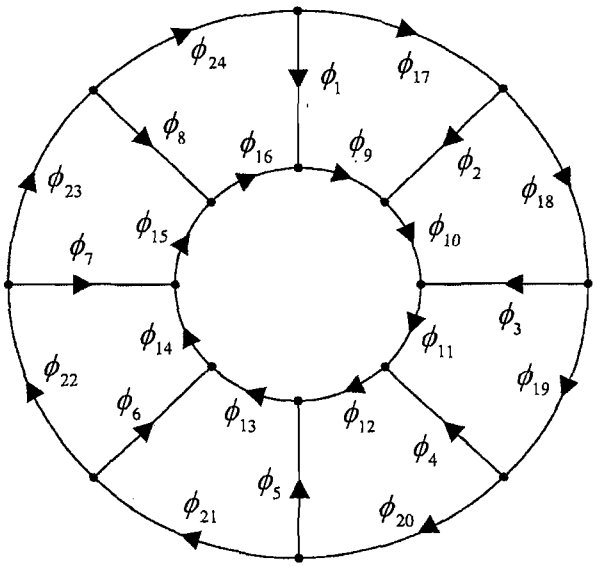

Figure 4.2: Actuator flux path model

where the derivative of the flux is determined and the current is calculated from the result of $\dot{\Phi}$.

$$\begin{aligned} \dot{\Phi} &= \mathbf{C}^{-1}\mathbf{L}\mathbf{H} + \mathbf{C}^{-1}\mathbf{G}\mathbf{H}_g + \mathbf{C}^{-1}\mathbf{N}\mathbf{V} \\ I &= \mathbf{I}_V\mathbf{V} + \mathbf{I}_\Phi\dot{\Phi} \end{aligned} \tag{4.5}$$

The model derivation and variables used to calculate the derivative of the flux and the current are discussed in detail by Ranft [1] and Noh *et al* [49]. Figure 4.3 shows the voltage and current waveforms, where a 20 kHz 100 volt switching voltage is applied to the magnetic bearing model as shown in the top figure. The bottom figure shows the current through the coil due to the switching voltage. The simulated current correlates well with the practical waveforms.

4.2 Magnetic bearing specifications

The physical magnetic bearing system which will be modelled using the TSM have specifications as shown in table 4.2.

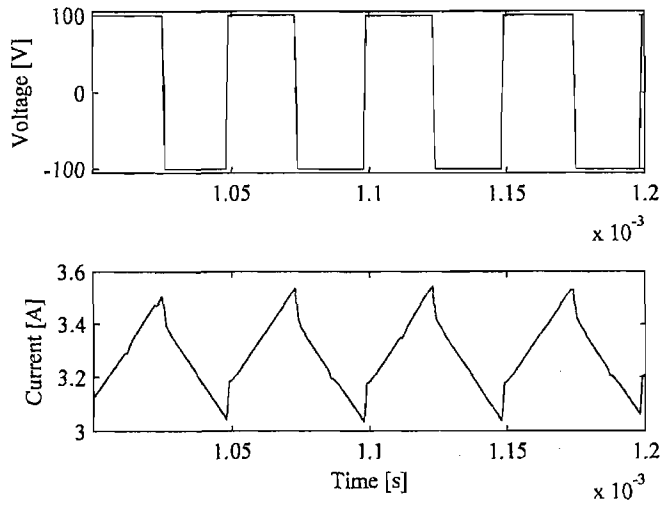

Figure 4.3: Switching waveforms

Table 4.2: Practical model specifications

Nominal inductance	5.2 mH
Coil resistance	0.2 Ω
Air gap	0.6 mm
Operating current	0 - 10 A
Bias current	3 A
Switching frequency	20 kHz
Switching voltage	50 V

4.3 Nonlinear model identification and scaling

In each self-sensing scheme the nonlinear effects of the AMB system must be identified. The identification method and scaling are mostly the same for all the self-sensing schemes, thus the identification method and scaling will be discussed in detail in the following subsection. The respective identified results will be shown in the relevant sub-sections.

4.3.1 Nonlinear model identification

In chapter 3, x_{ge} and x_m were used in the self-sensing model, but in the simulation and in the practical system the y-axis will be used for self-sensing, thus all modelling variables will be denoted with a y.

The nonlinear effects are identified for each method from the estimated flux through the ma-

terial and the uncompensated output y_{ge}. In the analog, FIR, band-pass sampling and FFT demodulation methods the demodulated current $\underline{I_d}$ is divided by the demodulated voltage $\underline{U_d}$, which are the uncompensated output denoted by y_{ge}. For the gradient and DCM methods the algorithm output will also be called the uncompensated output and denoted as y_{ge} for the ease of explanation.

The method to determine the nonlinearity due to saturation is discussed in detail in chapter 3 section 3.3.1. In simulation for each self-sensing scheme the rotor position will be forced to the center position (600 μm) and the current will be varied from 0 A to 10 A. By using the estimated flux, determined by (3.23), and y_{ge} the nonlinear compensation function y_m is identified using (3.18). The estimation function y_m and the uncompensated self-sensing scheme's output y_{ge} will be plotted on the same axis to visually inspect the efficiency of the estimation function.

If the estimation function is satisfactory, the constants obtained are implemented in the self-sensing compensation algorithm. The same nonlinearity measurement method as discussed above is repeated with the compensation function evaluated with the estimated flux. The estimation function output (y_m) is subtracted from the uncompensated output (y_{ge}) and the difference $y_{ge} - y_m$ is plotted. This error will be used as an evaluation of the nonlinear compensation function. Ideally, the output should be zero if the nonlinear function is an exact match of the nonlinearities. The nonlinear model identification must be determined for each self-sensing scheme, since the demodulation method affects the estimation function.

4.3.2 Scaling

If the nonlinear compensation is satisfactory the scaling constant k_x can be determined as shown in (3.19). After the model identification is completed the static and dynamic performance can be evaluated.

4.4 Self-sensing performance evaluation

In this section, performance evaluation methods which will be used to evaluate the performance of the self-sensing schemes, are introduced. Static and dynamic performance measurements will be used as evaluation methods. The static evaluation measures the linearity of the self-sensing scheme. The dynamic evaluation method makes use of gain and phase analysis and the robustness of the self-sensing system as described in the AMB's ISO 14839-3 standard manual to evaluate the dynamic performance.

4.4.1 Static evaluation

The linearity of the self-sensing schemes will be evaluated using the static evaluation method. It is important to note that this evaluation method is an open loop measurement method. The static evaluation method is as follows: the rotor position is linearly varied from the minimum

to the maximum position. The real and estimated position are recorded simultaneously. The real position points are plotted versus the estimated position points. The result should ideally be a linear line with a gradient of one. The static evaluation will indicate the deviations from the linear position when the self-sensing schemes reach the extreme positions.

4.4.2 Dynamic evaluation

The dynamic performance of the self-sensing schemes will be evaluated using gain and phase analysis and robustness measurement. The estimation position is used to close the loop for both performance measurement methods.

Gain and phase relation

The gain and phase analysis make use of the relationship between the real and the estimated frequency content of the position signals. In simulation the real position will be assumed to be the AMB model position output and the estimated position will be the output of the simulated self-sensing scheme. From these two outputs the gain and phase relation will be calculated.

The frequency content measurement method must determine the magnitude and phase properties of the real and estimated position signals. FFT measurements will be used to determine the frequency content. The AMB model is perturbed with a 10 µm peak to peak sinusoidal position reference at different frequencies. The perturbed signal frequency intervals will be of the FFT frequency spacing to optimize the FFT calculation accuracy. The FFT of the real and estimated position will be calculated and the phase and magnitude will be calculated at the specific frequency. From these results the gain and phase over various frequencies can be evaluated.

The frequency response ratio of the estimated to the real position is denoted as $G_x(\omega) = 20\log(\frac{X_e(\omega)}{X(\omega)})$, where $X_e(\omega)$ is the estimated position and $X(\omega)$ is the real position. The frequency response of $X_e(\omega)$ and $X(\omega)$ is obtained with the FFT method as described above. The phase of $X_e(\omega)$ and $X(\omega)$ are obtained using the FFT phase information. The phase of $X(\omega)$ is used as reference to $X_e(\omega)$. Ideally, $G_x(\omega)$ must have a gain of one and a phase of zero, but due to filters and the AMB system the gain and phase drift from the ideal case. Since the demodulation of some methods introduce a non-minimum phase component due to zeros outside the unity circle, the control performance of the AMB system is limited.

Robustness

The robustness of an AMB system with conventional sensors is determined by sensitivity measurements as described by the ISO 14839-3 standard [10]. The same method will be used to evaluate the robustness of the self-sensing schemes. In figure 4.4 a simplified AMB model is shown. By using the ratio between $E(\omega)$ and the reference position $X_{ref}(\omega)$ the sensitivity

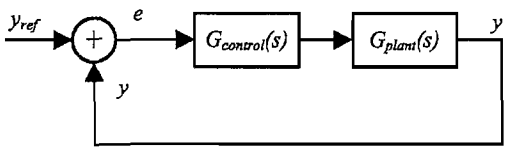

Figure 4.4: Simplified AMB system

function $G_S(\omega)$ can be obtained,

$$G_s(\omega) = \frac{E(\omega)}{X_{ref}(\omega)} \tag{4.6}$$

where $E(\omega)$ and $X_{ref}(\omega)$ are the frequency response of the error (e) and the position reference (x_{ref}) respectively. The FFT method is also used to obtain the frequency content. Table 4.3 shows the classification of AMB systems, where the sensitivity peak determines in which class the AMB system falls. Class A to D are defined as follows:

Class A: Is defined as a newly commissioned AMB system.
Class B: A system with the sensitivity functions normally acceptable for unrestricted long-term running.
Class C: A system with unsatisfactory sensitivity and is not suitable for long -term operation.
Class D: Sensitivity is classified as severe and can lead to damage to the machine.

4.5 Controllers

The position controller used to stabilize the position of the self-sensing system is shown in figure 4.5. A PID controller is used with some filter variations. The filters LPF_E and LPF_D are defined where LPF_E is in the path of all the PID inputs and LPF_D is only in the path of the derivative input. The purpose of the LPF_E is to reduce the total noise input to the PID controller, and the purpose of LPF_D is to reduce noise in the derivative path. In simulation the different self-sensing schemes make use of the filters LPF_E and LPF_D which have the same frequency response in all the schemes. The frequency response of the FIR LPF is shown in figure 4.6. From simulation the minimum order was determined to be 20. If the order is lower the phase shift is minimized, but the self-sensing schemes become unstable. The filter has a cutoff

Table 4.3: Sensitivity classification

Zone	Sensitivity peak [dB]
A	peak < 8
B	8 < peak < 12
C	12 < peak < 14
D	peak > 14

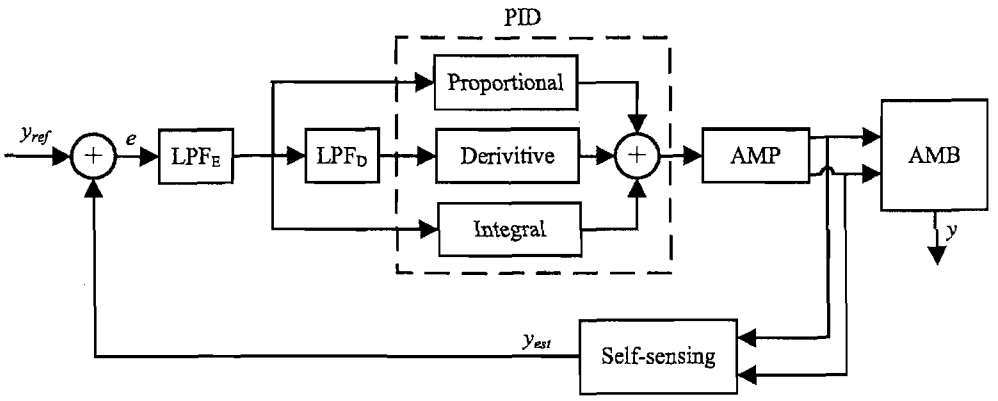

Figure 4.5: Controller block diagram

frequency of 300 Hz and a stop band of 700 Hz. Most of the self-sensing schemes use only

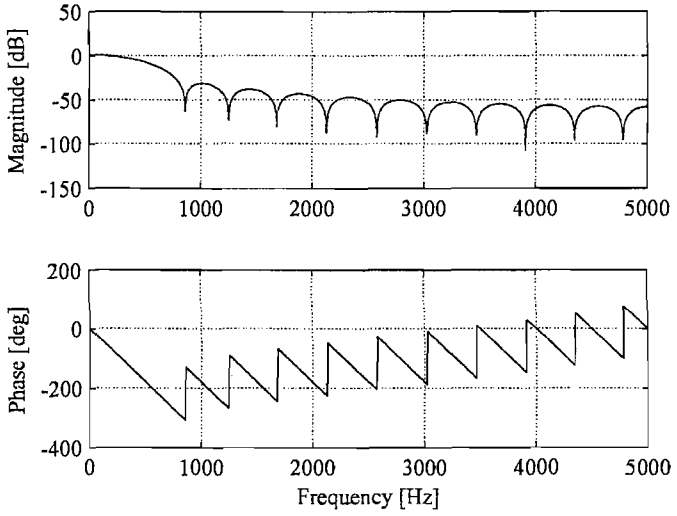

Figure 4.6: PID input filter response

LPF$_D$, but some use a combination of these two filters. In each self-sensing scheme's section the filter configuration used will be stated in the control section.

Figure 4.7 shows the AMB system with the current controller. The current signal is sensed using a LEM current sensor. The current signal is passed through an analog filter and then the signal is digitized. The PI controller is implemented on the controller. The proportional gain of the PI controller determines the power amplifier bandwidth. Ideally, the control loops must have a 50 μs cycle time to update the 20 kHz PWM signals. From practical implementation the control loops were not able to calculate the control output in 50 μs, thus the cycle time was adjusted to 100 μs. In simulation the control loops and the FIR filter will be evaluated at 10 kHz due to the practical implications.

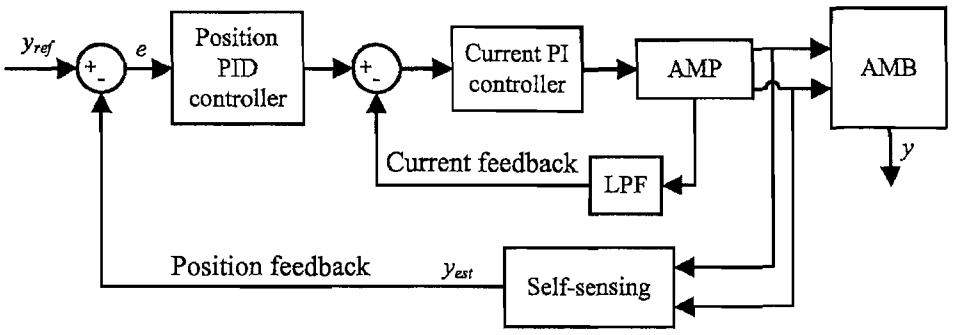

Figure 4.7: PI current controller

4.6 Self-sensing simulation and evaluation results

In the following subsections the different self-sensing schemes will be simulated and the simulation results will be given in terms of the static and dynamic evaluation methods. After all the simulations are completed a summary of the results are given in table form to compare performances.

4.6.1 Analog demodulation method

The analog demodulation method is directly based on Schammass's work, the difference from Schammass's work is that a different AMB system is used and the demodulation filters are not exactly the same. The self-sensing scheme is evaluated on a coupled AMB system which includes cross-coupling.

Demodulator filters

Figure 4.8 shows the block diagram of the analog demodulation method. The filters used in the analog demodulation method differs slightly from Schammass's work. In this method the BPF is implemented by an IIR BPF and the demodulator also make use of an IIR filter. The frequency response of the IIR filter is approximately the same response as in the physical analog system. The high frequency component is passed through a butterworth BPF to obtain the fundamental component. The BPF has a center frequency at the switching frequency and a bandwidth of 4 kHz. The demodulator consists of an ideal absolute function and a butterworth LPF with a cutoff frequency of 1 kHz. The BPF and LPF have an order of two. The sampling frequency of the filters is the same as the TSM (1 MHz), which is assumed to be real time. Figure 4.9 shows the gain and phase response of the BPF. Since the BPF has a low-pass effect on the position modulated current ripple it is investigated [5]. The BPF low-pass effect can be modelled by a first order LPF with a cutoff frequency at half the bandwidth of the BPF which is 2 kHz. The frequency response of the LPF is shown in figure 4.10. From the phase plot it is clear that the BPF introduces a phase shift onto the demodulated current, thus affecting the self-sensing bandwidth.

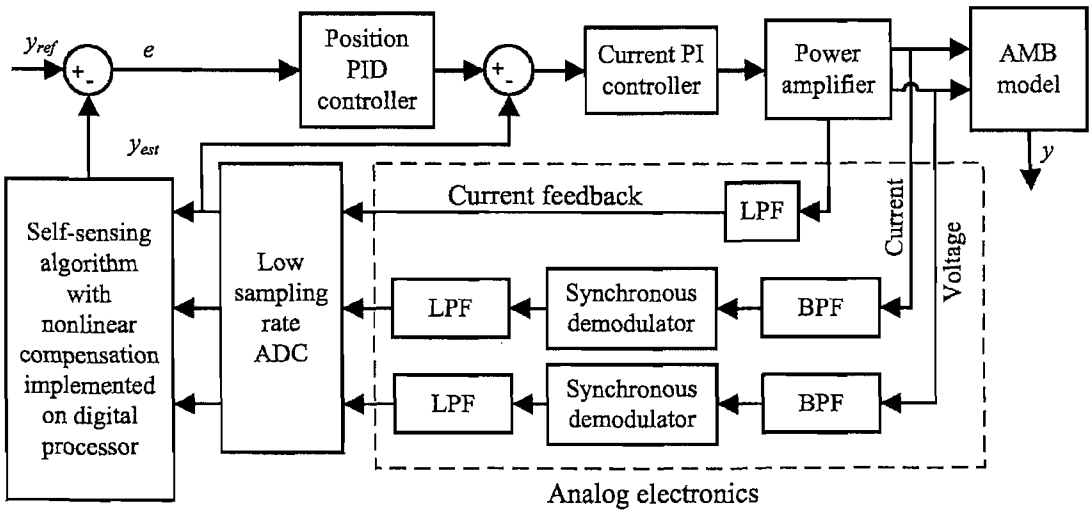

Figure 4.8: Block diagram of the analog demodulation self-sensing scheme

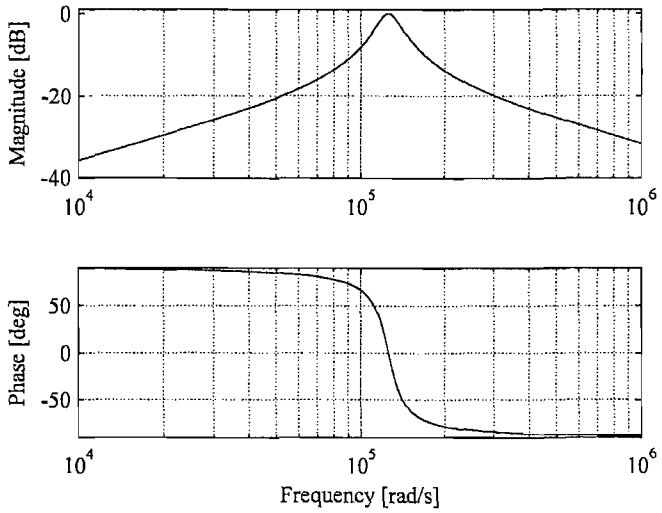

Figure 4.9: Analog BPF frequency response

The BPF current component is passed through the demodulator. For this analysis it is assumed that the analog absolute calculation of the demodulator reacts the same as an ideal absolute function.

The rectified signal is passed through the LPF which shifts the high frequency component to low frequencies. This LPF mostly determines the bandwidth of the self-sensing scheme, since it has the lowest cutoff frequency of all the components in the analog self-sensing scheme. The frequency response of the LPF filter is shown in figure 4.11. From the phase response it is clear that it has a large effect on the estimated position.

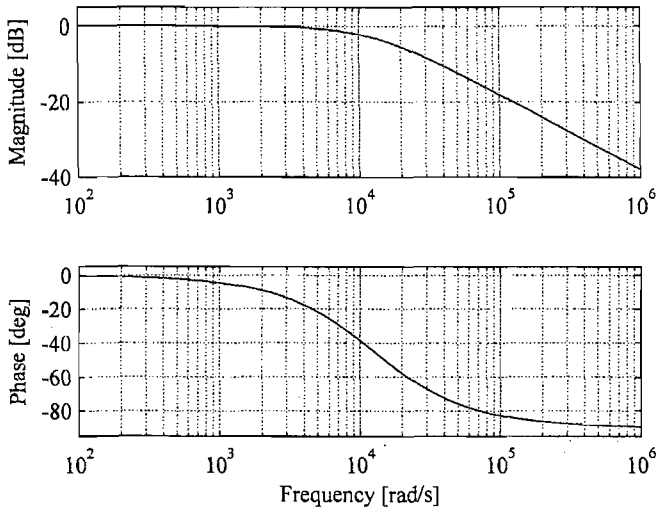

Figure 4.10: LPF effect due to BPF

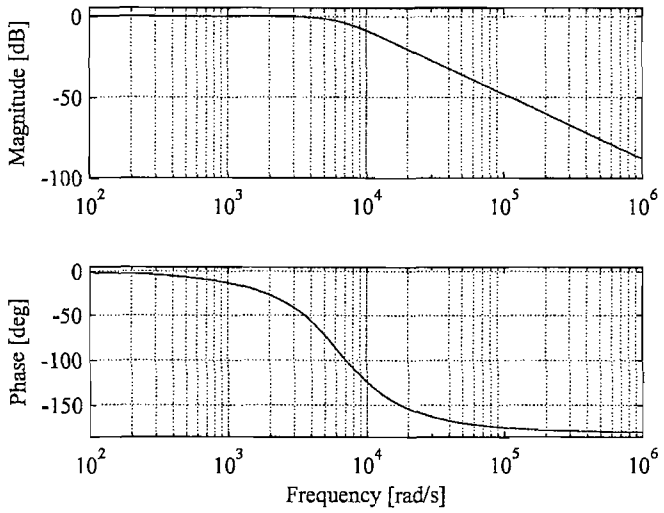

Figure 4.11: Demodulator LPF

Demodulation effects

The analog demodulation method gain and phase effects were discussed in section 3.4.1 where it was found that the gain and phase effect is due to the low-pass effect of the BPF and the LPF used in the demodulator to shift the high frequencies to low frequencies. $G_d(z)$ in the analog demodulation method will be modelled with IIR filters with the same properties as the combination of the two analog filters. The frequency response of $G_d(z)$ for the analog case is shown in figure 4.12. From figure 4.12 it is clear that the analog demodulation method affects

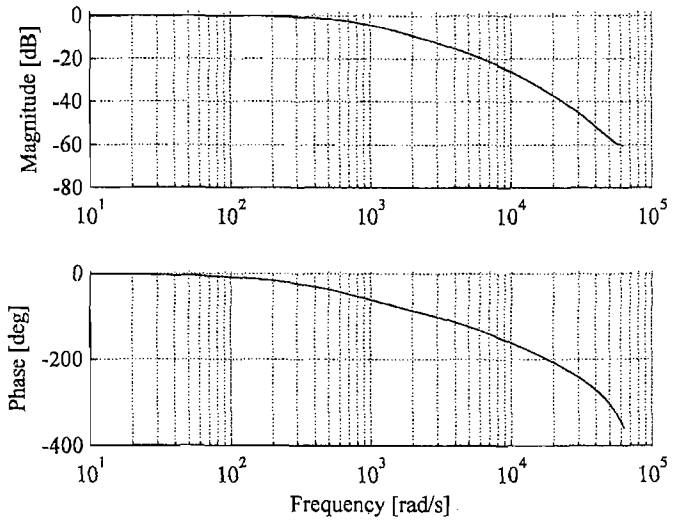

Figure 4.12: $G_d(z)$ frequency response: Analog demodulation method

the phase of the estimated position substantially.

Nonlinear model identification

The analog demodulation method as discussed previously is applied on the current and voltage signal of the TSM. The demodulated current to voltage ratio y_{ge} and the estimated flux are determined. Figure 4.13 shows the nonlinear effects mostly due to saturation. The estimation function y_m obtained from (3.18) is also plotted; a fourth order fit is used for the estimation function. The nonlinear estimator constants are evaluated in simulation by performing the same procedure as above, but by plotting $y_{ge} - y_m$, where y_m is calculated using the estimated flux. The ideal output should be zero if the nonlinear function is an exact estimation of the nonlinearities. The result is plotted in figure 4.14. The scaling constant k_x is determined as -1.5 for the analog demodulation method.

Static evaluation

The linearity of the analog self-sensing scheme can be evaluated using the real and estimated position. The method discussed in section 4.4 will be used. Figure 4.15 shows the static evaluation of the analog self-sensing scheme. The estimated position follows the real position relatively well, but at the extreme positions the estimated position deviates from the desired position. This is expected, since the nonlinear model is determined at the center position. Note that the static evaluation is an open loop evaluation method, since the rotor is forced to a position and the response of the real and estimated position signals are compared in open loop.

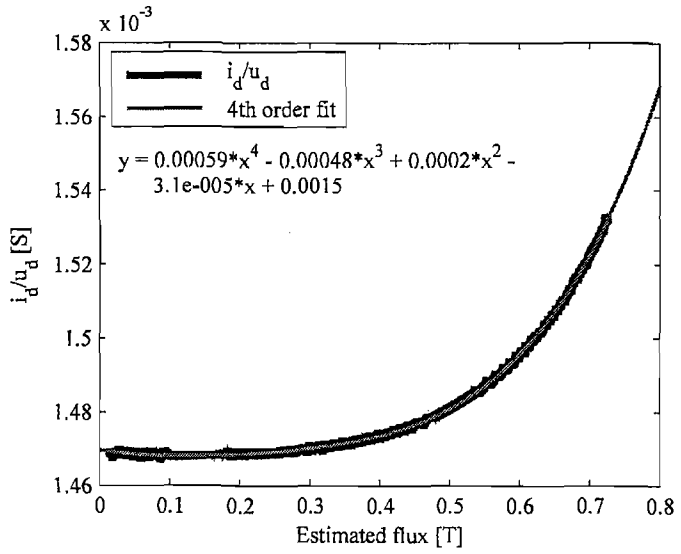

Figure 4.13: Nonlinear effects on self-sensing scheme

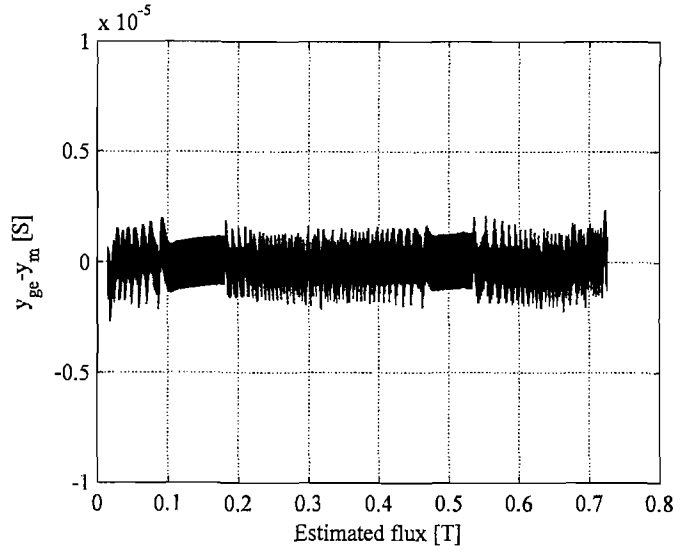

Figure 4.14: Nonlinear compensated output

Controller parameters

Since the coupled AMB system was used to evaluate the analog self-sensing scheme the control constants had to be altered to obtain stability.

If the derivative constant of the position controller is too large a high frequency component is present. This high frequency component is also dependent on the proportional gain of the current loop. By reducing the bandwidth of the current loop and by reducing the damping,

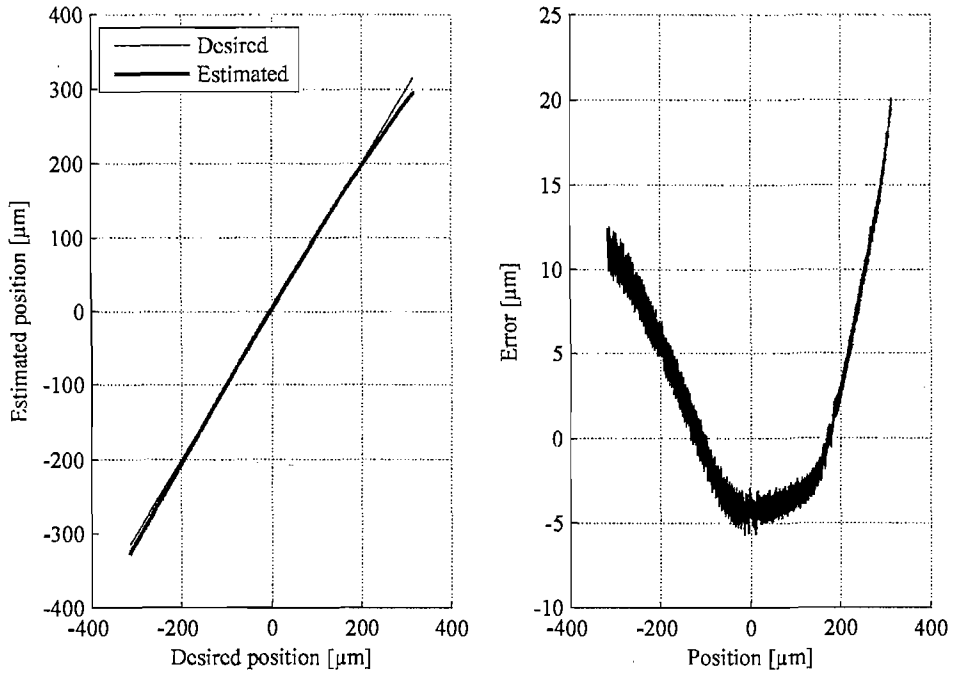

Figure 4.15: Static evaluation: Analog method

the high frequency component is eliminated. This may be due to estimated position dependency on the current ripple. If there is a high frequency component present the derivative will reinforce the high frequency component. By reducing the derivative the high frequency amplitudes may be reduced or eliminated, but the damping may become too low. By reducing the power amplifier bandwidth the high frequency component can be reduced, but the overall AMB bandwidth will be lower. Optimal performance has been obtained by reducing the amplifier bandwidth and the derivative constant with adequate performance. The power amplifier bandwidth is set to 1300 Hz.

A low frequency component is present when the proportional gain is too high. The low frequency oscillation may be due nonlinearities. If the proportional gain of the position controller is large, the system comes close to the characteristics of a marginally stable system or an unstable system. By reducing the proportional gain the system becomes more stable, thus the phase margin may be increased. The control parameters of the analog demodulation method are shown in table 4.4. These control parameters are the maximum values obtainable with stable suspension with only LPF_D in the PID's derivative path.

Dynamic evaluation

The position control loop is closed with the estimated position. Nonlinear material compensation is included in this evaluation. The gain and phase response of the analog simulation

Table 4.4: Control constants: Analog scheme

Constant	Value
K_p	10000
K_d	25
$K_{p_{AMP}}$	0.35

were obtained by exciting the system with a 10 μm peak to peak sinusoidal position reference from 16 to 1000 Hz. The gain and phase response obtained by the FFT method is shown in figure 4.16. The gain starts to deviate from 0 dB at approximately 150 Hz and reaches 20 dB at 400 Hz. The phase starts to deviate from 0 degrees at 100 Hz and peaks at approximately 400 Hz. The robustness of the system is obtained using the frequency response of the position

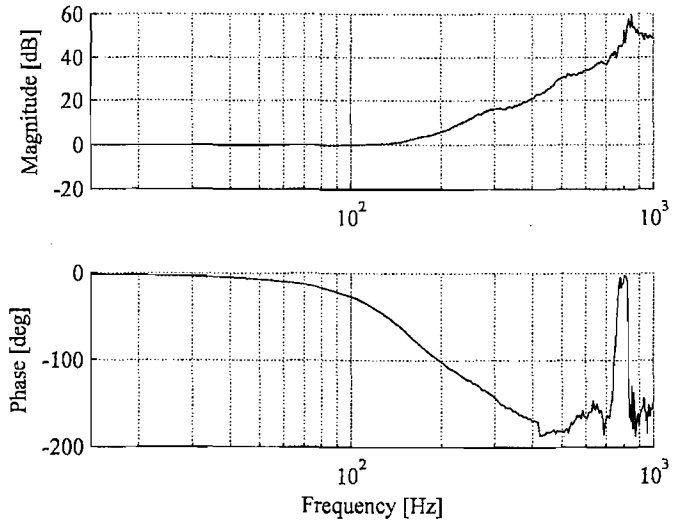

Figure 4.16: Gain and phase response: Analog demodulation method

reference and error signals with the same reference used as in the gain and phase analysis. The robustness of the self-sensing system is shown in figure 4.17. The peak sensitivity is at 13.3 dB, which classifies the self-sensing AMB system as type C. The first rigid body mode is found to be around 100 Hz.

4.6.2 Digital demodulation method

In the digital demodulation method a combination of analog and digital filters are used. In simulation an IIR filter will be used to obtain the fundamental component and a FIR filter will be used for the demodulator. The fundamental component is obtained by a BPF with the same characteristics as in the analog demodulation method. The demodulator is implemented by an absolute function and the LPF, which is implemented with a FIR filter with a cutoff frequency of 600 Hz. The FIR LPF filter is a 500th

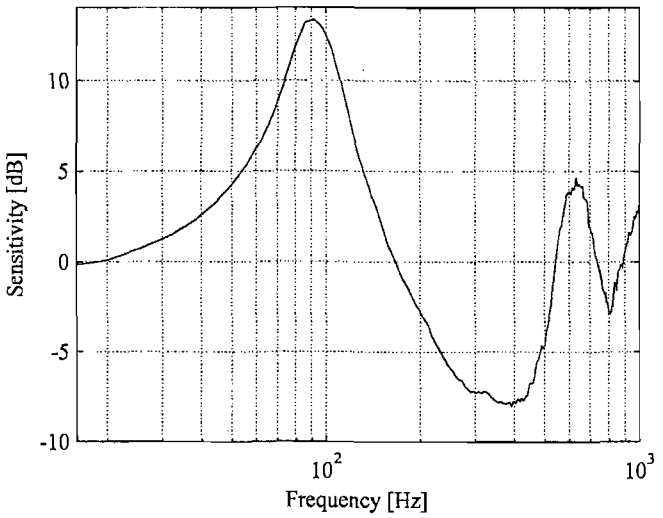

Figure 4.17: Sensitivity plot: Analog method

order filter with a pass band of 300 Hz and a stop band of 3500 Hz. The FIR LPF has a 1 MHz sampling rate which correlates with the maximum sample rate in the hardware implementation.

Demodulator

Figure 4.18 shows the block diagram of the digital demodulation self-sensing scheme. The

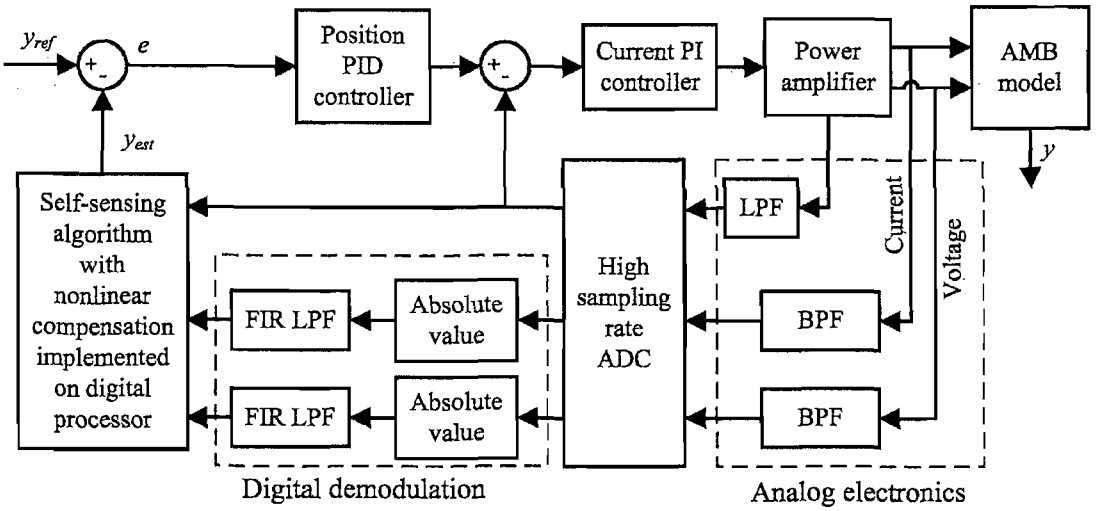

Figure 4.18: Block diagram of the digital demodulation self-sensing scheme

same analog BPF is used as in the analog demodulator, and the same low-pass effect and phase

shift exist due to the BPF as stated in the analog demodulation case.

The band-pass filtered current and voltage components are sampled at 1 MHz and passed through the absolute function and then passed through the FIR LPF to shift the high frequencies to low frequencies. This LPF also determines the bandwidth of the self-sensing scheme. The frequency response of the FIR LPF is shown in figure 4.19. From the frequency response the

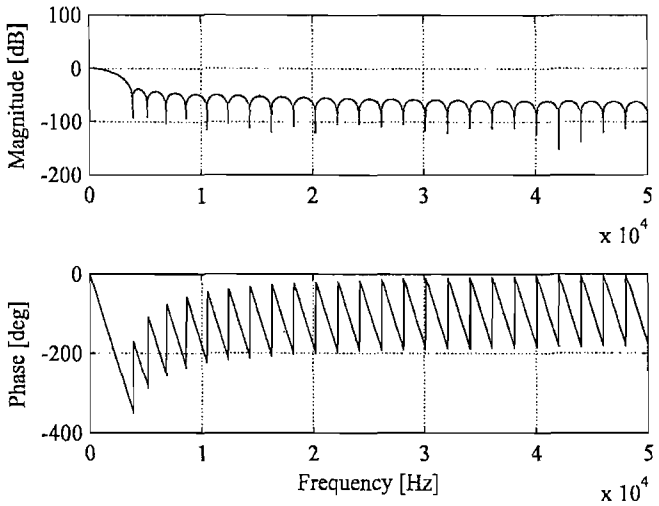

Figure 4.19: Frequency response of FIR LPF

filter has a large effect on the overall bandwidth of the self-sensing scheme.

Demodulation effects

In the digital demodulation method the analog LPF is replaced by a FIR LPF as discussed in the previous section. $G_d(z)$ in the digital demodulation method will be modelled with a combination of a FIR LPF and an IIR BPF with the same properties as discussed in the previous section. The frequency response of $G_d(z)$ for the digital demodulation method is shown in figure 4.20. From figure 4.20 it is clear that the digital demodulation method still affects the phase of the estimated position. From the figure it is also clear that the combination of an IIR and FIR filter results in a nonlinear phase effect. The FIR filter's phase is more dominant.

Nonlinear model identification

Figure 4.21 shows the nonlinear effects on y_{ge} due to the AMB system and the estimation function is also plotted. Again, a fourth order fit is used for the estimation function.
Figure 4.22 shows $y_{ge} - y_m$ with y_m evaluated with the estimated flux. The output is close to

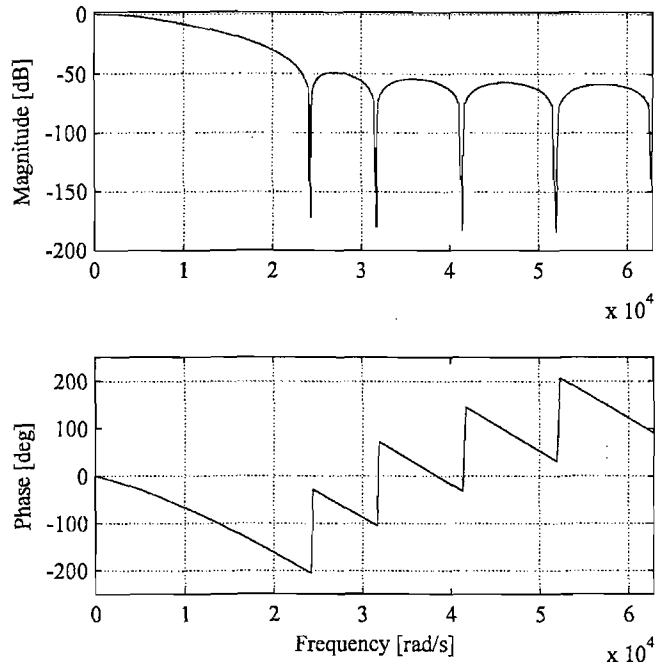

Figure 4.20: $G_d(z)$ frequency response: Digital demodulation method

zero, thus the compensation function is adequate. The scaling constant k_x is calculated as -1.55 for the digital FIR demodulation method.

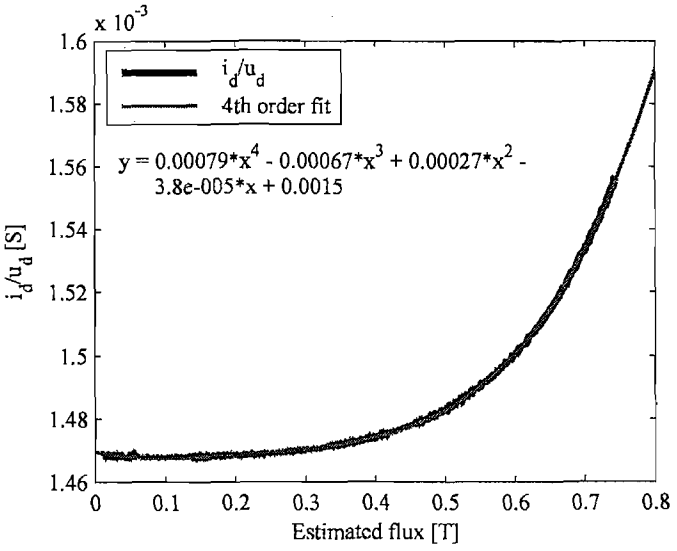

Figure 4.21: Nonlinear effects on self-sensing scheme

Static evaluation

Figure 4.23 shows the static evaluation of the digital self-sensing scheme. From these results it is clear that the system performs well over a wide range, but deviates from the desired position at the maximum positions.

Controller parameters

The coupled AMB system was again used to evaluate the digital filtering self-sensing scheme and the control constants had to be altered to obtain stability. The control parameters are summarised in table 4.5 with the derivative constant K_d of the position controller decreased to 20 where in the analog case it was 25. In table 4.5 the maximum control values obtainable with stable suspension with LPF_D in the PID's derivative path are shown.

Dynamic evaluation

The gain and phase of the FIR filter scheme were obtained by exciting the system with a 10 μm sinusoidal position reference from 16 Hz to 1 kHz. The frequency and phase response obtained by the FFT method are shown in figure 4.24 . The gain starts to deviate from 0 dB at approximately 150 Hz and reaches 20 dB at 400 Hz. The phase starts to deviate from 0 degrees at approximately 100 Hz and peaks at 400 Hz. These results correlate well with the analog method. Figure 4.25 shows the robustness of the FIR demodulation method. The peak value is at 13.7 dB, which is very close to the analog demodulation method. The frequency of the first rigid mode has changed slightly.

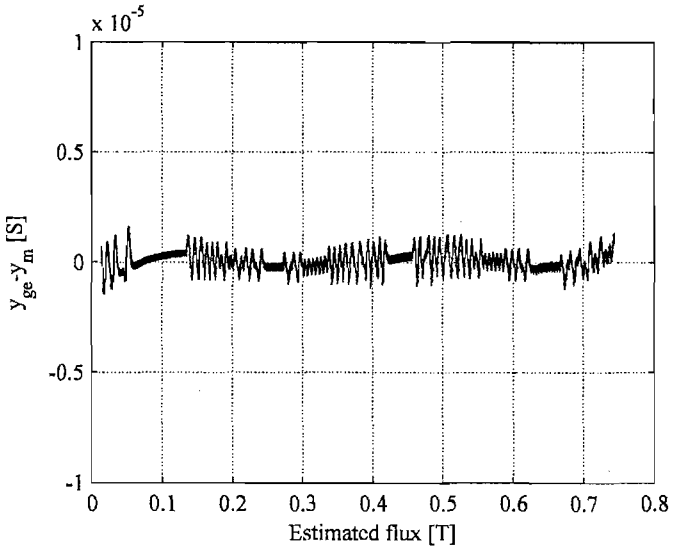

Figure 4.22: Nonlinear compensated output

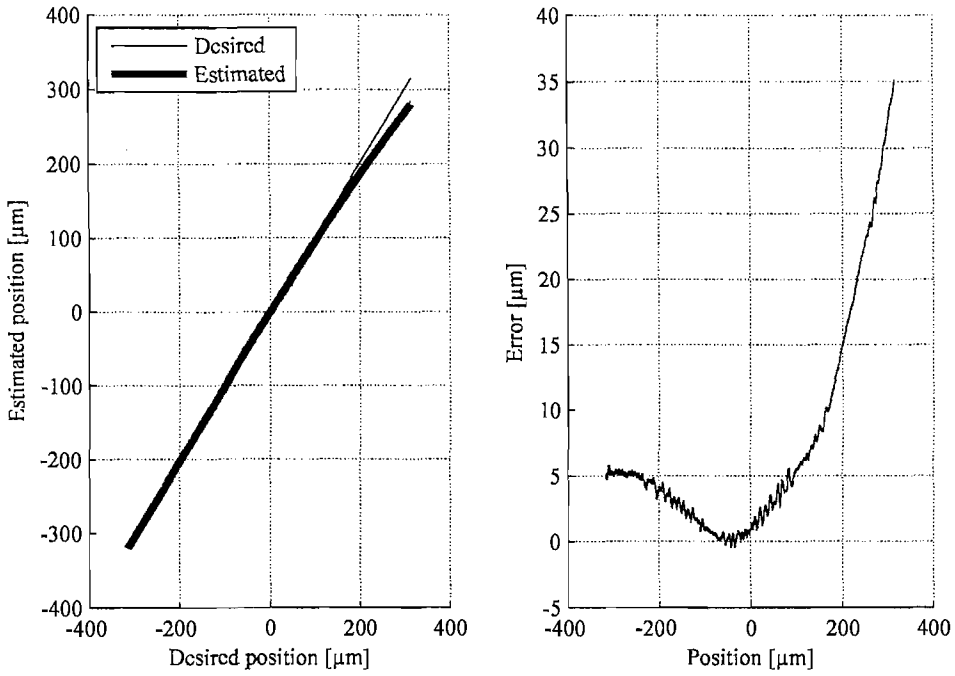

Figure 4.23: Static evaluation: Digital method

Table 4.5: Control constants: Digital method

Constant	Value
K_p	10000
K_d	20
$K_{p_{AMP}}$	0.35

4.6.3 Band-pass sampling demodulation method

In the band-pass sampling demodulation method the demodulator and LPF are eliminated, and the same analog BPF as in the previous demodulation methods is used. This method was proposed by Schammass to reduce cost and component count.

Demodulator

Figure 4.26 shows the block diagram of the band-pass sampling demodulation self-sensing scheme. The method proposed by Schammass samples at the peak values of the band-pass filtered signal, but due to the BPF dynamics the peak value is not exactly synchronized with the PWM signal. Another method was devised to determine the peak values. The signals

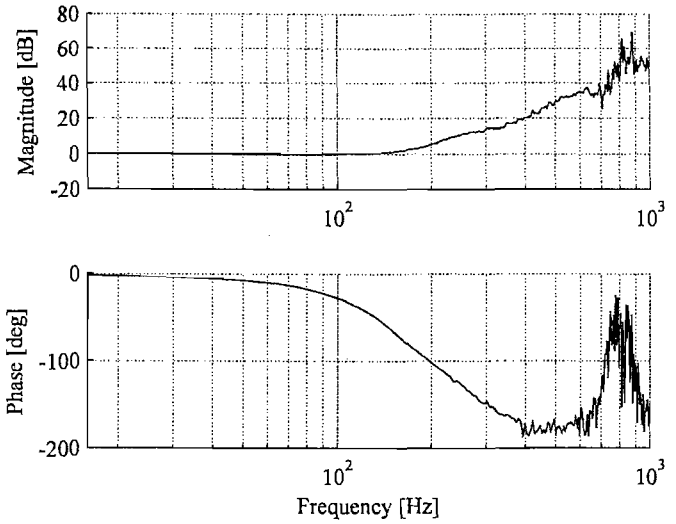

Figure 4.24: Gain and phase response: Digital method

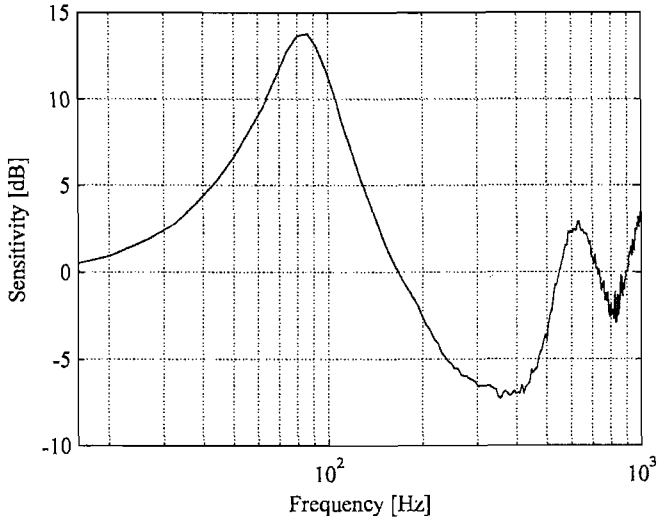

Figure 4.25: Sensitivity plot: Digital method

are sampled at a high sampling rate and the peak values are determined by the largest and lowest saved values in one switching period. This defies the point to eliminate the LPF since the sampling frequency has to be increased which increases cost due to the high speed ADC. The band-pass sampling method is evaluated to determine the feasibility of the method had synchronized sampling not been a problem.

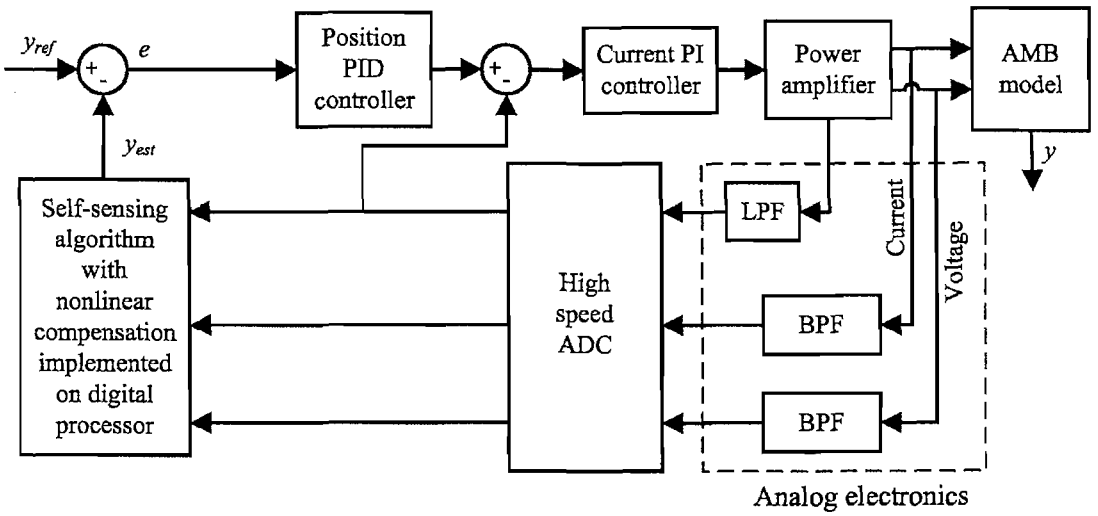

Figure 4.26: Block diagram of the band-pass sampling demodulation self-sensing scheme

Demodulation effects

In the band-pass sampling method the demodulation consists of the analog BPF and the peak sampling method. The sampling frequency of the peaks in the band-pass sampling method is twice the switching frequency. By evaluating $G_{d0}(j\omega)$ in (3.33) the effect of the band-pass sampling method is obtained as shown in figure 4.27. The frequency response is evaluated up to 500 Hz which is the bandwidth of the AMB. From these results it is clear that the band-pass sampling technique has little effect on the gain and phase, thus it will be neglected from $G_d(z)$. $G_d(z)$ will only include the effect of the analog BPF. The BPF in the digital demodulation method will be modelled by the same IIR BPF as discussed in the previous section. The frequency response of $G_d(z)$ for the band-pass sampling demodulation method is shown in figure 4.28. From figure 4.28 it is clear that the band-pass sampling demodulation method affects the phase of the estimated position less than the previous methods due to the elimination of the LPF in the demodulation path.

Nonlinear model identification

The demodulation method is applied to the band-pass filtered current and voltage signals. Figure 4.29 shows the nonlinear effects on y_{ge} and the fourth order estimation function y_m. Figure 4.30 shows $y_{ge} - y_m$, where the output is much more noisy than expected. Since there is no filtering at the output of y_{ge} the noise on the signal can be explained. The output is relatively close to zero, thus the estimation is assumed adequate without the amount of noise. The scaling constant k_x is determined as -1.58 for the band-pass sampling demodulation method.

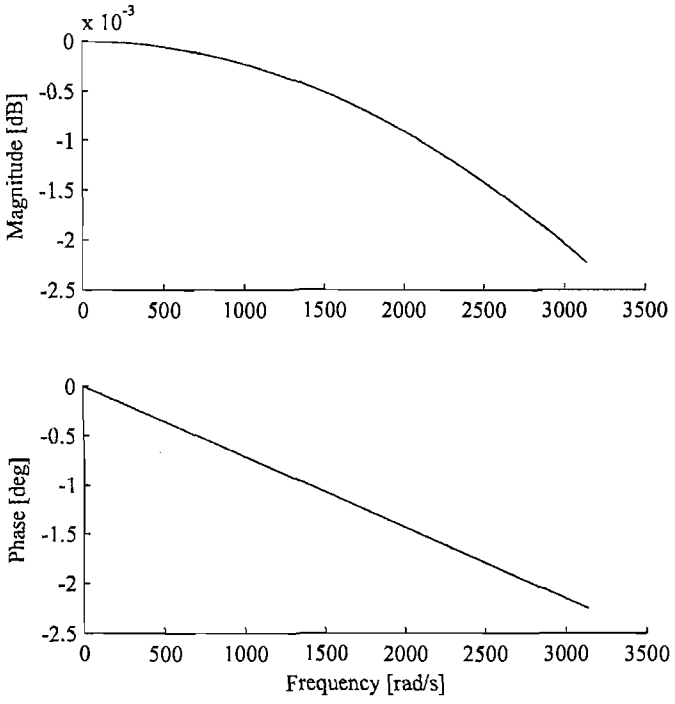

Figure 4.27: Frequency response of band-pass sampling demodulation method with out BPF

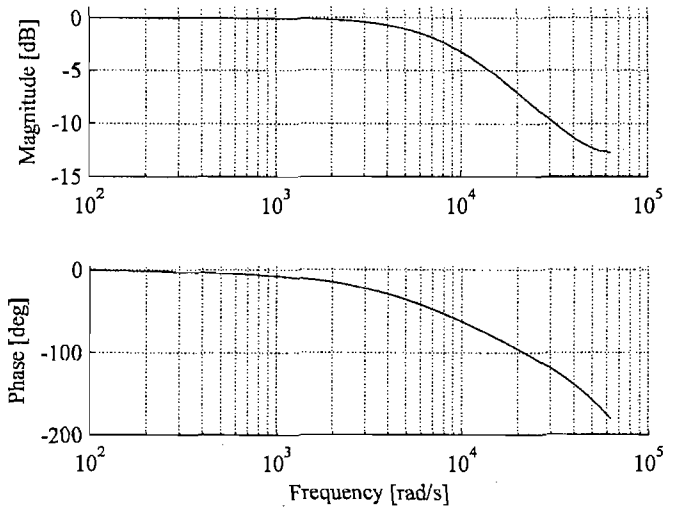

Figure 4.28: $G_d(z)$ frequency response: Band-pass sampling demodulation method

Static evaluation

Figure 4.31 shows the static evaluation of the band-pass sampling demodulation method. The

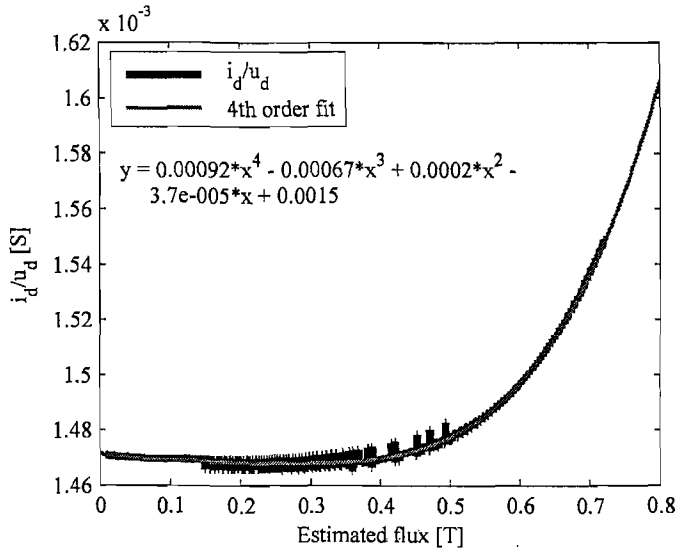

Figure 4.29: Nonlinear effects on self-sensing scheme

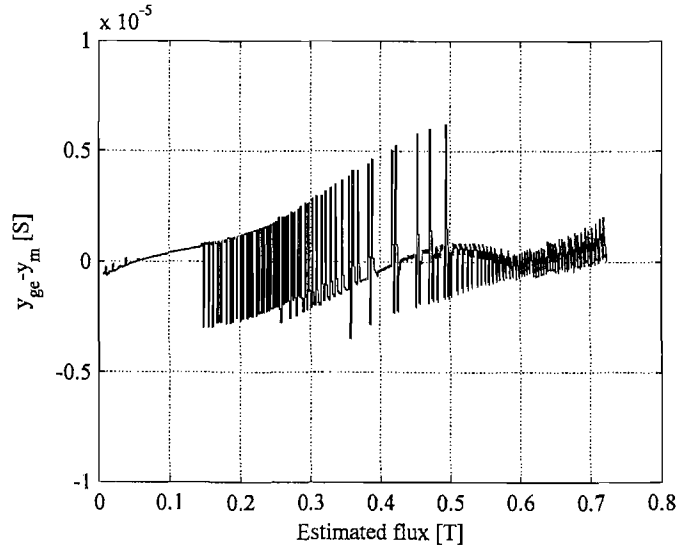

Figure 4.30: Nonlinear compensated output

band-pass sampling technique follows the desired position, but the estimated position is only linear over a very small range at the center position. From inspection of figure 4.31 the noise level is higher than the other methods. The noise is about 5 μm at the center position.

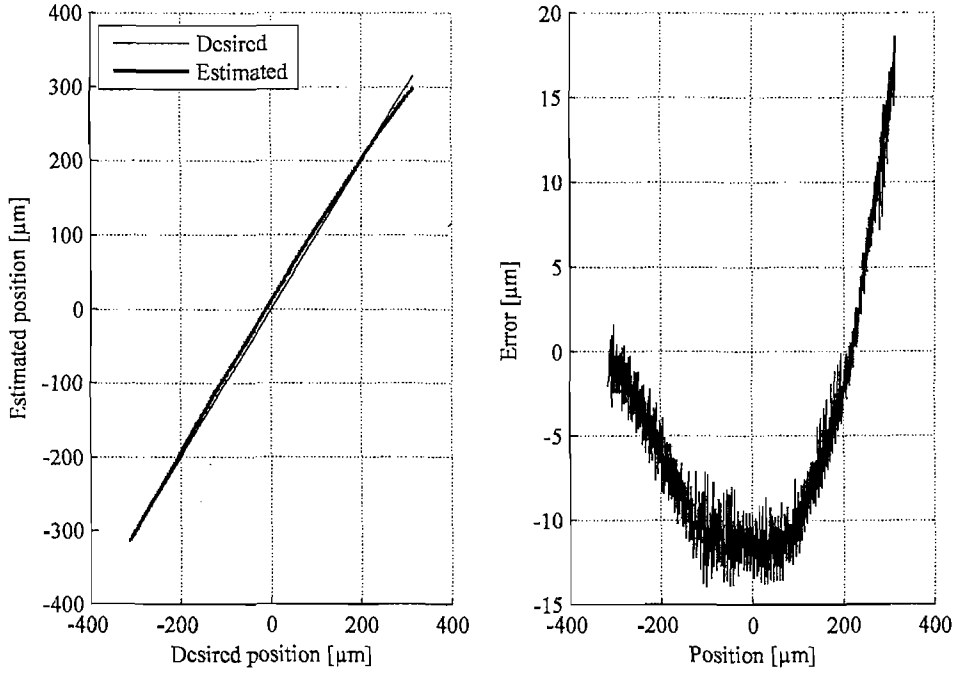

Figure 4.31: Static evaluation

Controller parameters

The control parameters of the band-pass sampling technique had to be altered and the power amplifier bandwidth had to be reduced to 760 Hz to obtain stability. The control parameters are summarised in table 4.6. These control parameters are the maximum values obtainable with stable suspension with LPF_D and LPF_E in the PID's input paths.

Dynamic evaluation

The gain and phase plot of the band-pass sampling scheme is shown in figure 4.32. The gain starts to deviate from 0 dB at approximately 300 Hz and reaches 20 dB at 450 Hz. The phase starts to deviate from 0 degrees at approximately 100 Hz and peaks at 400 Hz. The robustness of the band-pass sampling self-sensing scheme is shown in figure 4.33. The peak value is at 11.6

Table 4.6: Control constants: Band-pass sampling method

Constant	Value
K_p	10000
K_d	22
$K_{p_{AMP}}$	0.2

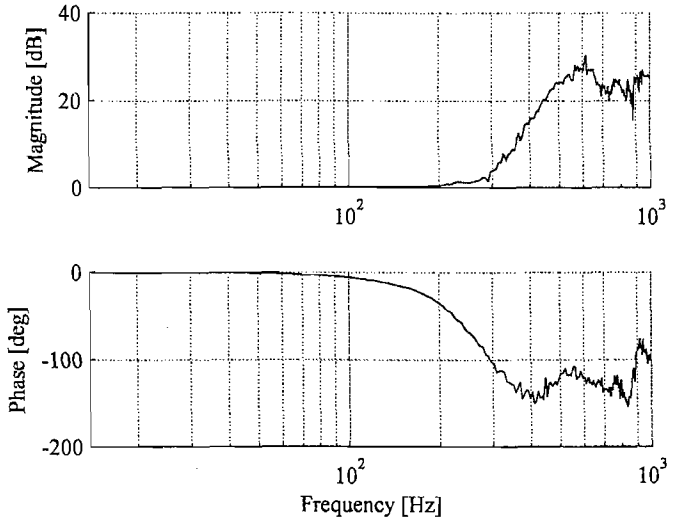

Figure 4.32: Gain and phase response: Band-pass sampling method

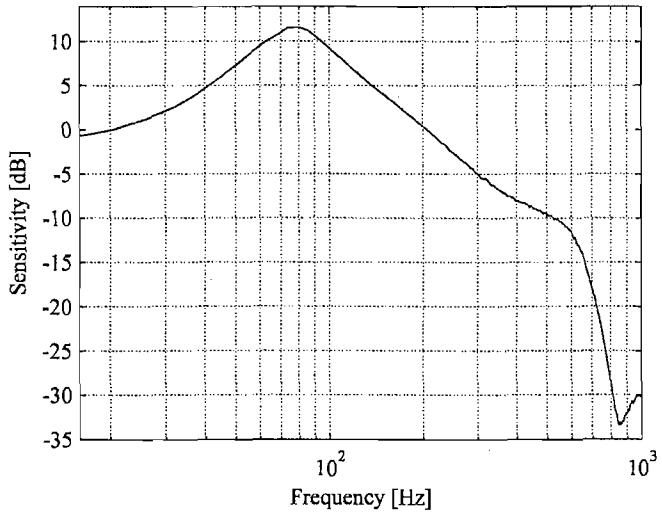

Figure 4.33: Sensitivity plot: Band-pass sampling method

dB. It was not expected that the sensitivity peak would be lower than the previous self-sensing schemes since LPF_D and LPF_E introduced large phase shifts. The reduced sensitivity might be due to the filters and the low mechanical bandwidth of the AMB.

4.6.4 Fast Fourier Transform (FFT) demodulation method

In the FFT demodulation method two cases will be evaluated: 1) where the signals are passed through a BPF and 2) where the signals are detrended and the FFT calculated from these outputs. The FFT demodulation method replaces the LPF in both cases, but in the second case the BPF is also eliminated. The motivation for the FFT demodulation method is noise immunity and phase reduction. The effect of the BPF in the demodulation path will be evaluated, since comparison of the band-pass sampling and detrending FFT method caters for this evaluation.

Demodulator

In the FFT demodulation method an analog BPF is used to obtain the fundamental component and to remove the control current. Alternatively a detrending function is used to remove the control current without any filtering. In this method an FFT function used as the demodulator. Figure 4.26 shows also the FFT demodulation method which make use of BPFs. In this case the an IIR BPF is used to obtain the fundamental component and a 256 point FFT for the demodulator. The same BPF will be used as in the previous methods. Figure 4.34 shows the block diagram of the FFT demodulation method which makes use of digital detrending. In the de-

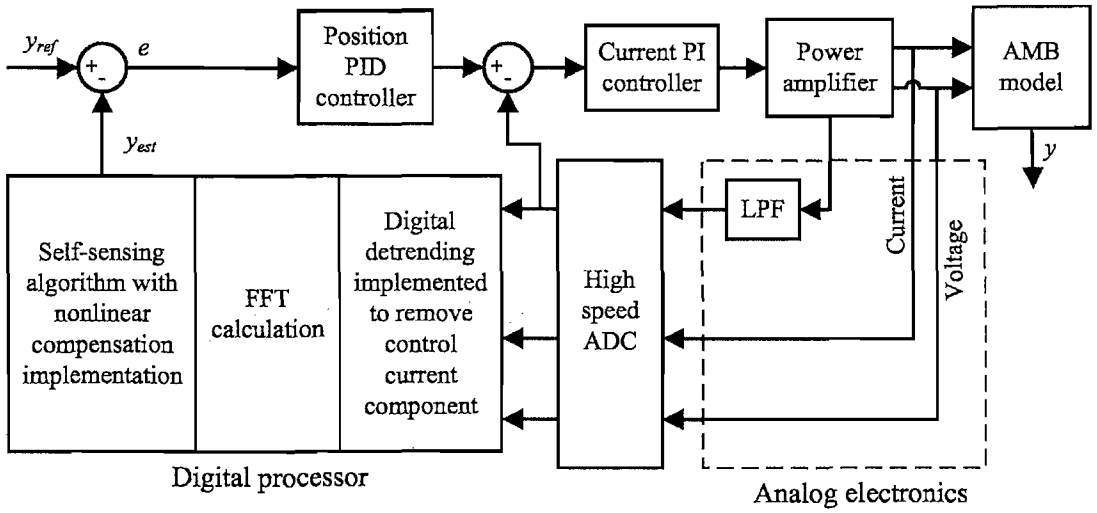

Figure 4.34: Block diagram of the FFT demodulation self-sensing scheme which makes use of digital detrending

trending method's case the current signal is passed through a detrending function which is part of the digital algorithm and thus the BPF is eliminated. The detrend function in MATLAB® will be used for the simulation implementation with all the samples used to calculate the trend.

The output of the BPF or detrend function is passed through the 256 point FFT function. The FFT function is evaluated at 1 MS/s, with a frequency spacing of 3.9063 kHz between each FFT

frequency point. The closest FFT frequency calculation to the 20 kHz switching frequency is 19.531 kHz, which is the 6^{th} calculated point in the FFT.

Three PWM cycles of the filtered or detrended current and voltage signals are used as data inputs for the FFT calculation. The three cycles consist of two delayed cycles and the present cycle. The motivation for using more than one cycle is that an averaging effect is obtained which should increase stability.

Demodulator effects

In the FFT demodulation method two implementations are possible as discussed above. Both methods make use of an FFT function, but one uses detrending where the other uses an analog BPF. In the detrending case the fundamental frequency content is mostly changed by the FFT function, but in the case where the BPF is used the frequency content is dependent on the low-pass effect of the BPF and the FFT function.

The effect of the FFT is investigated first. From Ranft [1] it was determined that the frequency response of an FFT function can be modelled by using a zero-order hold function. Equation (4.7) shows the modelling transfer function F(s) of the FFT,

$$F(s) = \frac{1 - e^{-T_1 s}}{T_1 s} \cdot \frac{1 - e^{-T_2 s}}{T_2 s} \tag{4.7}$$

where T_1 is the width of the window and T_2 is the period intervals at which the FFT function is evaluated. In the simulation three switching periods were used, which consists of the present period and two delayed periods. The FFT is evaluated at the end of the switching period.

Figure 4.35 shows the frequency response of $F(s)$. Using this result the response $G_d(z)$ can be determined for both FFT demodulation methods. Figure 4.36 shows the frequency response of $G_d(z)$ for the FFT demodulation method which makes use of the analog BPF. An IIR LPF was used to model the combination of the analog BPF and FFT response. The filter was designed to match the phase response of the combined responses up to the AMB's bandwidth. In the case where the FFT with the detrending demodulation method is applied the FFT function has the most effect on the frequency content. Since $F(s)$ resembles a FIR system a FIR LPF was used to model $G_d(z)$. Figure 4.37 shows the frequency response of $G_d(z)$. From figure 4.28 it is clear that the FFT method which makes use of the BPF has a large effect on the frequency response. The phase shift in the case where detrending is applied, is approximately 20 degrees less than the case where the BPF is used.

Nonlinear model identification

The current-to-voltage ratio y_{ge} is obtained by dividing the 19.531 kHz output of the current FFT calculation with the 19.531 kHz voltage FFT calculation. Figure 4.38 and 4.39 show the non-linear effects on y_{ge} and the fourth order estimation function y_m where the BPF and detrending function were used respectively in the demodulation path. Figure 4.40 and 4.41 show the compensated output respectively. The scaling constant k_x is determined as -1.5 for both cases.

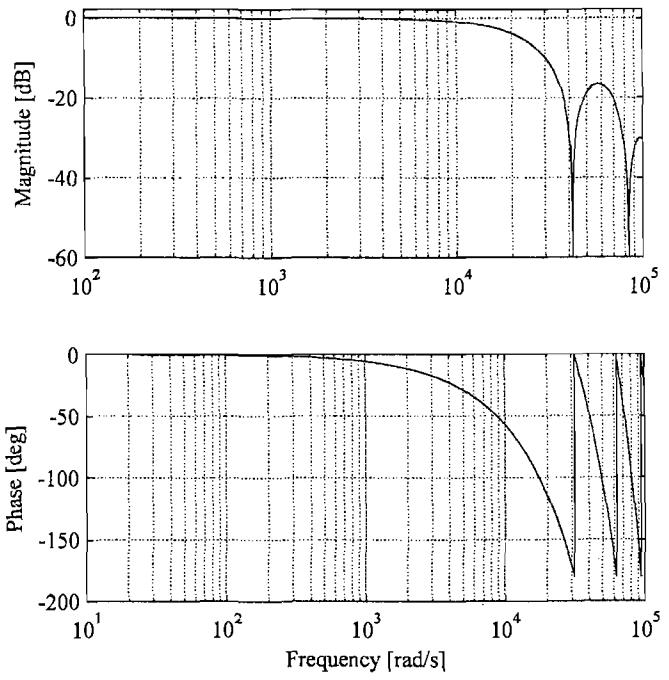

Figure 4.35: Frequency response of FFT modelling transfer function

Static evaluation

Figure 4.42 and 4.43 show the static evaluation of the FFT demodulation self-sensing scheme where the BPF and detrending function were used respectively. From these results it is clear that the band-pass filtered system performs relatively well over the whole range. For the detrended case the maximum deviation is from the center position and below. From these analyses the detrending method is found to be much more noisy even in open loop evaluation.

Controller parameters

For stable suspension of the band-pass filtering FFT method the control parameters are set to the same values as in the band-pass sampling technique, and shown in table 4.6. The control parameters of the detrending FFT method were also kept the same as in the band-pass filtering FFT method to evaluate the effect of the BPF on the demodulation path. From simulation it was determined that the control parameters of the detrending FFT method could not be increased further. Both FFT schemes make use of the LPF_D in the PID's derivative path.

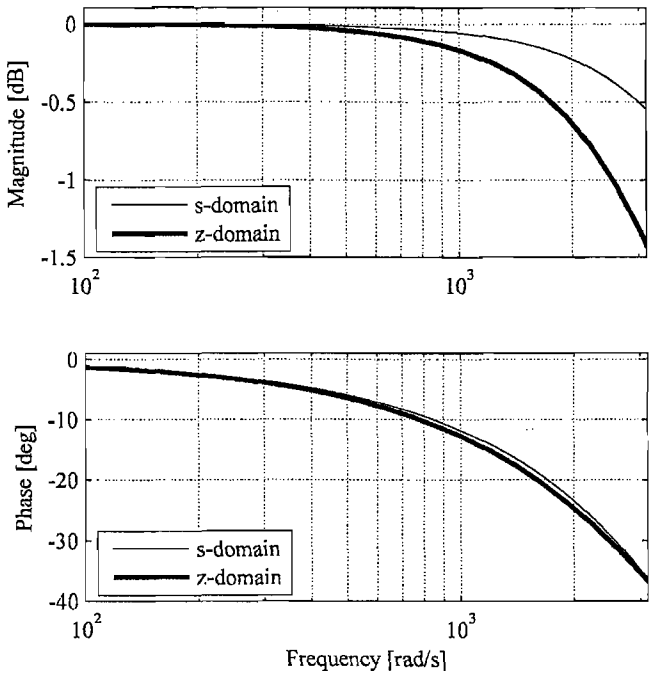

Figure 4.36: $G_d(z)$ frequency response: FFT with BPF demodulation method

Dynamic evaluation

The gain and phase plot of both FFT demodulation methods are obtained by exciting the AMB system with a 10 μm peak to peak sinusoidal position reference from 16 Hz to 1 kHz. The frequency and phase response are shown in figure 4.44 and was obtained using the FFT measurement method. The gain starts to deviate from 0 dB at approximately 150 Hz and reaches 20 dB at 400 Hz for both methods. The phase starts to deviate from 0 degrees at approximately 100 Hz and peaks at 600 Hz for both methods. From figure 4.44 the phase of the detrending FFT method is much lower between the transition of 0 dB and the peak. At 200 Hz the detrending FFT method's phase is 50 degrees lower than that of the band-pass FFT. It is also interesting to note that the phase shift of the BPF at 200 Hz (1256 rad/s) is only -5.7 degrees. There is therefore not a direct relationship between the BPF phase and the self-sensing output. The robustness of the two methods are shown in figure 4.45. The band-pass FFT method has a much higher sensitivity peak at 13.3 dB than the detrending FFT method at 9.7 dB. The BPF in the demodulation path has a smoothing effect on the position output, but increases the sensitivity peak. The conclusion is that the phase and gain can be directly linked to the sensitivity peak, thus robustness.

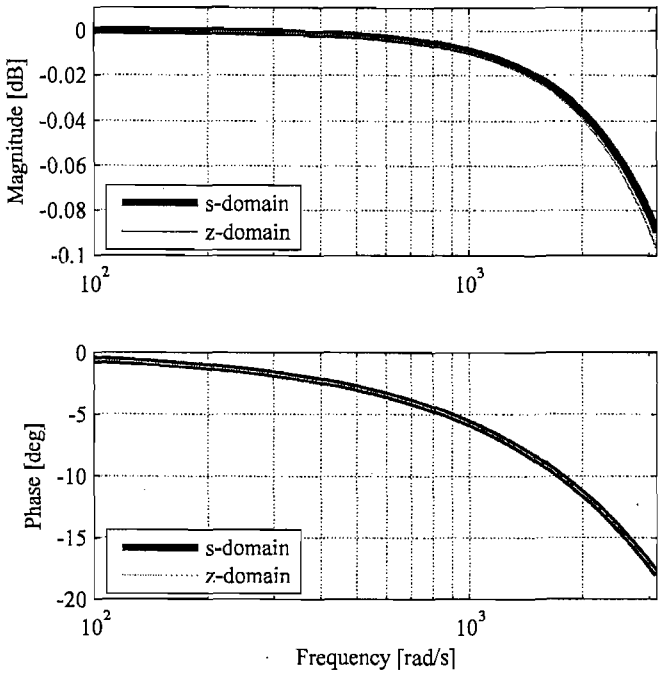

Figure 4.37: $G_d(z)$ frequency response: FFT with detrending demodulation method

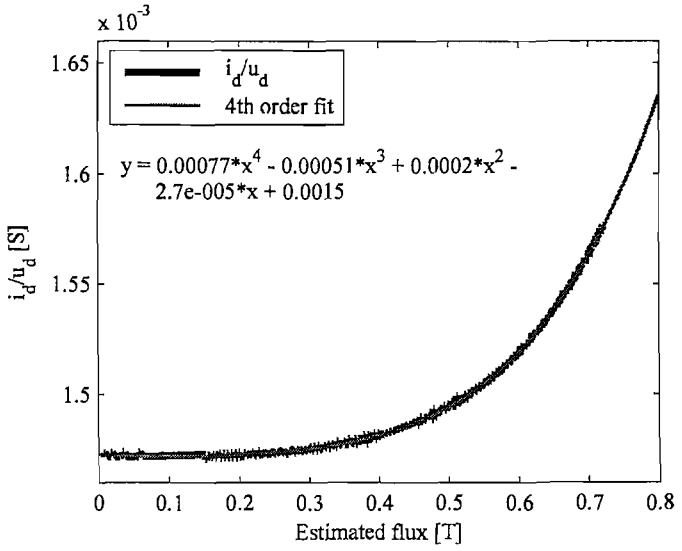

Figure 4.38: Nonlinear effects on self-sensing scheme: Band-pass filtered

4.6.5 Gradient method

The gradient method is a new proposed method which extracts the position information from the current ripple's gradient. The nonlinear compensation method proposed by Schammass is integrated into the

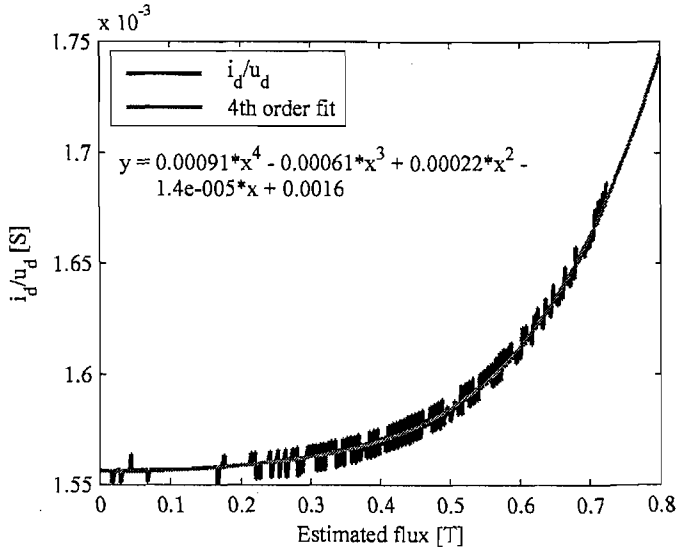

Figure 4.39: Nonlinear effects on self-sensing scheme: Detrended

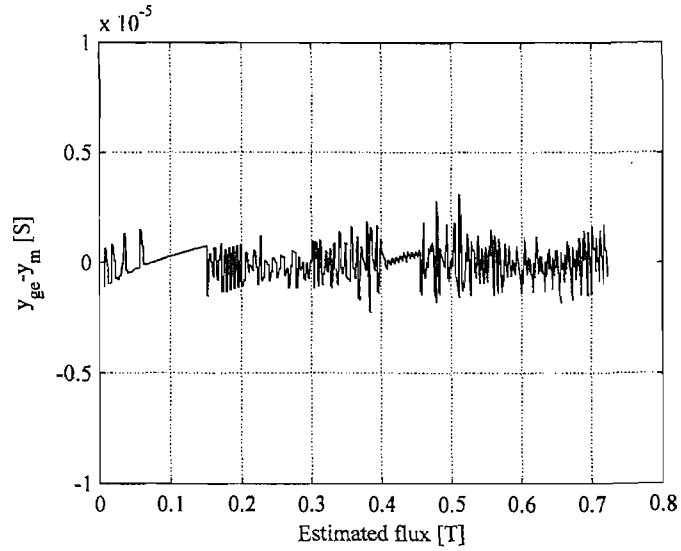

Figure 4.40: Nonlinear compensated output: Band-pass filtered

algorithm to compensate for nonlinearities. The advantage of the gradient method is that it eliminates all filters in the demodulation path.

Demodulator effects

Figure 4.46 shows the block diagram of the gradient self-sensing scheme. In the gradient self-sensing technique all filters in $G_d(z)$ are eliminated. The only component which has an effect on

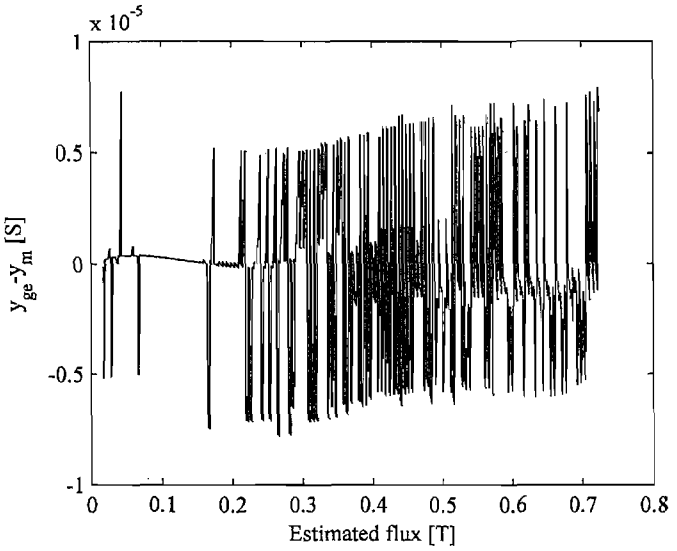

Figure 4.41: Nonlinear compensated output: Detrended

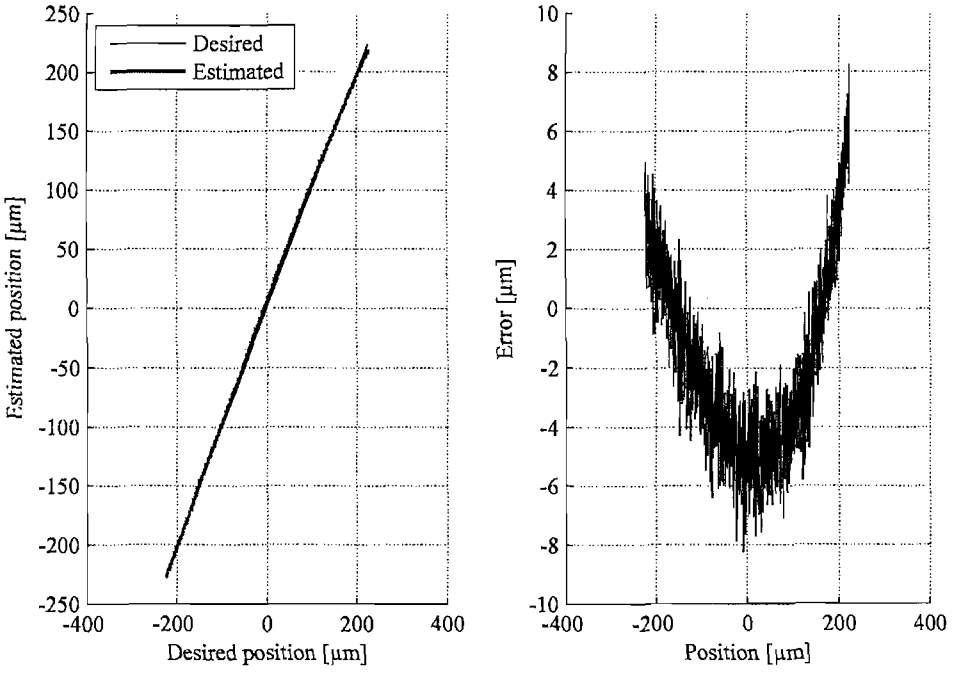

Figure 4.42: Static evaluation: Band-pass filtered FFT method

the frequency response is the sample and hold action of the position calculation. By evaluating the sample and hold transfer function with a sampling period of 100 µs the frequency response as shown in figure 4.47 is obtained. The effect of the sample and hold is evaluated in the range

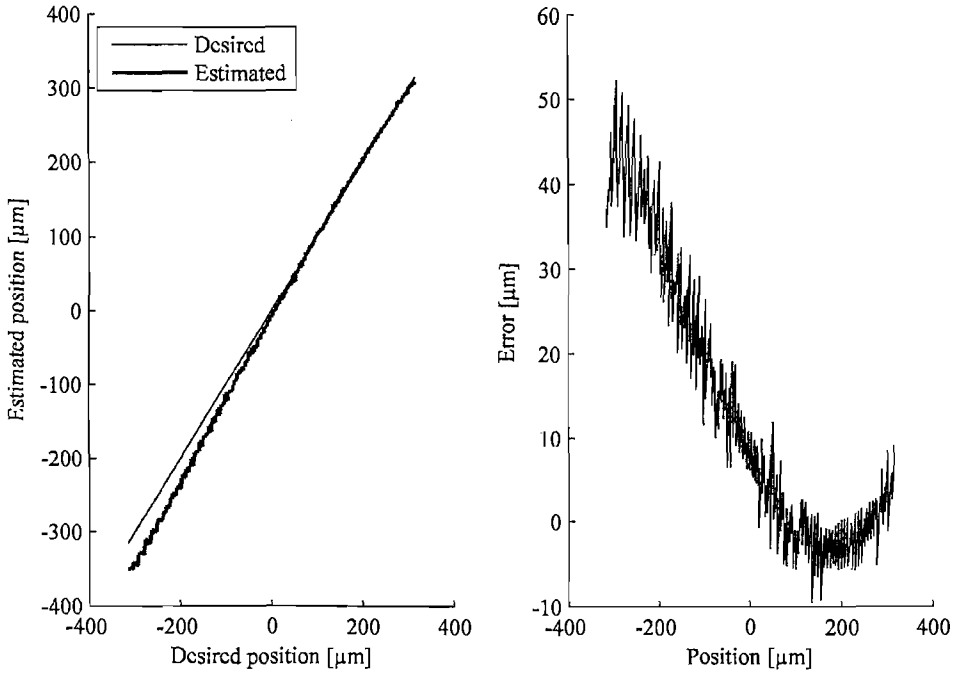

Figure 4.43: Static evaluation: Detrended FFT method

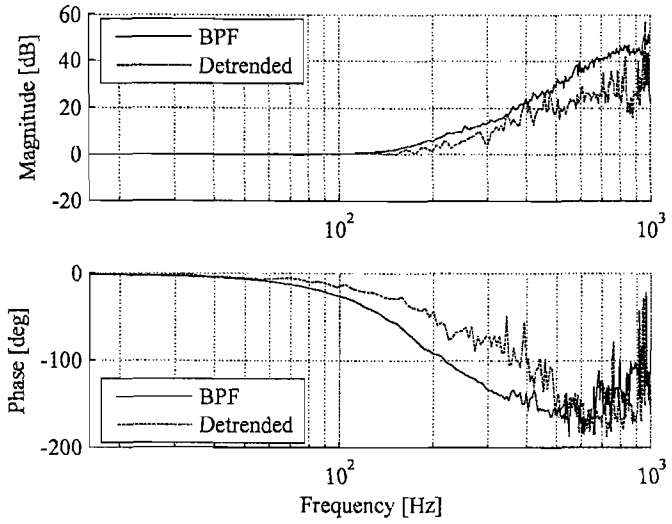

Figure 4.44: Gain and phase response: FFT method

of the AMB's bandwidth, which is 3200 rad/s or 500 Hz. From the magnitude response it is clear that the sample and hold has little effect on the gain of the system within the AMB's bandwidth range. From the phase plot the sample and hold has an effect on the phase shift but

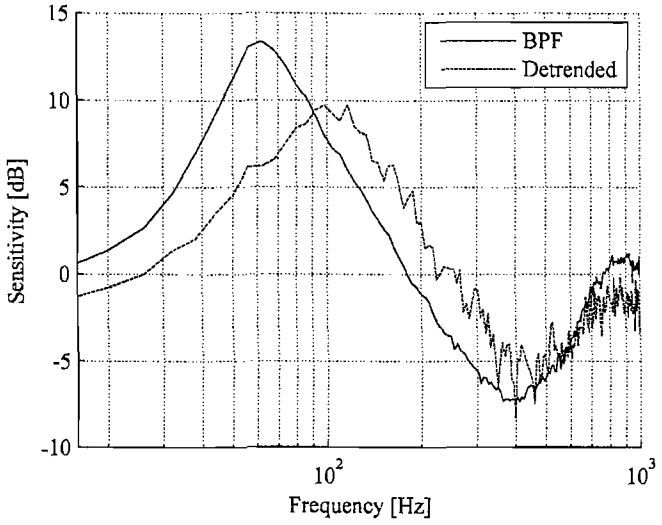

Figure 4.45: Sensitivity plot: FFT method

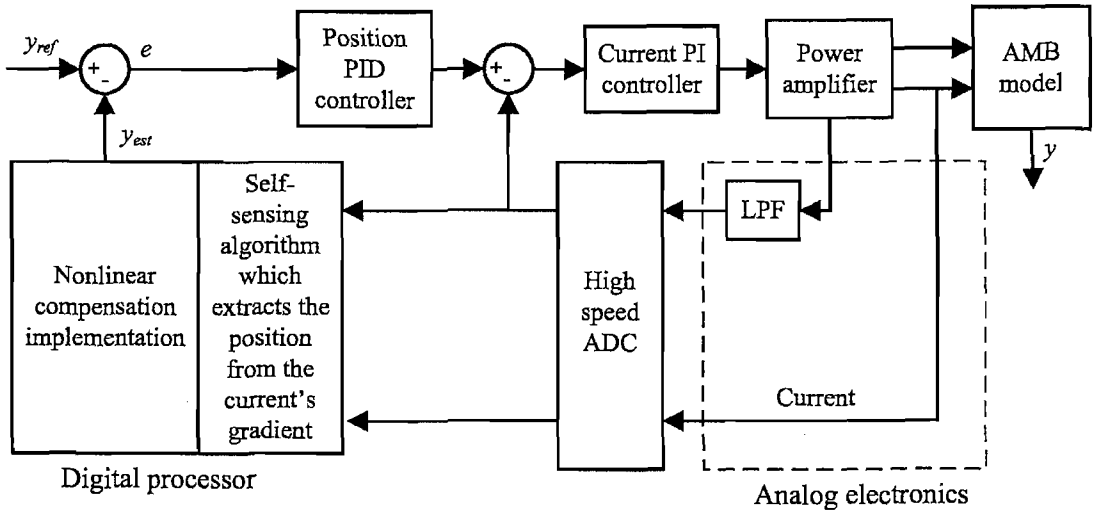

Figure 4.46: Block diagram of the gradient self-sensing scheme

it is relatively low and thus it will be neglected. For the gradient self-sensing technique $G_d(z)$ is set to one due to the results discussed above.

Nonlinear model identification

Figure 4.48 shows the nonlinear effect due to nonlinear effect in the TSM on the unscaled gradient demodulation method. The estimation function of the nonlinear effects are also shown. Figure 4.49 shows $y_{ge} - y_m$, where the output is close to zero. The evaluated nonlinear com-

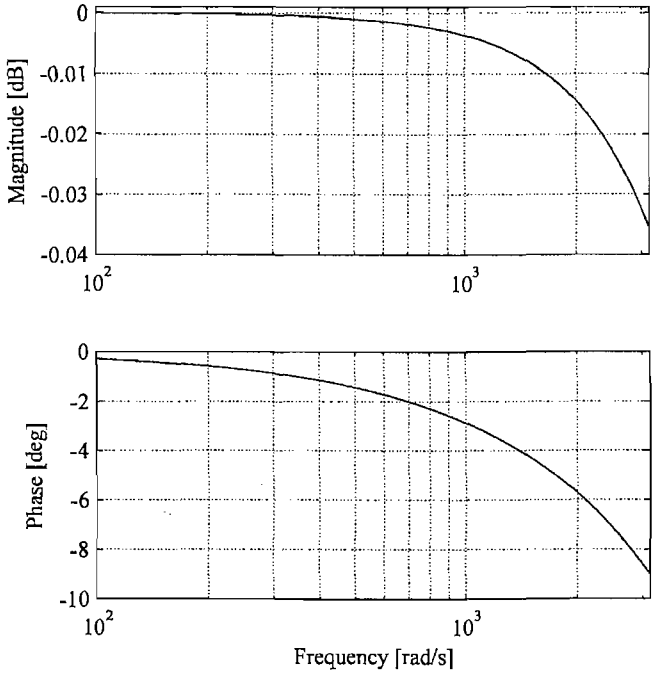

Figure 4.47: Frequency response of sample and hold

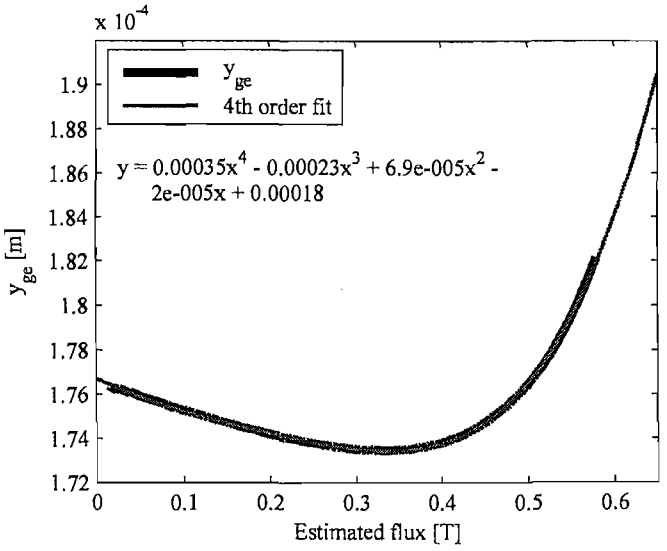

Figure 4.48: Nonlinear effects on self-sensing scheme

pensator performs well with the gradient demodulation method. The scaling constant k_x is determined as -1.02. This value is slightly larger than expected, since the gradient method transforms the gradient directly to scaled position. The value of k_x should have been equal to

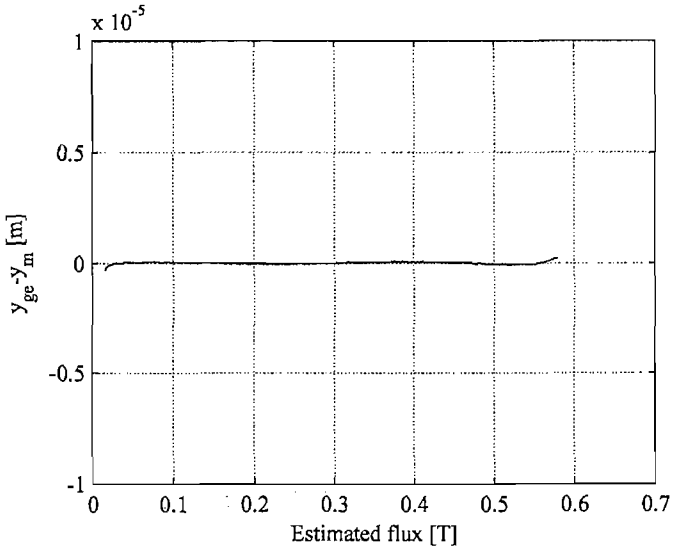

Figure 4.49: Nonlinear compensated output

one. The advantage of the nonlinear compensation method is that it compensates automatically for nonlinearities and scaling errors.

Static evaluation

Figure 4.50 shows the static evaluation of the gradient self-sensing scheme. The estimated position follows the desired position closely. The maximum open loop deviation from the desired position is 8.5 μm, thus the gradient method has high linearity.

Controller parameters

In the gradient self-sensing case the control parameters are close to the designed constants. The derivative constant was slightly reduced to 30. The power amplifier bandwidth is also set to 2500 Hz. The control parameters are shown in table 4.7. The LPF_D filter was used in the PID's derivative path.

Table 4.7: Control constants: Gradient method

Constant	Value
K_p	20000
K_d	30
$K_{p_{AMP}}$	0.7

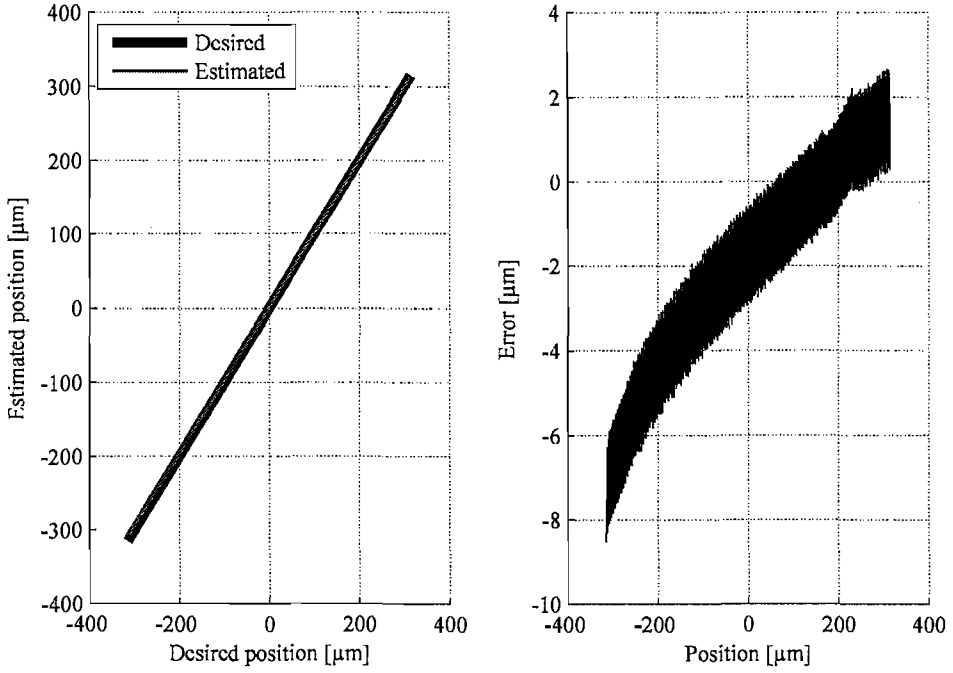

Figure 4.50: Static evaluation: Gradient method

Dynamic evaluation

The gain and phase plot of the gradient self-sensing scheme is obtained by exciting the system with a 10 µm peak to peak sinusoidal position reference from 16 Hz to 1 kHz. The frequency and phase response are shown in figure 4.51 and was obtained using the FFT measurement method. The gain starts to deviate from 0 dB at approximately 250 Hz. It is interesting to note that the gain is 20 dB at 700 Hz. From this it is clear that the gain of the gradient method is lower at high frequencies than the previous self-sensing schemes which made use of demodulation methods. The phase of the gradient demodulation method starts to deviate from 0 degrees at approximately 100 Hz and peaks at 400 Hz, which are approximately the same as the previous methods. The robustness of the gradient self-sensing system is shown in figure 4.52. The peak value is at 10.3 dB, which is defined as a class B AMB system.

4.6.6 Direct current measurement method

The DCM method is a unique method which eliminates the effect of duty cycle variation effects and reduces cross-coupling effects by forcing the duty cycle to 50 % when the position is estimated. A method to reduce possible high frequency noise on the sensed current is implemented and evaluated. This is discussed in detail in the next section.

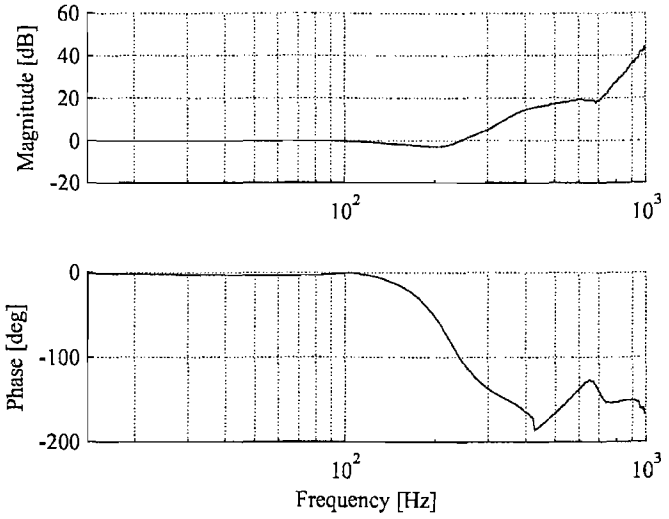

Figure 4.51: Gain and phase response: Gradient method

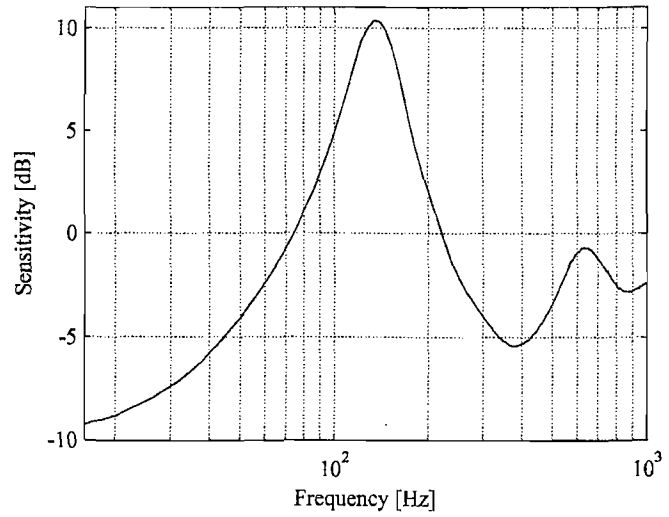

Figure 4.52: Sensitivity plot: Gradient method

Noise reduction

Figure 4.53 shows the block diagram of the DCM self-sensing scheme. In simulation the sampled ripple is passed through a low order FIR filter to reduce high frequency noise in the practical implementation. The filter has the disadvantage of phase shift, but the noise reduction is much more beneficial to self-sensing stability.

The order of the filter plays an important part in the stability of the DCM method. Since a FIR

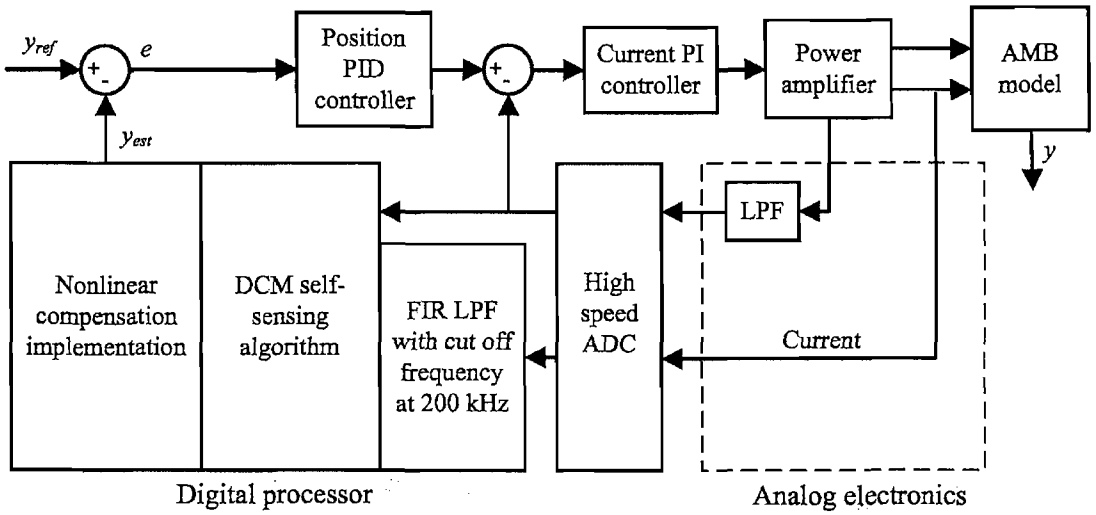

Figure 4.53: Block diagram of the DCM self-sensing scheme

filter is used, delayed input samples must be used to implement the filter. The delay buffer will make use of delayed ripple values which fall in the control cycle. If an 8^{th} order FIR filter is used, it makes use of 7 delayed samples of the control cycle and the first sample of the sensing cycle to calculate the first sensing cycle point. From the illustration it is clear that the sensing cycle is not only dependent on sensing cycle data points, but also the control cycle data points. If the order is too high the control cycle will have a large effect on the filtered sensed cycle. An 8^{th} order FIR filter is used in the simulation, thus 7 delayed samples are used. The total number of samples in each sensing cycle is 50 if the sample rate of the FIR filter is at 1 MHz and the switching frequency is at 20 kHz. Due to the 7:50 ratio the 7 samples should not have an enormous effect on the sensing cycle. The worst case would be if the duty cycle of the control cycle is above 86 %. Figure 4.54 shows the 8^{th} order FIR filter with the cutoff frequency of 20 kHz and stop band of 200 kHz. Due to the 25 degree phase shift the ripple is not synchronized with the PWM signal. By using (4.8) the PWM signal and filtered ripple signal can be synchronized by delaying the filtered component with the calculated samples with the power amplifier switching frequency (f_s at 20 kHz).

$$\begin{aligned} S &= \frac{\theta}{360.fs.dt} \\ &= 3.5 \end{aligned} \tag{4.8}$$

S is the delay in samples, θ is the phase shift in degrees, fs is the switching frequency and dt is the simulation time interval. From this calculation 3 delayed samples are implemented in simulation. Figure 4.55 shows the real current and filtered current which is approximately 3 samples apart.

Demodulator effects

In the DCM self-sensing technique $G_d(z)$ consists of a sample and hold and the noise reduction filter. The noise filter is evaluated at 1 MHz which is far above the sample and hold frequency,

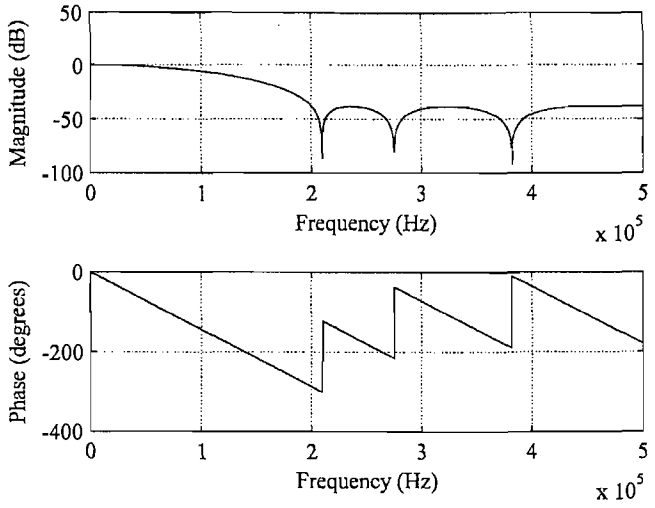

Figure 4.54: 8th order noise reduction FIR filter

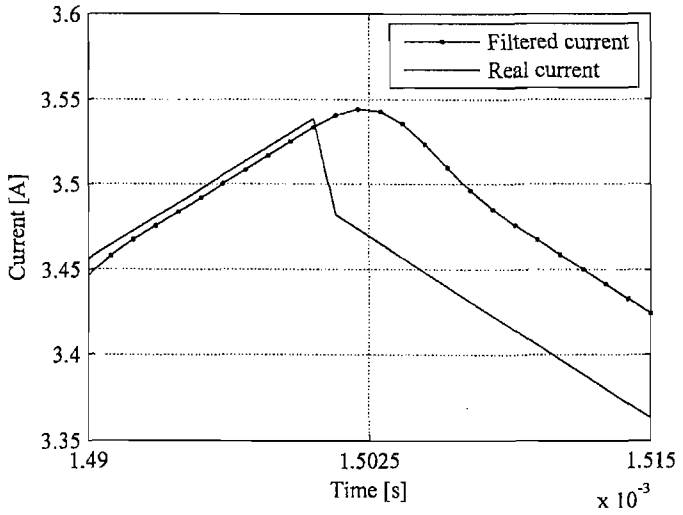

Figure 4.55: Nonlinear effects on self-sensing scheme

thus the effect of the filter will be neglected. The sample and hold effect of the self-sensing algorithm has an effect on the system. The sample and hold must be evaluated with a sampling time of 100 μs. This is due to the control and sensing cycle implementation of the DCM self-sensing technique. By evaluating the sample and hold transfer function the frequency response is determined as shown in figure 4.47. The magnitude response has little effect on the gain of the system and thus it will be neglected. From the phase plot the sample and hold has an effect on the phase shift but it is relatively low. For simplicity the phase effect is neglected and $G_d(z)$ is set to one.

Nonlinear model identification

The scaling is applied as discussed in chapter 3. The scaled current is divided by 70 to transform the ripple amplitude to the same unscaled position range as the previous demodulation methods for comparison only. If the division is excluded the output of $y_{ge} - y_m$ and k_x would be 70 times larger. Figure 4.56 shows the nonlinear effects and the estimation function. Figure

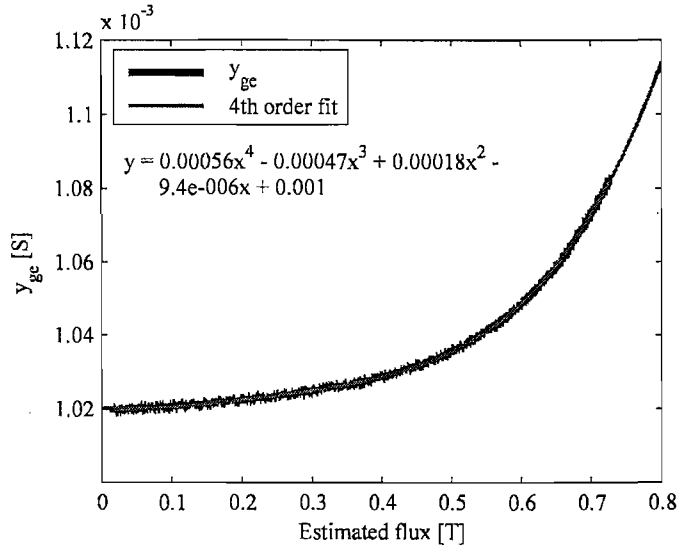

Figure 4.56: Nonlinearity due to saturation

4.57 shows $y_{ge} - y_m$. From the figure it is clear that the nonlinear compensator performs well. The scaling constant k_x is determined as -1.15.

Static evaluation

Figure 4.58 shows the static evaluation of the DCM self-sensing scheme. From these results it is clear that the system performs well in the range of 200 μm. Beyond the 200 μm range the estimated position starts to deviate from the desired position.

Controller parameters

The DCM method is the only self-sensing scheme in which the designed control parameters could be used. The bandwidth of the current loop is set to 2500 Hz. The designed control parameters are shown in table 4.8. The filter LPF_D is implemented with the DCM method, but the response of the LPF_D is altered. It was found that by reducing the order of LPF_D the performance is increased. Figure 4.59 shows the frequency response of LPF_D for the DCM method.

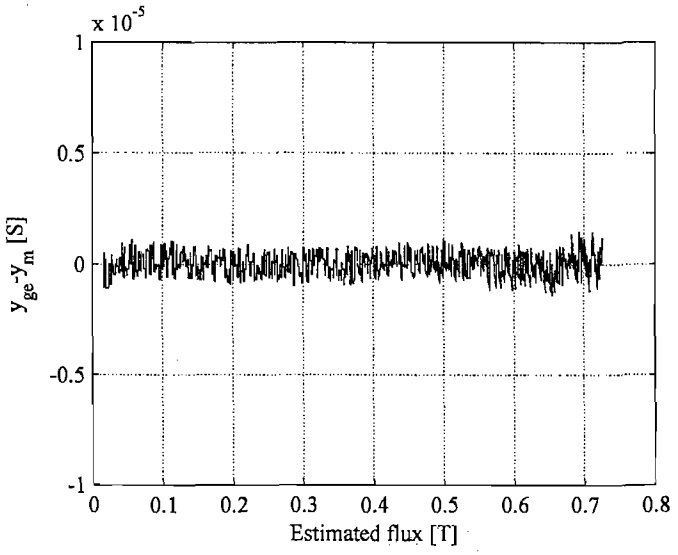

Figure 4.57: Nonlinear compensated output

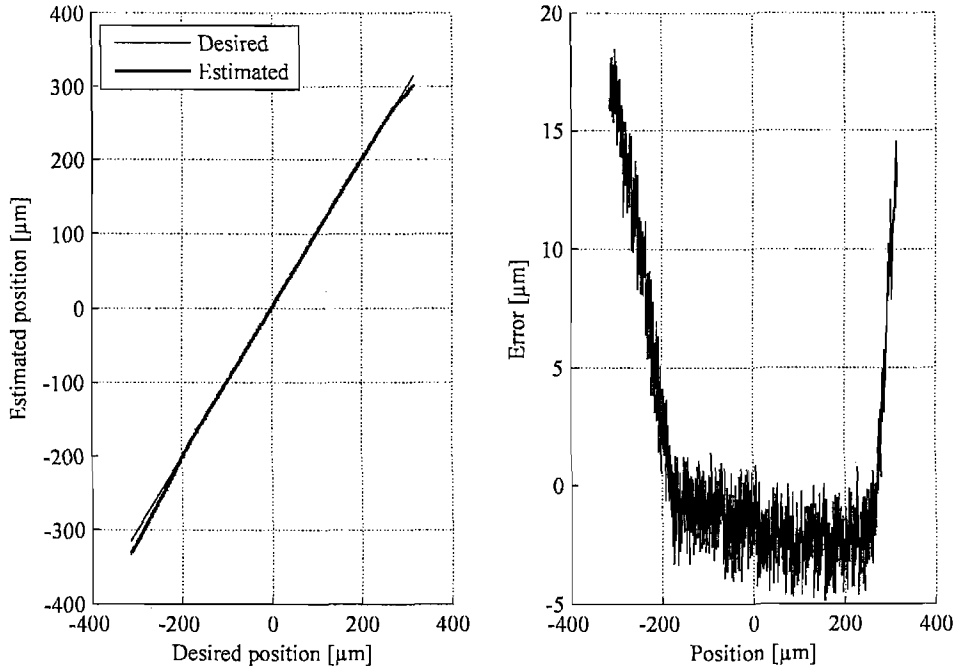

Figure 4.58: Static evaluation: DCM method

Dynamic evaluation

Figure 4.60 shows the gain and phase relation obtained by the FFT method. The gain starts to deviate from 0 dB at approximately 100 Hz and reaches 20 dB at 700 Hz. The phase starts

Table 4.8: Control constants: DCM method

Constant	Value
K_p	20000
K_d	38
$K_{p_{AMP}}$	0.7

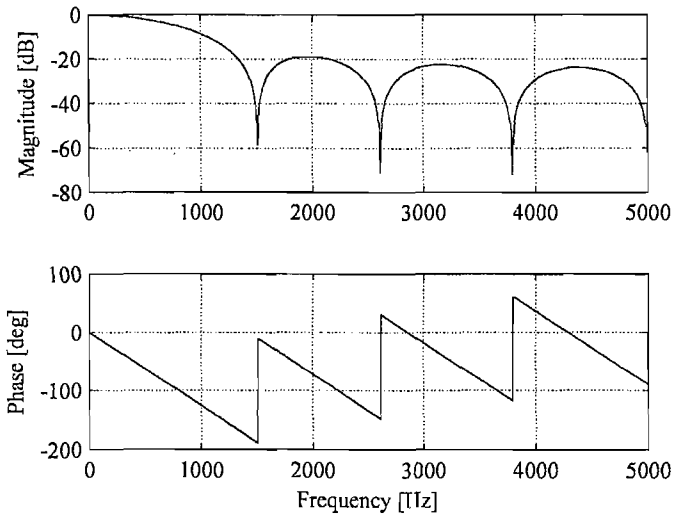

Figure 4.59: Frequency response of PID derivative path filter

to deviate from 0 degrees at an early stage, but the deviation is small and gradual. The major phase change is at 300 Hz. The phase reaches only 50 degrees at 1000 Hz, which is about 130 degrees less than in the previous phase analysis. Figure 4.61 shows the robustness of the DCM method, where the peak value is 6.2 dB when excited with a 10 μm peak to peak sinusoidal position reference. The requirement for an industrial AMB system is 8 dB which means that the DCM self-sensing scheme meets a new commissioned industrial system which is of class A.

4.6.7 Cross-coupling

In this section the effect of cross-coupling will be evaluated. The effect of cross-coupling on the DCM self-sensing technique is compared with the cross-coupling effect on the digital FIR filter demodulation method. All the self-sensing schemes are affected the same way by cross-coupling except the DCM technique which makes use of the 50 % sensing cycle.

For this analysis the position of the rotor is forced to 200 μm, 0 and -200 μm respectively and all the coils are supplied with a bias current of 3 A. For the vertical analysis the bottom coil is

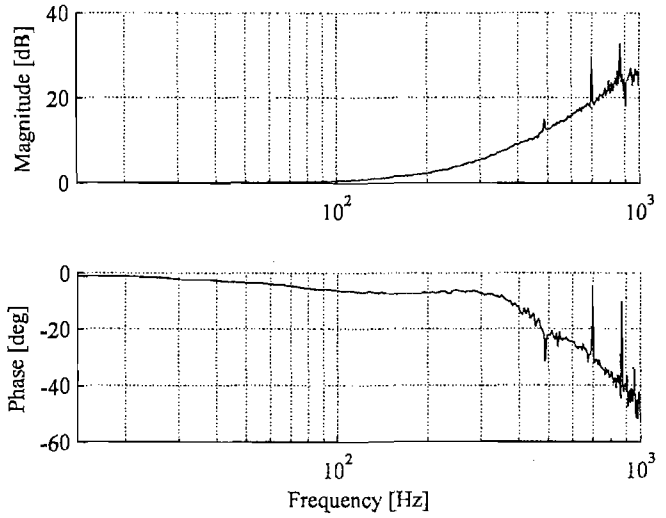

Figure 4.60: Gain and phase response: DCM method

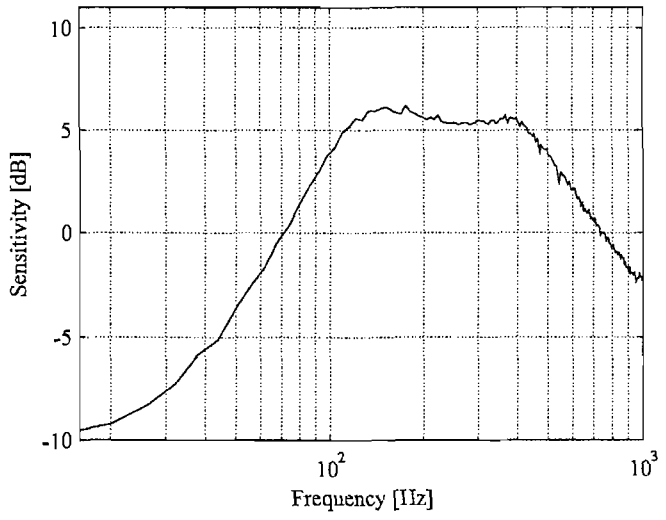

Figure 4.61: Sensitivity plot: DCM method

additionally supplied with a 2 A_{p-p} sinusoidal signal with a frequency of 200 Hz or 500 Hz. For the horizontal analysis all the coils are supplied with a 3 A bias current and the left coil is additionally supplied with a 2 A_{p-p} sinusoidal signal with a frequency of 500 Hz. Hysteresis is included in the simulation since it is unavoidable in practice, but due to the low current levels the magnetic material is operated close to its linear range thus the effect of saturation should not be significant. The top coil is used for self-sensing and the effect of cross-coupling on the estimated position is measured.

Figure 4.62 and 4.63 shows the effect of cross-coupling on the FIR filter self-sensing technique in the vertical axis. In this analysis the sensing coil duty cycle is at approximately 50 % due to the constant bias current but the controller varies the duty cycle in the bottom coil due to the sinusoidal current reference. The effect of cross-coupling due to a 200 Hz current reference and the different rotor position references induce an estimated position error which varies from approximately 1.5 to 2.5 μm and for the 500 Hz current reference the estimated position varies from approximately 2 to 6.5 μm. It is interesting to note that there is a second frequency component present, which is at double the frequency of the supplied current. This is due to the amplitude demodulation method used in the self-sensing technique. In chapter 3 section 3.9.3

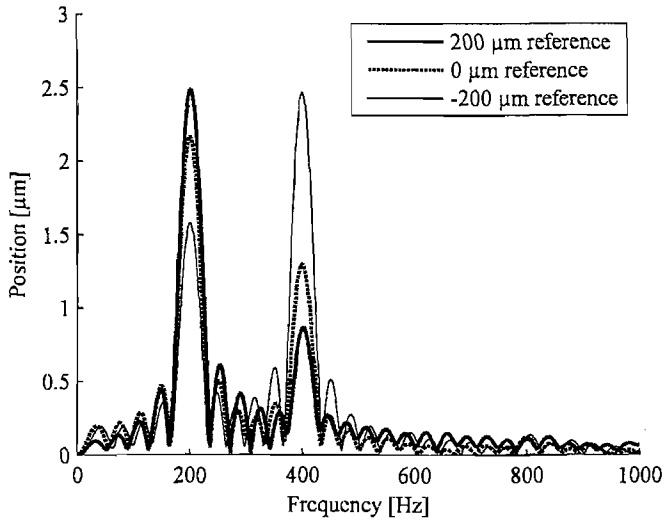

Figure 4.62: Cross-coupling effect on top coil: Analog demodulation self-sensing scheme, bottom coil excited with 2 A, 200 Hz current reference

the conclusion was made that the estimated position is affected by the amount of variation in duty cycle in other coils with the sensing coil's duty cycle at 50 %. This effect will be evaluated by varying the duty cycle of the bottom coil with a 100 Hz and 200 Hz current reference with different current amplitudes which will result in the same maximum duty cycle variation. This will prove that duty cycle cross-coupling is variation dependent, thus amplitude and not frequency dependent. Figure 4.64 shows the cross-coupling duty cycle amplitude dependency for the 100 Hz evaluation on the left and the 200 Hz evaluation on the right. From this evaluation it is clear that the duty cycle cross-coupling is dependent on the amount of deviation and not the rate of deviation, since in both methods the duty cycle amplitude is at 17 % peak to peak. It is important to note that saturation was neglected to eliminate the effect of saturation due to two different current amplitudes. At higher current reference frequencies the bandwidth of the power amplifier starts to play a role, which increases the duty cycle cross-coupling effect. Assuming the current reference of the bottom coil to be outside the bandwidth of the power amplifier the duty cycle of the bottom coil will vary between its minimum and maximum values, which will result in a maximum duty cycle cross-coupling from the bottom coil to the top sensing coil. Figure 4.65 shows the effect of the left horizontal coil with a 2 A, 500 Hz cur-

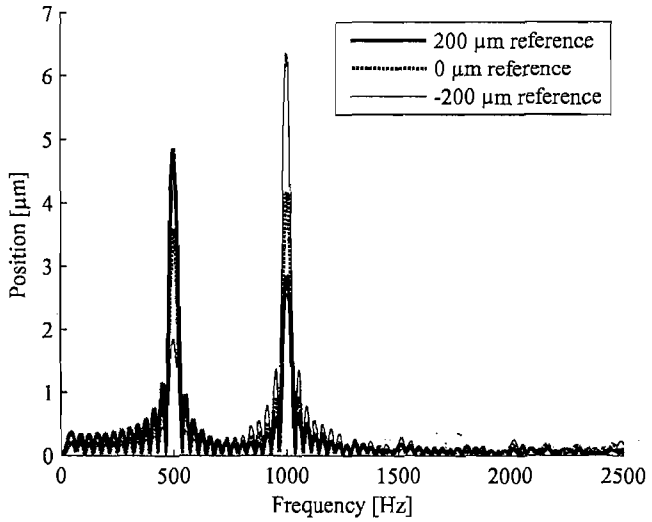

Figure 4.63: Cross-coupling effect on top coil: Analog demodulation self-sensing scheme, bottom coil excited with 2 A, 500 Hz current reference

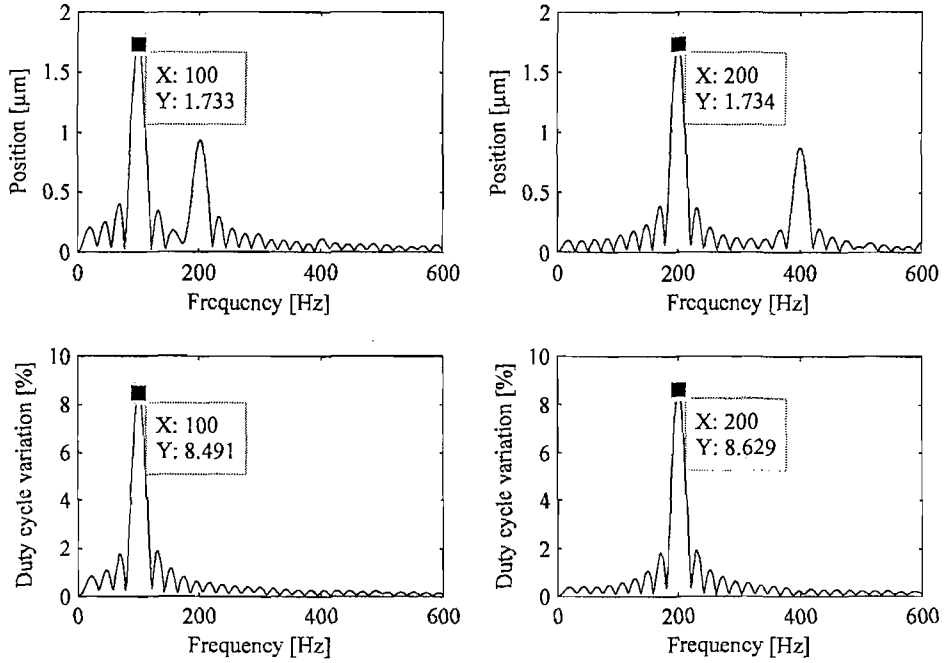

Figure 4.64: Amplitude dependency: Cross-coupling effect on top coil with bottom coil excited with 100 Hz (left) and 200 Hz (right) and constant duty cycle variation in bottom coil

rent reference on the top coil. The error induced by cross-coupling is substantially large due to the pole distances. The left and right horizontal poles are the closest poles to the top vertical pole and thus the cross-coupling effect is larger. Figure 4.66 and 4.67 shows the effect of

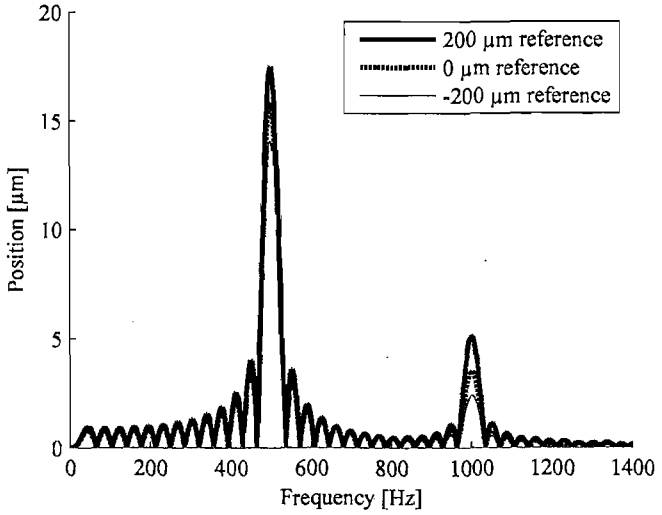

Figure 4.65: Cross-coupling effect on top coil: Analog demodulation self-sensing scheme, left horizontal coil excited with 2 A, 500 Hz current reference

cross-coupling on the top vertical coil which make use of the DCM self-sensing technique. The bottom coil is excited with a 2 A 200 Hz and 500 Hz current reference respectively. In the DCM method all the duty cycles are forced to 50 % in the sensing cycle and from the results it is clear that cross-coupling is reduced in the vertical axis. By comparing figure 4.62 and 4.63, 4.66 and 4.67 duty cycle cross-coupling in the vertical axis is reduced by a factor of at least 3.3 at 200 Hz and for 500 Hz a factor of at least 2.1.

Figure 4.68 sows the cross-coupling effect of the left horizontal coil with a 2 A_{p-p} 500 Hz sinusoidal current reference on the top vertical coil as sensing coil. Again, all duty cycles are forced to 50 % in the sensing cycle. By comparing figure 4.65 and 4.68 the cross-coupling effect is mostly eliminated.

4.6.8 Overview of results

Table 4.9 summarises the gain, phase and sensitivity simulation results for the different self-sensing schemes. From the table the effect of the gain and phase will be related to the sensitivity. In the table the frequency gain points at 0 dB and 20 dB will be used as gain performance measures as well as the 0 degree and 180 degree phase points.

The frequency where the sensitivity is at its maximum is affected by the different self-sensing schemes. The frequency effect of the different self-sensing schemes can be determined from the

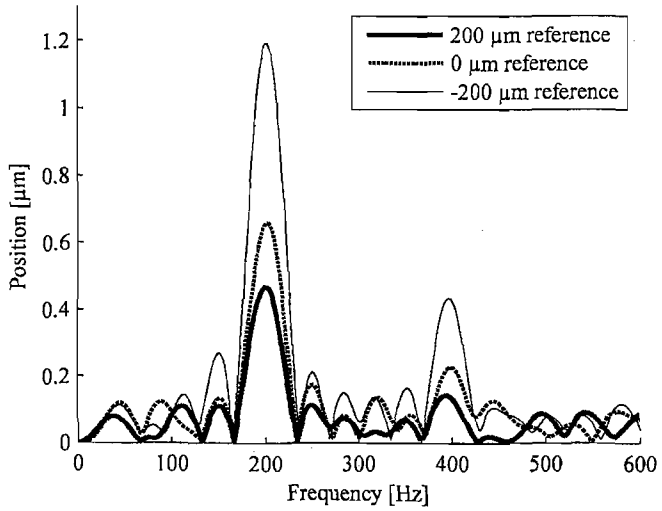

Figure 4.66: Cross-coupling effect on top coil: DCM self-sensing scheme, bottom coil excited with 2 A, 200 Hz current reference

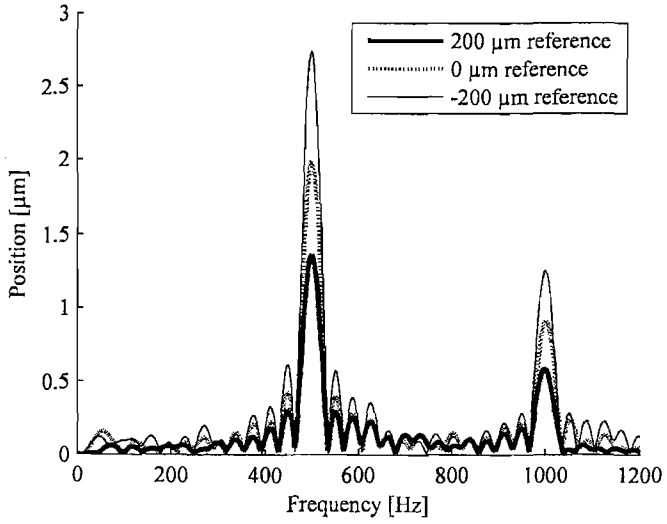

Figure 4.67: Cross-coupling effect on top coil: DCM self-sensing scheme, bottom coil excited with 2 A, 500 Hz current reference

robustness plots.

The point where the gain deviates from 0 dB starts from around 100 Hz and upwards for the different self-sensing schemes. The band-pass sampling and gradient methods have slightly lower gains at higher frequencies. The points where 20 dB is reached for the band-pass sampling and gradient methods are at higher frequencies. The phase of the band-pass sampling

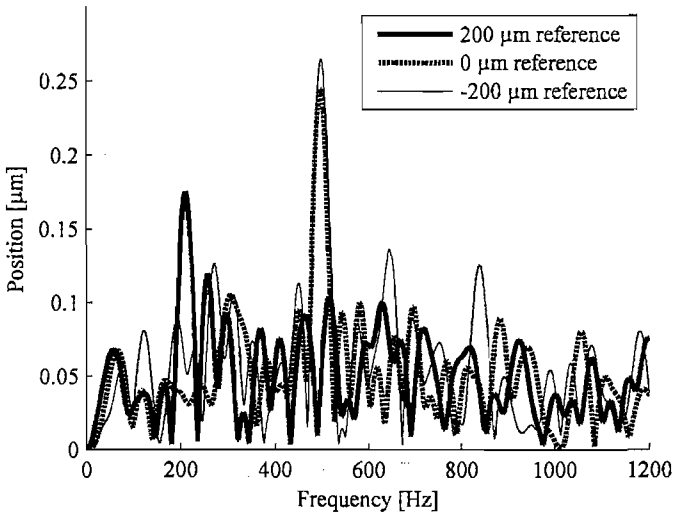

Figure 4.68: Cross-coupling effect on top coil: DCM self-sensing scheme, left horizontal coil excited with 2 A, 500 Hz current reference

and gradient methods is the same as that of the analog, and digital methods. The band-pass sampling and gradient methods have lower sensitivity gains as the analog and digital methods. From these comparisons it can be concluded that the frequency where the gain deviates from 0 dB affects the sensitivity. The sensitivity decreases as the frequency increases.

By comparing the two FFT demodulation methods the point where the gain starts to deviate from 0 dB is approximately the same frequency for both methods. The deviation for the 0 degree phase is also at the same frequency . The maximum values, namely the 20 dB and the phase peak, are also at the same frequencies for both methods. The gain and phase of the detrending FFT method are lower than that of the band-pass filtering method between 100 and 600 Hz. From the above results the following conclusions can be made: 1) The frequencies where the gain reaches 20 dB affects the sensitivity. 2) The frequency where the phase peaks (180 deg) affects the sensitivity. 3) The transition shape of the response to these frequency points are also of importance. The closer the response is to zero the lower the sensitivity becomes. This was obtained from the FFT demodulation methods where the transition shape of the response made a 3.6 dB improvement on the sensitivity.

If the gradient method is compared to the DCM method the 0 to 20 dB gain is in the same range, but there is a large difference between the two methods' phases. The DCM reaches only 50 degrees at 1 kHz where the gradient method reaches the peak at 400 Hz. From this it can be concluded that the higher the phase lag the lower the robustness.

From the results above it can be assumed that if the gain and phase can be kept low over the AMB's bandwidth range the robustness requirements can be met. The gain and phase does not have to follow the ideal case, 0 dB gain and 0 degrees phase, but there are certainly upper limits on these parameters.

Table 4.9: Self-sensing schemes benchmarking

Sensing method	0 dB	20 dB	0 degree	180° phase peak	Sensitivity (dB)
Analog	150 Hz	400 Hz	100 Hz	400 Hz	13.3
Digital	150 Hz	400 Hz	100 Hz	400 Hz	13.7
BP sampling	300 Hz	450 Hz	100 Hz	400 Hz	11.6
FFT BPF	150 Hz	400 Hz	100 Hz	600 Hz	13.3
FFT detrended	150 Hz	400 Hz	100 Hz	600 Hz	9.7
Gradient	250 Hz	700 Hz	100 Hz	400 Hz	10.3
DCM	100 Hz	700 Hz	300 Hz	50° @ 1 kHz	6.2

In this chapter all the different self-sensing schemes were simulated and performance results were obtained. By comparing the performance results of the different self-sensing schemes it was found that the phase shift effects can be linked to robustness. In the methods in which the BPF filter are eliminated the noise increased. It is concluded from the results that the removal of the BPF increases noise levels, but the robustness of the self-sensing scheme was improved.

The filters implemented in the PID controller also have an effect on the robustness, since in the DCM the self-sensing scheme's sensitivity peak is much lower due to the low order filter used.

The effect of cross-coupling on the DCM technique with the 50 % sensing cycle was evaluated. From the analysis it was found that the coil apposing to the sensing coil has the maximum cross-coupling effect. By using the 50 % sensing technique cross-coupling can be reduced by a factor of up to 3.3. Thus the 50 % sensing cycle increases the overall performance in a coupled AMB system.

Chapter 5

Hardware implementation

In this chapter the hardware and the implementation of different self-sensing schemes are discussed. The hardware is divided into the power amplifier electronics board, the digital electronics board and the analog electronics board. Each of the electronic boards is discussed in short together with its specifications. The digital implementation of each self-sensing scheme is discussed along with its associated signal conditioning electronics. The alterations that were made to the theoretical design are explained in detail. The performance of each self-sensing scheme is evaluated and discussed. The effect of cross-coupling is evaluated using the DCM self-sensing technique. The digital limitations of each self-sensing scheme are highlighted and future recommendations are identified.

5.1 Integrated power amplifier

Compactness and the reduction of wiring costs are the main motivation for the development of the integrated power amplifier for industrialization purposes. By reducing the wiring length, the noise levels are reduced. As stated earlier, the hardware of the integrated controller are subdivided into the three sections, namely the power amplifier electronics, digital electronics and analog electronics. Each of these three sub-components consists of a physical circuit board. These boards are piggybacked onto one another via high power and small signal connectors. Figure 5.1 shows the piggybacked integrated power amplifier board, with the power electronics board at the bottom, the digital electronics board in the middle and the analog electronics board on top. Each of the boards will be discussed in the following sections.

5.1.1 Power electronics

The power electronics is set up in such a manner that six half bridges are configurable into two three phase bridges or two full H-bridge configurations. Figure 5.2 shows the basic layout of the power amplifier board. Decoupling capacitors and switching resistors are omitted for simplicity. This configuration capability makes the power electronics usable for AMB applications

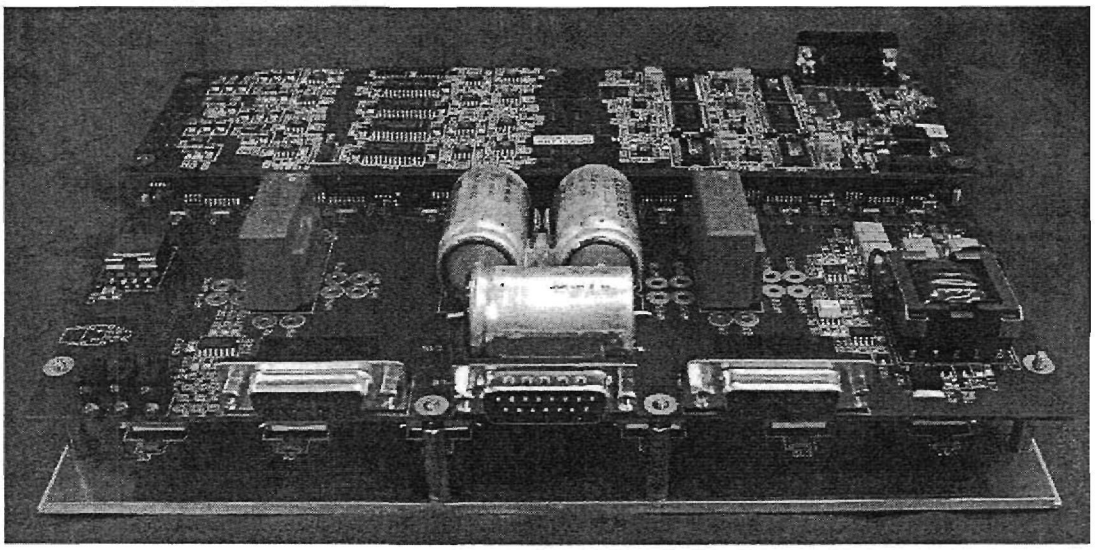

Figure 5.1: Integrated power amplifier

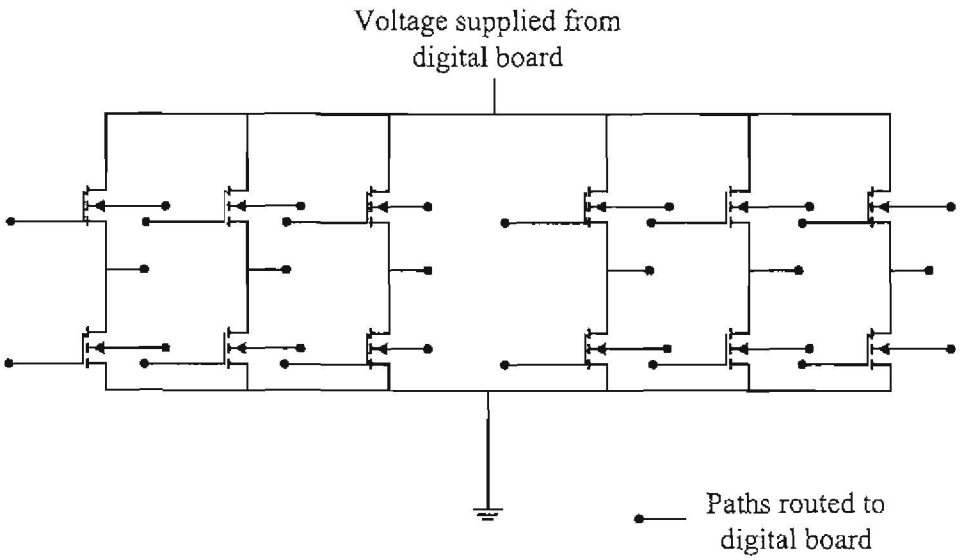

Figure 5.2: Power electronics block diagram

as well for motor drives. For this research the two full H-bridges configuration is used.
The dual power amplifier configuration makes it possible to suspend a rotor in one degree of freedom with one power amplifier board. The drivers used to switch the switching components are situated on the digital board, which will be discussed in the next section. The power electronics board is constructed on an aluminium substrate, which optimizes the heat transfer from the power electronics to the heatsink. Figure 5.3 shows the physical aluminium substrate power electronics board. The power amplifiers have the following capabilities as stated in table 5.1.

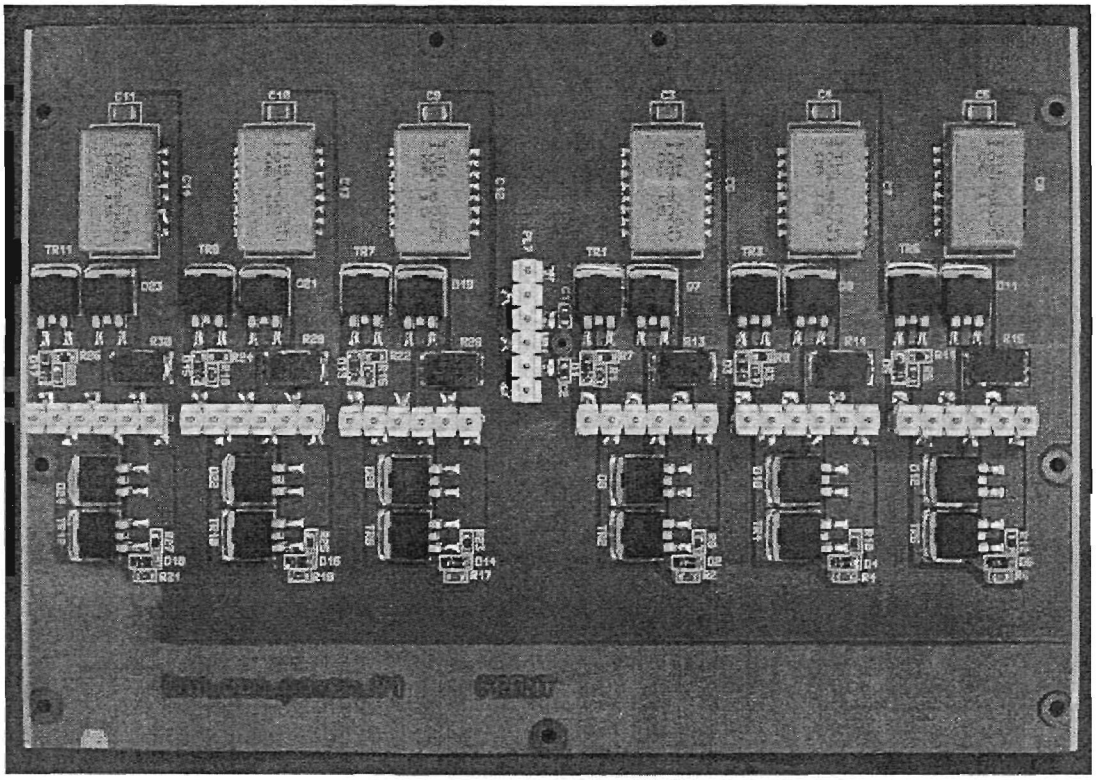

Figure 5.3: Power electronics board

Table 5.1: Power amplifier capabilities

Current capability	7.5 A rms
Switching frequency capability	20 - 50 kHz
Current sensing capability	25 A @ 200 kHz

5.1.2 Digital electronics

The digital electronics board forms the heart of the integrated power amplifier and the self-sensing schemes. Figure 5.4 shows the block diagram of the digital board consisting of power amplifier drivers, current and voltage sensors, a TMS320F2812 controller, a high speed Spartan 3E series FPGA , communication interface and power supplies. The H-bridge drivers are controlled by the TMS which has onboard PWM controllers. The current sensors (LAH25-NP) used to sense the ripple are also integrated with the digital board. The outputs of the current and voltage sensors are fed to a connector which connect to the analog electronics board. The position and current control are implemented on the TMS. The power amplifier feedback currents are fed from the analog electronics board where they are filtered and scaled, then fed back to the digital board and digitized for current control. The position is also fed from the analog board to the digital board and digitized for position feedback. The current and position signals

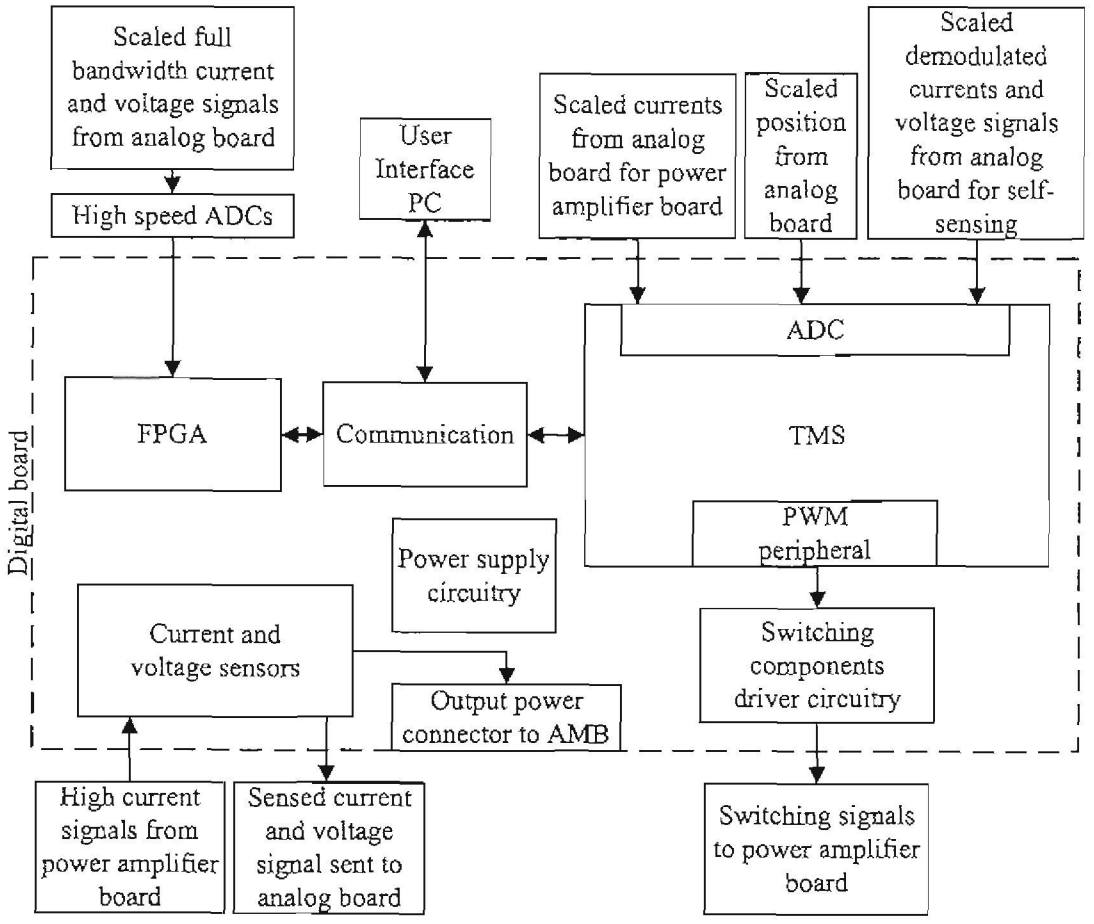

Figure 5.4: Block diagram of digital electronics circuit

are digitized by the TMS's onboard ADC.

Two currents and two voltages with high bandwidth are digitized by external high sampling ADCs. The four digitized signals are passed to the FPGA where they are used as inputs for the self-sensing algorithm. The results of the algorithm are passed to the TMS through a bidirectional communication interface. The algorithm result is then used as the position feedback component in the position control loop of the TMS. The main purpose of the FPGA is to evaluate complex algorithms in a specified time frame. The physical circuit of the digital board is shown in figure 5.5.

5.1.3 Analog electronics

In this section the analog electronics board is discussed. The board consists of self-sensing circuitry and electronics which form an integral part of the power amplifier operation. Figure 5.6 shows a block diagram of the analog board. The analog electronics which form part of the integrated power amplifier are the current feedback electronics and the position feedback

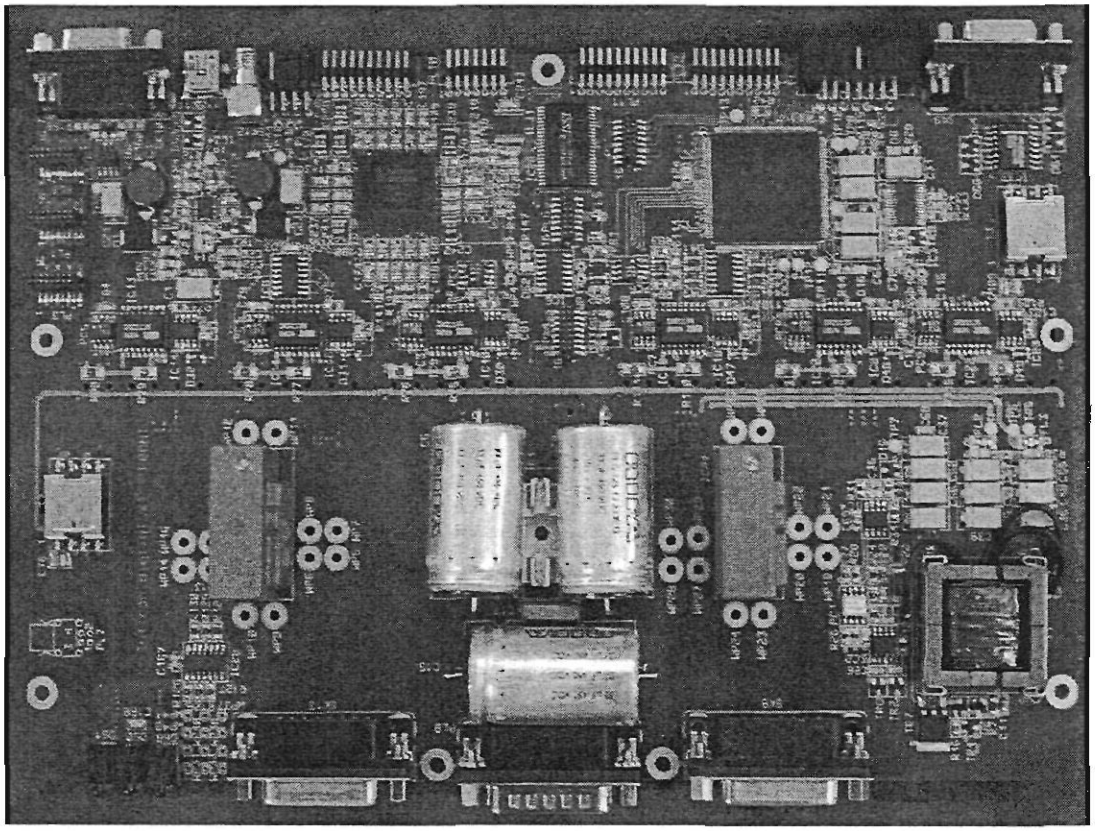

Figure 5.5: Digital electronics board

electronics. Both the sensed current and position signals are measured differentially with a differential operational amplifier and passed through LPFs with 5 kHz cutoff frequency. The filtered signals are scaled for digitization. Both signals are digitized using the TMS ADCs.

The self-sensing electronics also make use of the differentially measured signals. Self-sensing is implemented in three ways as shown in figure 5.7. Option one shows the analog implementation, where the current and voltage signals are passed through the demodulator and are shifted to low frequencies and digitized by the TMS ADCs.
With option two, the current and voltage signals are only band-pass filtered and then passed to the high speed ADC for further demodulation. Option two applies to the digital demodulation method and the band-pass filtered FFT demodulation method. Method 1 and 2 was designed and implemented on the analog board.
With option three the sensed current signals are rescaled using the sample and hold method. The rescaled current signals are passed to the high speed ADC for digitization. Option three applies to the DCM self-sensing technique. Since the circuitry was not initially designed with the sample and hold circuitry, some alterations were made to accommodate the sample and hold circuitry. Figure 5.8 shows the physical analog board.

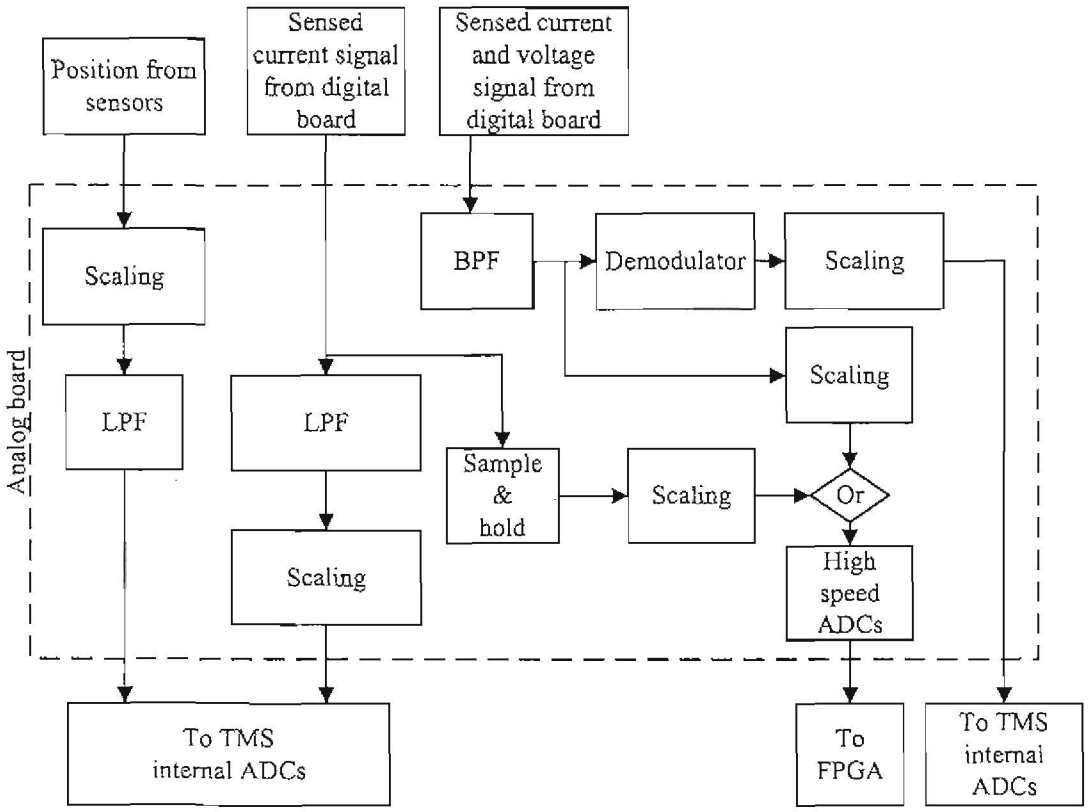

Figure 5.6: Block diagram of analog board

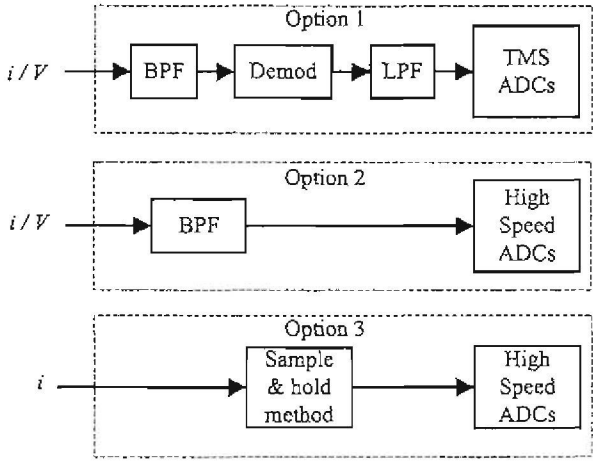

Figure 5.7: Self-sensing analog implementations methods

5.2 Digital demodulation method

The digital filtering self-sensing technique is implemented in hardware and the performance is evaluated using the gain and phase relation and sensitivity analysis. The analog switched capacitor filter and the

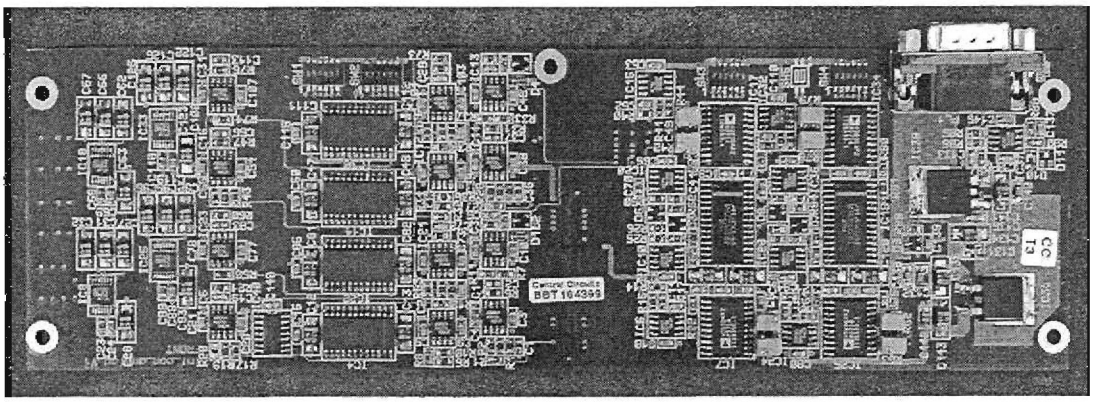

Figure 5.8: Analog electronics board

digital filter used to implement the demodulator are discussed.

5.2.1 Demodulation

The demodulation process consists of an analog BPF to remove the control current, a digital absolute function and a digital filter. The digital FIR BPF is replaced by an analog BPF due to ripple resolution. If the current was digitally filtered the control current levels should be accommodated, which means that the ripple would be only a twenty-fifth of the ADC range. The analog BPF removes this resolution problem since the fundamental component of the ripple can be scaled to the full range of the ADC. The analog BPF filter is implemented with a second order switched capacitor BPF with a pass-band of 4 kHz. The center frequency of the BPF is at the switching frequency of 20 kHz. The switch capacitor clock frequency is chosen as 1.57 MHz which is well above the 20 kHz switching component, with a third order 200 kHz anti-aliasing filter at the current and voltage sensor output as discussed in the previous chapter. The output is scaled to the maximum operating range (± 5 V) of the external ADCs with a 800 kHz sampling rate. The absolute value of the digitized signals are calculate by the FPGA, which are passed through a FIR filter. The frequency response of the least-squares FIR LPF is shown in figure 5.9. The advantage of the digital LPF is that noise generated by the power amplifier is reduced, where in the analog LPF case the noise persists even after the analog filter implementation.

5.2.2 Nonlinear model identification

The method as discussed in section 4.3 is used to identify the nonlinearities of the practical model. The top vertical axis coil was used for self-sensing. Figure 5.10 shows the nonlinear effects due to saturation of the top coil. For this analysis the current was ramped from 0.5 to 7 A. After comparing the practical and simulation results it was found that the effect of saturation was as expected. Figure 5.11 shows the compensated output. From practical measurements it

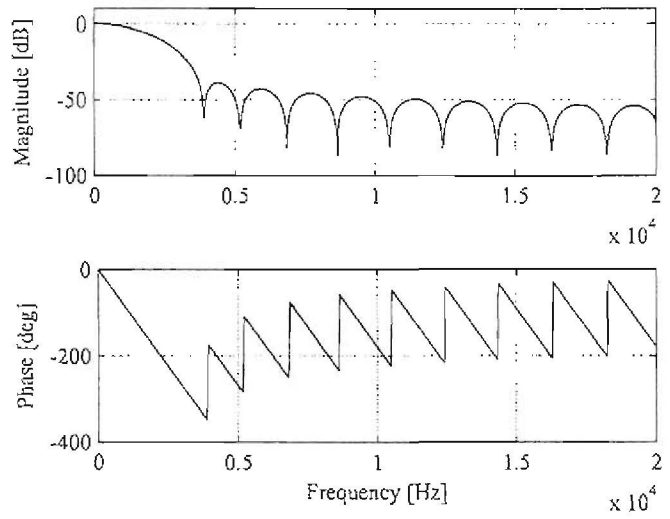

Figure 5.9: FIR filter frequency response

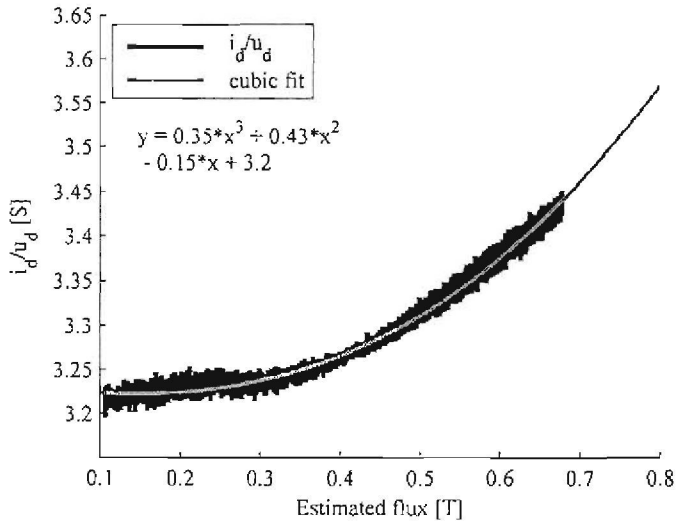

Figure 5.10: Nonlinearity due to saturation

was found that the self-sensing technique has relatively low resolution and from figure 5.11 the noise is about 2 % of the total range when the bias currents are kept constant at 3 A.

5.2.3 Static evaluation

Figure 5.12 shows the static evaluation of the self-sensing scheme which makes use of the FIR demodulation method with the bias current set to 3 A. From these results it is clear that the

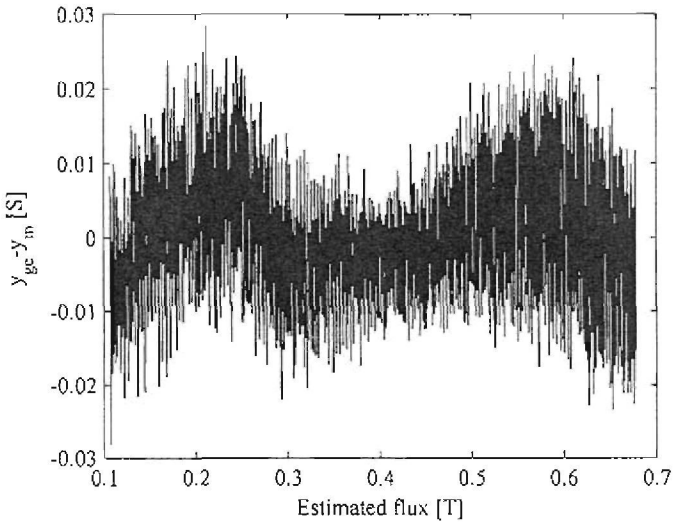

Figure 5.11: Nonlinear compensated output

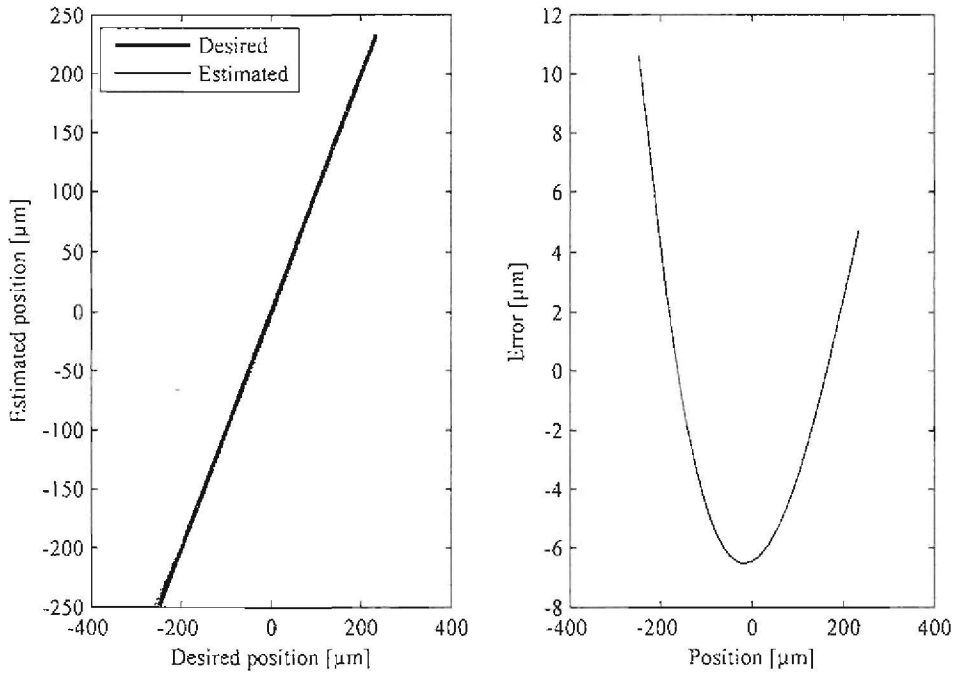

Figure 5.12: Static evaluation: Digital filtering method

system performs well in the range of 200 µm out of the total range. The self-sensing position deviates from the real position for values larger than 200 µm.

5.2.4 Controller parameters

The proportional gain of the current loop is even lower than estimated by the simulation as summarised in table 4.5. The low bandwidth of the power amplifier results in more stable self-sensing, but limits the performance of the AMB. The FIR demodulation method is evaluated with control parameters set to the values shown in table 5.2. The control parameters could not be increased since the self-sensing became unstable.

5.2.5 Dynamic evaluation

The dynamic performance is firstly evaluated by suspending the rotor with the reference set to zero. The AMB is suspended with the control loop closed with the estimated position. Figure 5.13 shows an FFT plot of the estimated and real position. From the FFT it is determined that the self-sensing excites the rigid body mode which is in the frequency range of 100 Hz. It was also found that by increasing the controller gains, the self-sensing AMB system starts to oscillate at 100 Hz. Figure 5.14 shows the gain and phase relation obtained with the controller parameters

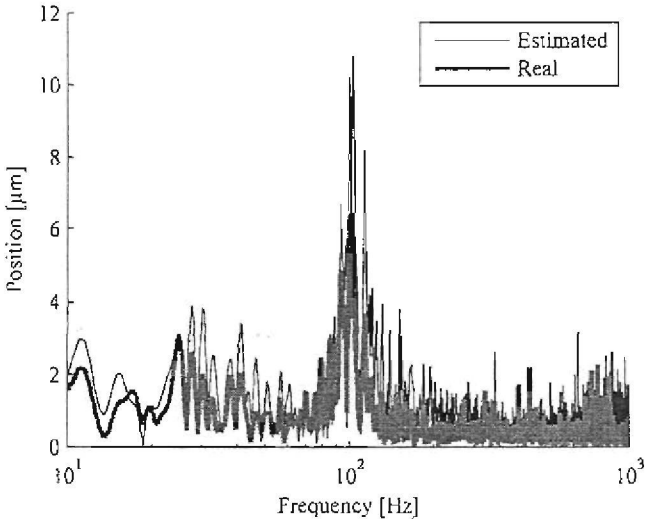

Figure 5.13: FFT of estimated position with static rotor suspension

Table 5.2: Control constants: Digital demodulation method

Constant	Value
K_p	10000
K_d	15
$K_{p_{AMP}}$	0.2

described in table 5.2. The gain starts to deviate from 0 dB at approximately 200 Hz and reaches 20 dB at 500 Hz. The phase starts to deviate from 0 degrees at 100 Hz. The phase peaks at 400 Hz. The practical gain and phase results correlate relatively well with the simulation results. Figure 5.15 shows the sensitivity of the digital demodulation method, where the peak value is

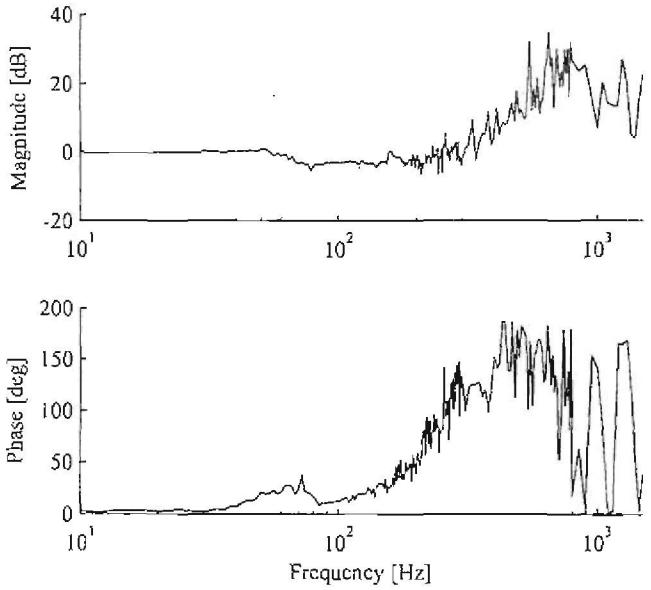

Figure 5.14: Gain and phase response: FIR demodulation method

at 16.3 dB when excited with a 9 μm peak-to-peak sinusoidal position reference. The sensitivity of the practical system is 2.6 dB higher than the simulation results. This difference can be explained by unmodelled nonlinear effects and switching noise. Since the sensitivity peaks above 14 dB, the self-sensing technique can cause severe damage to the machine [10], thus the coupled self-sensing method is not suitable for industrial applications. This method may be improved by deriving a model which includes cross-coupling effects. Such a model will make use of all the currents flowing through the coils to estimate the fluxes through the material. By estimating the fluxes the effect of cross-coupling can be estimated from each flux level.

5.3 Direct current measurement technique

The DCM self-sensing technique is implemented in hardware and evaluated using the gain and phase relation and robustness. The hardware implementation is discussed in detail where it deviates from the simulation method.

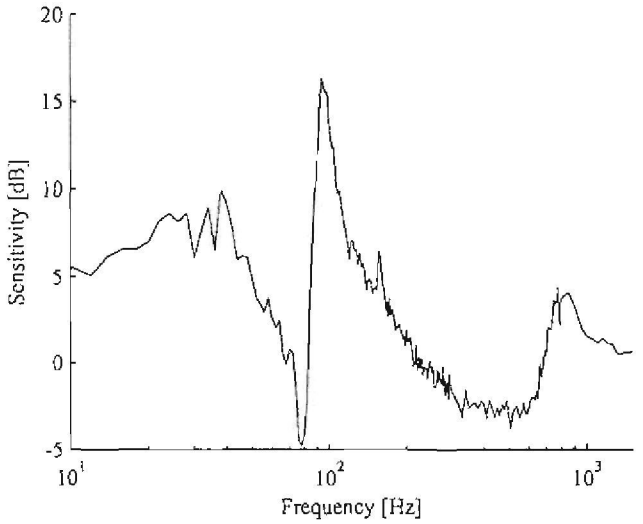

Figure 5.15: Sensitivity plot: Digital demodulation method

5.3.1 Signal conditioning

In simulation the ripple component was directly digitized and used as input to the self-sensing algorithm. The hardware was also implemented in this manner, but due to the switching noise the signal to noise ratio was very low. The low-pass filtering method as discussed in section 3.7.1 was evaluated. Due to the filter dynamics it was found not feasible. The DAC rescaling method was not included in the initial circuit design. It was not feasible to implement the DAC method due to the digital communication paths which was not available on the analog board. An analog sample and hold was implemented by piggybacking the circuit onto the analog circuit. Figure 5.16 shows the block diagram of the analog sample and hold. When the hold

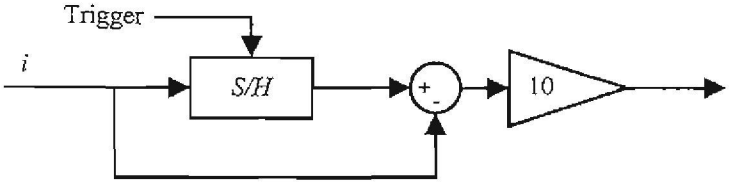

Figure 5.16: Sample and hold circuit

action is activated the control level is held and subtracted from the changing current due to the 50 % sensing cycle. The output of the differential operational amplifier is the ripple component of the coil in the 50 % sensing cycle. In the control cycle the sample action of the sample and hold is activated. In this case the sample and hold tracks the ripple and the output of the sample and hold is the same as the input. The result of the differential operational amplifier output is zero since the same signal is subtracted. The output of the differential operational amplifier is amplified to increase the resolution. The sample and hold circuit is implemented in hardware

and the amplified differential operational amplifier output is measured as shown in figure 5.17. The measurement is taken where the position is forced to the center and a bias current of 3 A

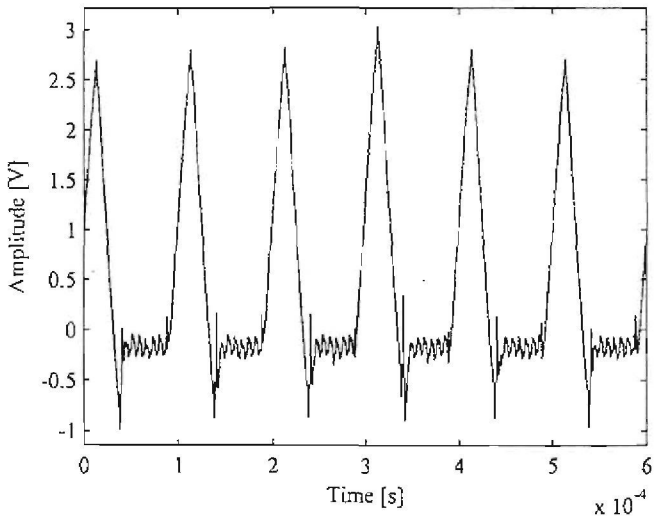

Figure 5.17: Hardware output of amplified sample and hold circuit

is applied. From the measurement the ripple component is about ten times larger than the original ripple component. This leads to a resolution increase of approximately a factor of ten due to the larger changing ripple input to the ADC.

Figure 5.18 shows the sample and hold output where the bias current is set to 3A and a 2 A, 500 Hz sinusoidal signal is added to the reference while the position is kept fixed at the center. From the top figure it is clear that some dynamics are hidden in the analog sample and hold. The 500 Hz component which can be seen in the top figure is due to a small gain error in the difference amplifier. This was determined by setting the bias current to various current levels. From this it was determined that the zero level of the difference amplifier shifted due to the current level.
In the bottom figure the output is plotted where the sinusoidal signal's gradient changes from positive to negative. From this plot it was determined that the ripple current is deformed by negative gradient components. The larger the gradient the larger the ripple deformation becomes. This was also evaluated using a lab setup with triangular signals from a signal generator to ensure this phenomenon is not dependent on the AMB model. The amplified sensing cycle is digitized using the high speed ADC. The digitized signal is passed through a low order FIR LPF which is implemented on the FPGA to reduce noise and increase stability. The FIR LPF response is the same as designed in section 4.6.6.

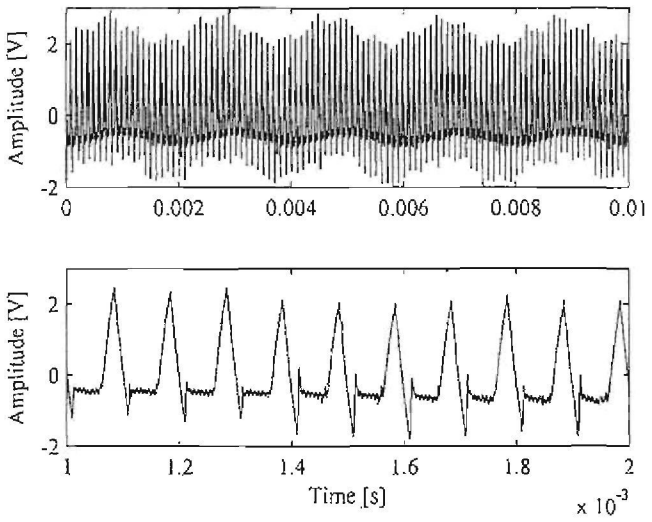

Figure 5.18: Hardware output of amplified sample and hold circuit

5.3.2 Nonlinear model identification

The same method as discussed in section 4.3 is used to identify the nonlinearities of the practical model. Figure 5.19 shows the nonlinear effects where the current is ramped from 0.5 A to 7 A. Figure 5.20 shows the unscaled nonlinear compensated position. From the figure it is clear that

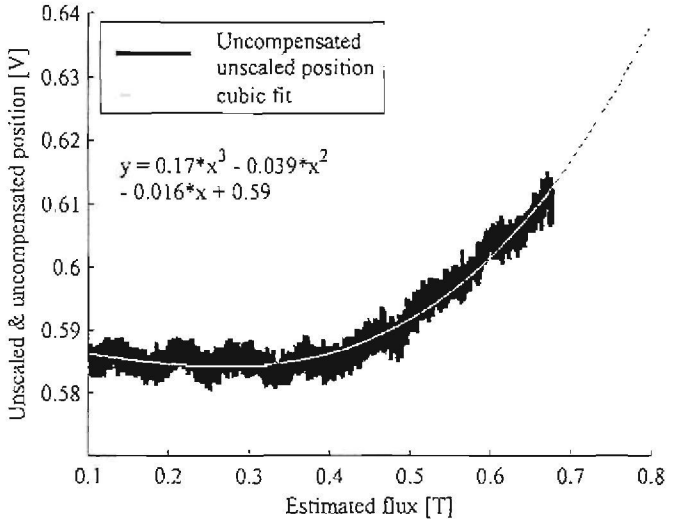

Figure 5.19: Nonlinearity due to saturation

the nonlinear compensator performs well over the range. Due to the floating point operation requirement of the compensation function, the cycle time could not be met. The compensation

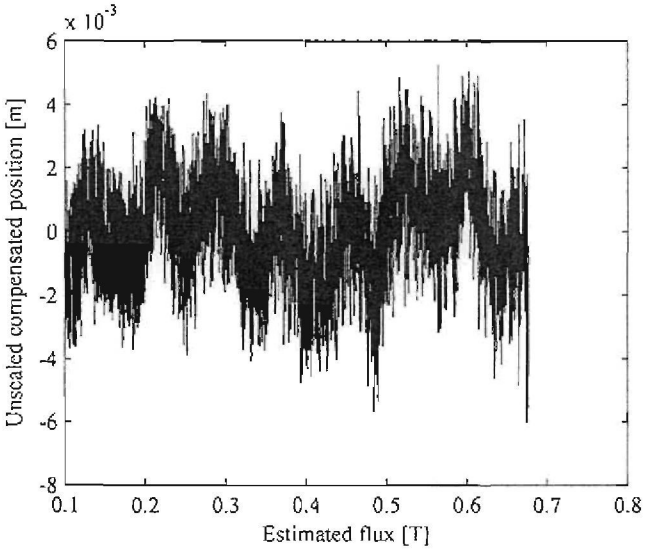

Figure 5.20: Nonlinear compensated output

function is reduced to only the bias component (0.585). It was determined that an error of approximately 1 % is made without the compensation function. The error is determined using the total self-sensing deviation of 3.616 and the total deviation of the estimation function which is approximately 0.035. The low error is due to the relatively low current operation. For self-sensing the system is operated in the range of 0 to 0.7 T and from the material data sheet it is still in the linear range. Nonlinearities start at approximately 0.6 T. The scaling is different than determined in simulation due to the fixed-point operation. The scaling constant k_x is determined to be 156.25×10^{-9} which includes all other scaling constants due to the fixed-point operation.

5.3.3 Static evaluation

Figure 5.21 shows the static evaluation of the DCM self-sensing scheme with 3 A bias current. From these results it is clear that the system performs well in the range of 200 μm out of the total range. The estimated position starts to deviate from the desired position when the position is larger than 200 μm.

5.3.4 Controller parameters

From simulation the DCM method is the only self-sensing scheme where the designed controller parameters could be used. The proportional constant of the power amplifier in the practical system was increased to twice the specified value of 0.7 and it was still stable, but the noise level increased. The self-sensing technique is evaluated with the power amplifier's bandwidth set to 2500 Hz. The DCM self-sensing technique is evaluated with two sets of controller param-

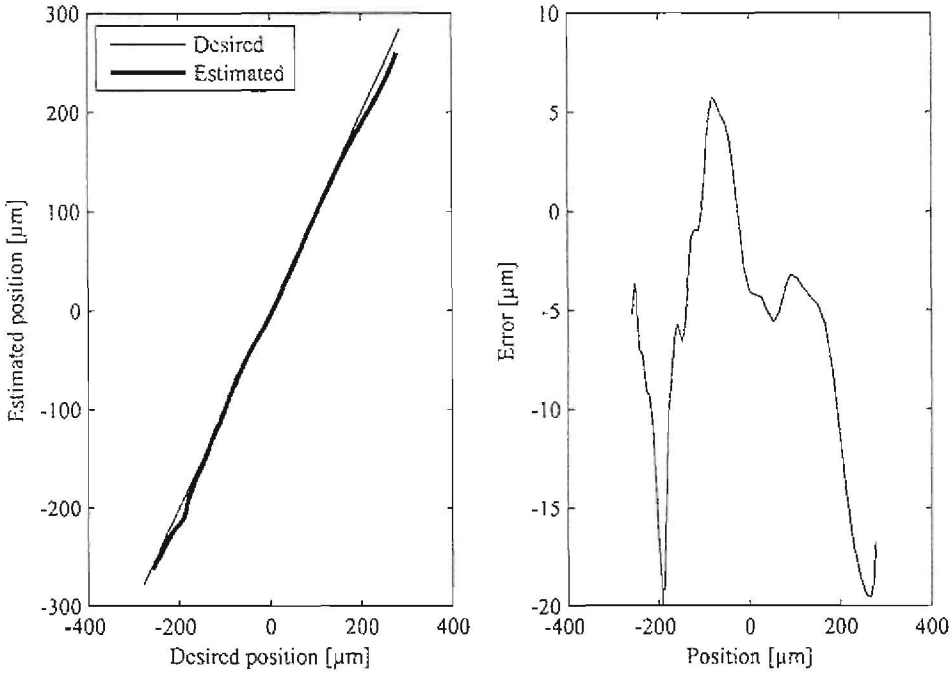

Figure 5.21: Static evaluation: DCM method

eters, which are shown in table 5.3. The filter LPF_D could not be implemented since the cycle time could not be met where the PID controller is implemented using separate proportional, integral and derivative parts. The PID controller was implemented using an integrated transfer function. Due to the integrated PID controller the whole PID input signal is filtered. The order of the filter could not be kept as low as in the simulation due to noise and oscillations. From practical measurements it was found that there is a oscillation at 720 Hz which is not due to a known rotor dynamic effect. The frequency response of the LPF was designed in such a way that the maximum attenuation is obtained at 720 Hz. The frequency response of the input PID filter is shown in figure 5.22. From the LPF frequency response it is clear that the phase of the self-sensing technique will be compromised. The filter does, however, remove the oscillation effect.

Table 5.3: Control constants: DCM method

Constant	Value	Value
K_p	10000	12000
K_d	25	25
$K_{p_{AMP}}$	0.7	0.7

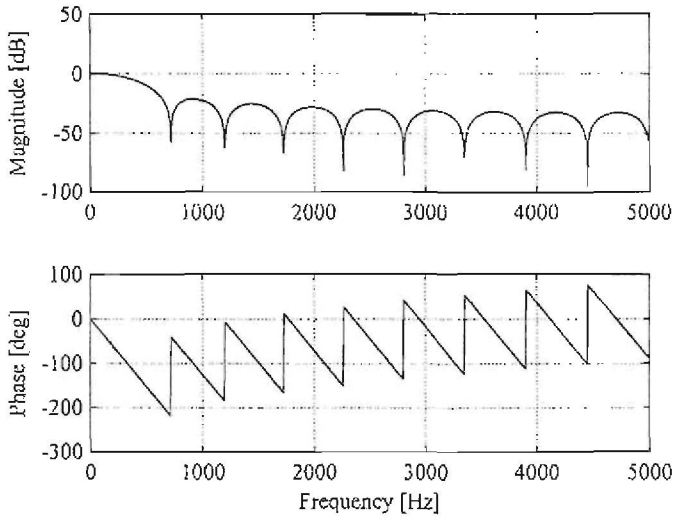

Figure 5.22: Frequency response of PID input filter

5.3.5 Dynamic evaluation

The dynamic performance is first evaluated by suspending the rotor with the reference set to zero. The AMB is suspended with the control loop closed with the estimated position. Figure 5.23 shows an FFT plot of the estimated and real position. From the FFT it is clear that there is a low frequency component present. This oscillation is at 16.5 Hz. The same result was obtained using a decoupled stator AMB system. Since the coupled and decoupled system have the same oscillation, the phenomenon is not due to the coupled AMB system.

The rotor was clamped to the center position and the same oscillation was found. From this it was determined that the ripple sensing method introduces some low frequency effects. From the same analysis it was found that the AMB is also sensitive in the range of the rigid body mode which is in the range of 100 Hz. From this it can be concluded that the self-sensing technique induces some low and high frequency components. The 16.5 Hz component is relatively independent of the control constants, where the 94 Hz component is influenced by the power amplifier and position control constants. Figure 5.24 and 5.25 show the gain and phase relation obtained where the control constants are used as described in 5.3. The gain starts to deviate from 0 dB at approximately 100 Hz and reaches 20 dB at 400 Hz. The phase starts to deviate from 0 degrees at 100 Hz. The phase peaks at 300 Hz. The practical results of the gain and phase analysis does not correlate well with the simulation results due to the high order of the PID input filter. The gain and phase analysis is repeated in simulation with the same high order PID input filter included in the control path to match the practical system. The case of $K_p = 10000$ is evaluated for the new gain and phase simulation analysis. Figure 5.26 shows the simulated response of the self-sensing system. From simulation it is determined that the order of the PID input filter resulted in large phase effects. The new simulated results are closer to the practical results. The extra phase shifts in the practical results can be due to the dynamic effect of the sample and hold.

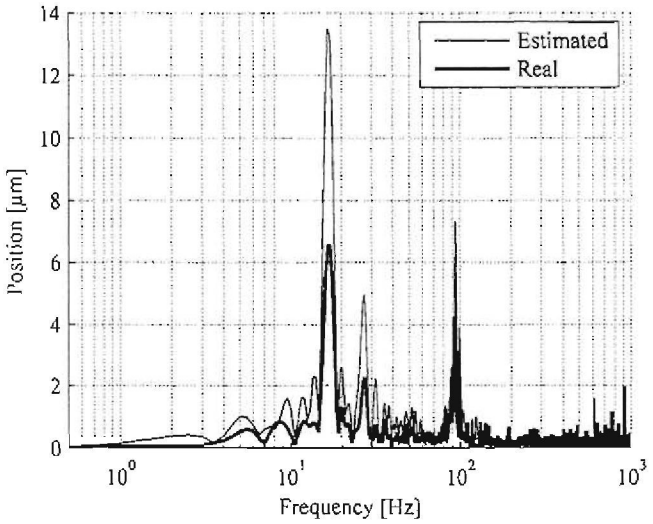

Figure 5.23: FFT of estimated position with static rotor suspension

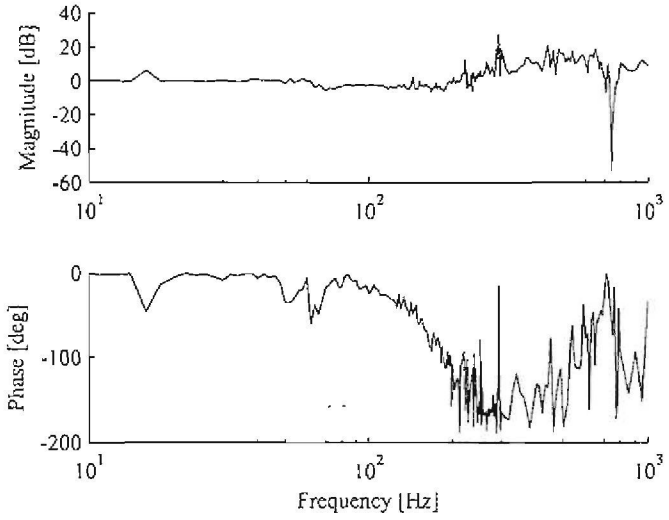

Figure 5.24: Gain and phase response: DCM method $Kp = 10000$

Figure 5.27 and 5.28 show the sensitivity of the DCM self-sensing technique. The peak value with $Kp = 10000$ is 10.3 dB excited with a 7 μm peak to peak sinusoidal position reference. The sensitivity of the practical system meets a class B system which is classified to operate unrestricted for long-term operation [10]. By altering the control constants it is found that the robustness of the self-sensing technique is affected.

The effect of the PID input filter is investigated further using an averaging filter. The order can be reduced and the system remain stable, but high frequency components affect the self-sensing

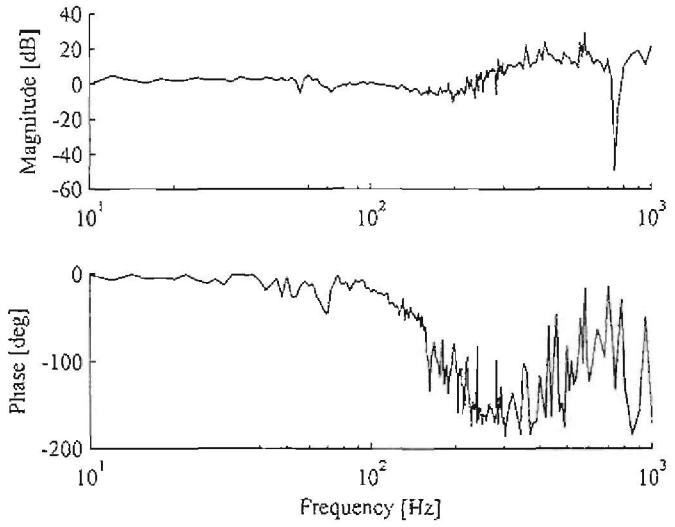

Figure 5.25: Gain and phase response: DCM method $Kp = 12000$

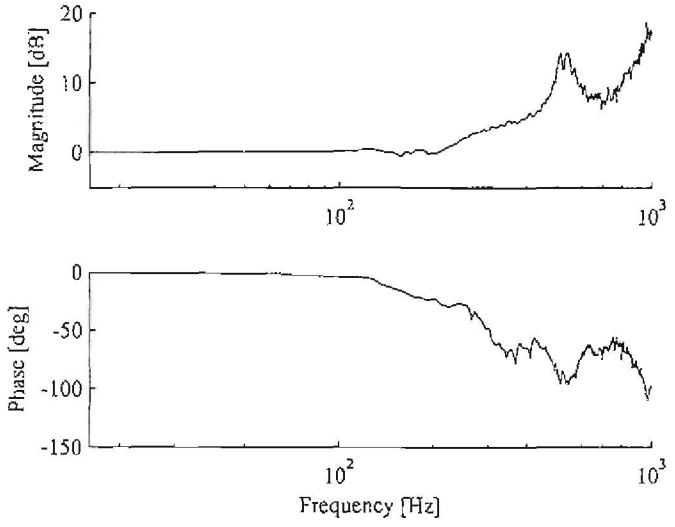

Figure 5.26: Gain and phase response: DCM method $Kp = 10000$

system. The order of the filter can be reduced to four. The phase at 500 Hz was evaluated for the filter for an order of four to seven. Each filter was evaluated and four measurements were taken to obtain a mean measurement. From these results the self-sensing has a 28 degrees phase shift and the rest of the phase shift is due to the PID input filter.

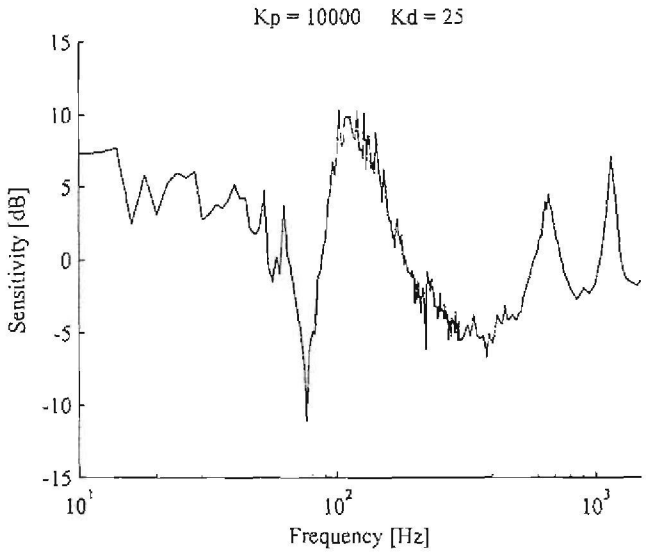

Figure 5.27: Sensitivity plot: DCM method

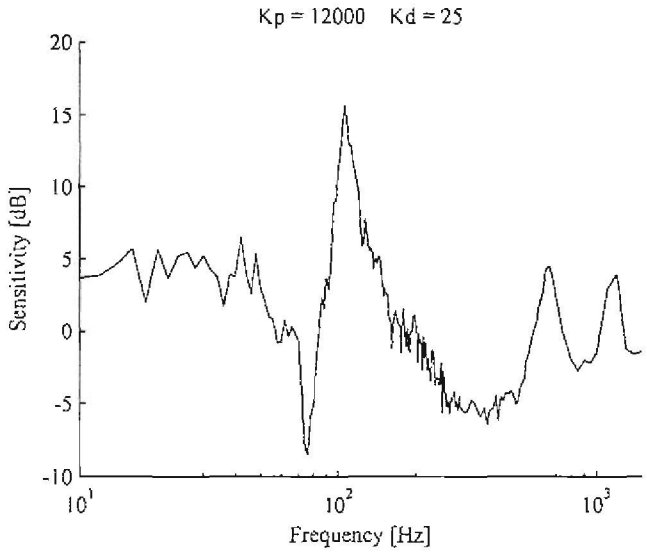

Figure 5.28: Sensitivity plot: DCM method

5.3.6 Cross-coupling

From the simulation the effect of cross-coupling on the estimated position could be reduced using the 50 % switching method of the DCM technique. The same cross-coupling measurement method as used in chapter 4 is applied to the AMB. The position of the rotor is forced to a fixed position with mechanical clamps. The 3 A bias current is applied to the top and bottom coil. A sinusoidal current reference signal is additionally applied to the top coil around the bias level. From simulation it was determined that the cross-coupling affects the self-sensing

Table 5.4: Phase effects due to filter order

Order	Phase shift due to filter	Phase shift due to closed loop system
4	72	107
5	90	121
6	108	135
7	126	147

system beyond 200 Hz, thus a 214 Hz 3 A peak to peak current reference is used. The bottom coil is used for self-sensing. Figure 5.29 shows the effect of the sinusoidal current on the position signals. The real and the estimated positions are affected by the current. The idea was that

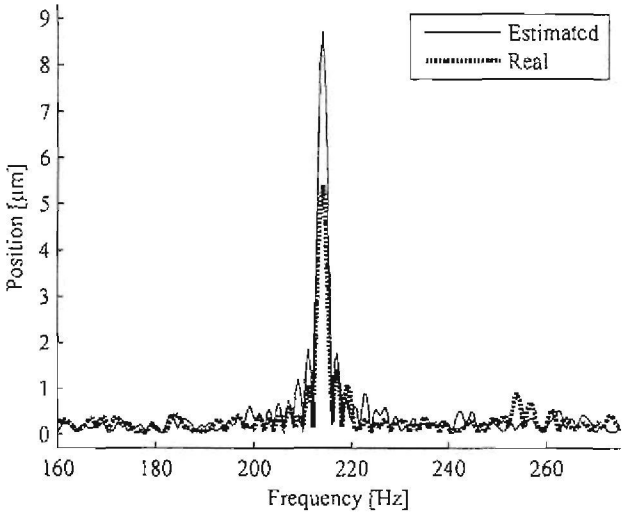

Figure 5.29: FFT of real and estimated position

the real position should not move so that the effect of cross-coupling on the estimated position could be evaluated. After investigation it was found that the real position deviates even with a 200 mA current reference when the rotor is clamped to a fixed position. Since the real position does not stay constant the measurement method is not valid.
A second measurement method was applied using the same current and sensing setup as above, but the ratio between the estimated and real position is used as measurement variable with different reference current amplitudes. Three measurements were taken at the same current level to obtain an average value. Table 5.5 shows the results in dB scale. From table 5.5 at current levels 2 and 4 amperes the conclusion is that the cross-coupling effect is the same, but the 3 A reading is substantially different. If cross-coupling has an effect the ratio should have ramped up, with the 2 A ratio reading the lowest and the 5 A reading the highest. Due to the 3 A reading the effect of cross-coupling is inconclusive.
A third method is evaluated by comparing the robustness results of a coupled and uncoupled

Table 5.5: Cross-coupling measurement

Current [A]	est/real [dB]	Real position deviation
2	12.83	3.4 μm
3	4.1	5.7 μm
4	12.62	6.3 μm

AMB system. The total AMB system constitutes two radial AMBs, thus the second AMB bearing was decoupled by cutting the laminated stator into four separate pole pairs. The four stator parts are assembled by placing splines through the laminated plates and the AMB cover body. The robustness was evaluated at the rigid body mode which is in the range of 100 Hz. The same PID input filter of which the response is shown in figure 5.22 was used. The controller constant for the decoupled method could not be kept the same as in the coupled stator case. The proportional gain K_p is set to 6000 and the derivative gain K_d was set to 12. Figure 5.30 shows the sensitivity plot of the coupled and decoupled stator. The rotor was suspended in

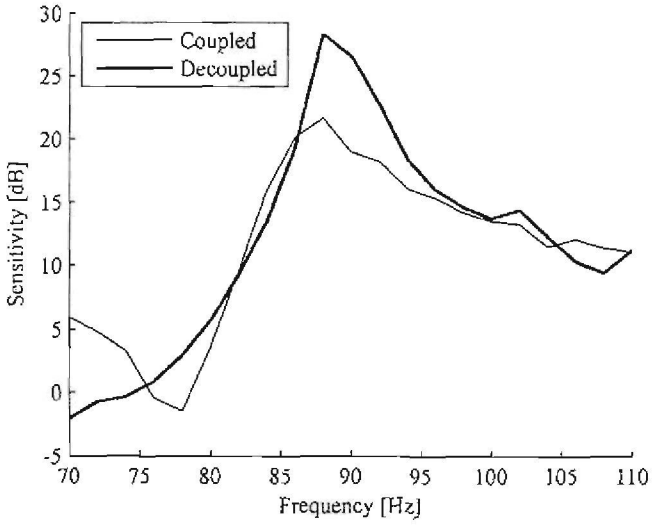

Figure 5.30: Sensitivity plot of coupled and decoupled stator

the center with a 7 μm sinusoidal position reference added. The sensitivity peaks are much higher due to the low proportional and derivative gains. The practical results contradict the theoretical results, since the coupled stator AMB performed better than the decoupled network. By using inductance measurements the decoupled AMB poles are found to be non-symmetrical, which may have an effect on the self-sensing stability. From further investigations it was found that the cutting and assembly of the poles of the uncoupled system was unsuccessful. From the three evaluation methods the effect of cross-coupling is still inconclusive. It may therefore be more feasible to evaluate the effect of cross-coupling on a smaller AMB system which exerts smaller forces on the rotor. In such a system the rotor may also be forced to a specific position

using mechanical clamps.

An interesting observation from figure 5.30 is that cross-coupling has a positive effect on the sensitivity in the range of 70-80 Hz. The self-sensing is insensitive to disturbances in this range. This is also confirmed by figures 5.27 and 5.28. The effect of cross-coupling on the peak sensitivity is inconclusive due to the decoupled AMB stability problem.

To eliminate all nonlinearities, except the duty cycle cross-coupling effect, a fourth measurement method is devised. The bottom vertical coil is switched with the 50 % sensing cycle with a 3 A bias current and it is used as the sensing coil. The top coil is supplied with a 3 A bias current with a sinusoidal current reference around the bias without the 50 % sensing cycle. The difference between this method and the previous method is that for the previous measurement method, the sinusoidal current reference is applied with the duty cycle forced to 50 % at the same time as the sensing cycle. For this measurement method, the duty cycle of the top coil will vary in the 50 % sensing cycle. By using these two measurement methods, the duty cycle cross-coupling effect can be investigated. Figures 5.31 to 5.33 show where a sinusoidal current reference is applied with a frequency of 130 Hz with different amplitudes of 2 A, 3.5 A and 5 A peak to peak respectively. In figure 5.31 and 5.32 there is little difference between the 50 % sensing cycle and without the 50 % sensing cycle. The small differences are due to small changes in duty cycle. In figure 5.33 a relative difference is identified between the estimated position with and without the 50 % sensing cycle. The estimated position measurement without the 50 % sensing cycle is smaller than in the case where the 50 % sensing cycle is used. Figure 5.34

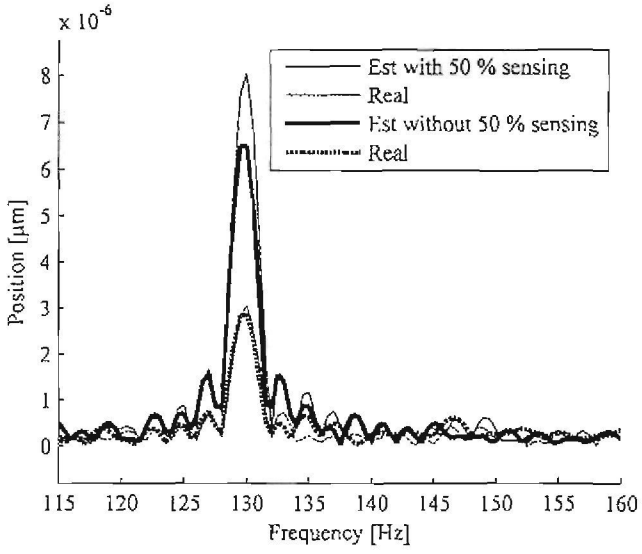

Figure 5.31: Cross-coupling due to 2 A 130 Hz current reference

shows the effect of duty cycle cross-coupling with a 5 A, 160 Hz sinusoidal reference with and without the 50 % sensing cycle. The increase of frequency has resulted in a larger duty cycle variation and the effect of duty cycle cross-coupling on the estimated position without 50 % sensing cycle is much larger. Figure 5.34 shows the effect of duty cycle cross-coupling with a 5 A, 210 Hz sinusoidal reference with and without the 50 % sensing cycle. From these results the

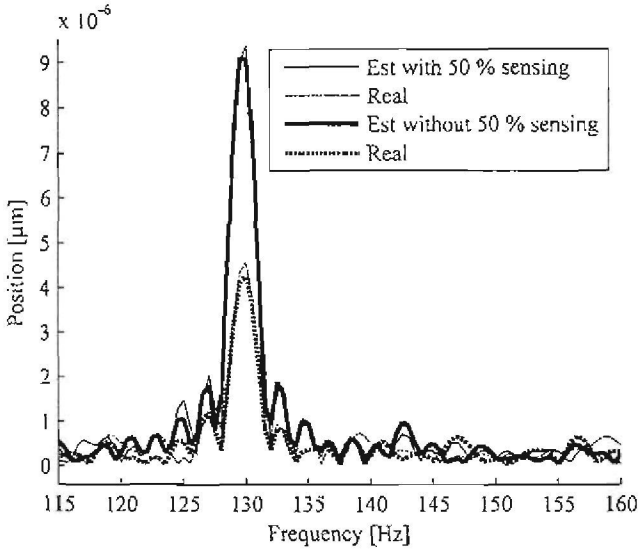

Figure 5.32: Cross-coupling due to 3.5 A 130 Hz current reference

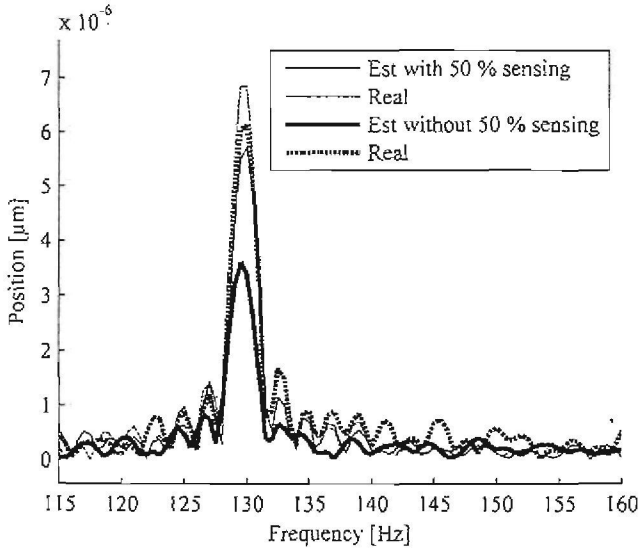

Figure 5.33: Cross-coupling due to 5 A 130 Hz current reference

improvement is less substantial as in the 160 Hz case, but there is still less cross-coupling in the 50 % sensing method. By investigating the gain and phase plot in figure 5.24 it is found that the self-sensing scheme's gain is relatively noisy after 200 Hz, thus gain measurements after 200 Hz may result in wrong cross-coupling conclusions. From the results obtained from the measurement method above it is clear that the 50 % sensing cycle results in position estimation improvements. Due to the movement of the rotor the effect of pure cross-coupling on the estimated position could not be determined, but the effect of duty cycle cross-coupling could be illustrated.

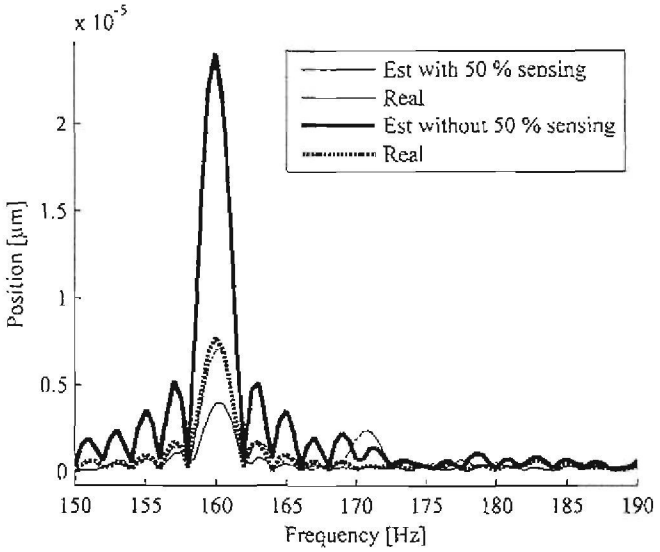

Figure 5.34: Cross-coupling due to 5 A 160 Hz current reference

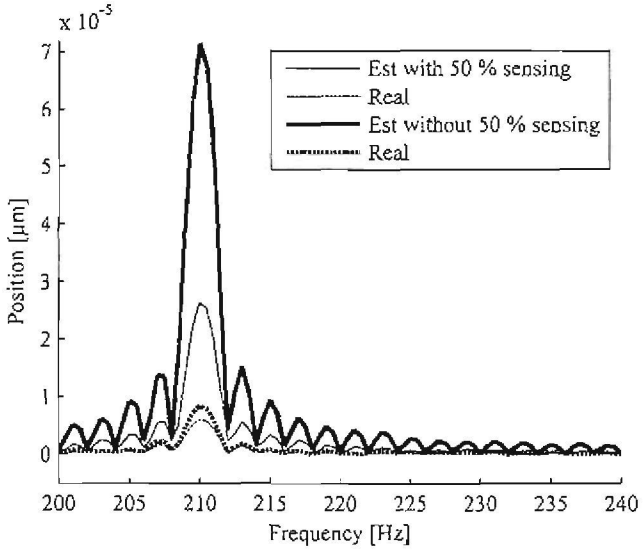

Figure 5.35: Cross-coupling due to 5 A 210 Hz current reference

---

In this chapter the hardware implementation was discussed. The power electronics-, digital- and analog boards were discussed in detail. Deviations in hardware implementation results from the simulation were discussed in detail.

The digital demodulation method was implemented and the practical results correlated well with the simulation results. The sensitivity of the self-sensing system was found to be too high for any industrial

application.

The analog, band-pass sampling, and BPF FFT self-sensing techniques were implemented on hardware. Only the BPF FFT technique was relatively stable, but not stable enough for any performance measurements. The rest of the techniques were found to be totally unstable. The interesting observation from these results was that the methods which have some form of filtering inside the FPGA were stable. From this, the conclusion can be made that noise has an enormous effect on the stability of the self-sensing techniques. In the case of the self-sensing techniques which make use of some form of FPGA filtering, the sinal to noise level is improved. Thus after the digital filtering no noise can couple onto the filtered signals.

The DCM self-sensing technique was implemented and the practical results did not correlate that well with the simulation results. The difference between the simulation and the practical implementation was due to the high order PID input filter as well as the dynamic effects due to the sample and hold. The filter was included in the simulation and the gain and phase again showed that filters have a large effect on the overall self-sensing bandwidth. The robustness of the self-sensing system was found to be in the mid range of a class B system, which means that the DCM self-sensing technique is usable in industry. The DCM self-sensing technique also has the advantage that only the current signals are necessary for position estimation.

The effect of cross-coupling was evaluated and it was found that it is relatively difficult to practically measure the effect on the estimated position. The effect of duty cycle cross-coupling could be illustrated and the 50 % sensing technique was shown to be less sensitive. From the sensitivity analysis it was found that the DCM method performed well. This increase in robustness could be directly linked to reduced cross-coupling.

Chapter 6

Conclusions and recommendations

6.1 Summary

The goal of this thesis was to evaluate existing self-sensing schemes, devise improvements and investigate possible new self-sensing schemes aimed at industrialization. The amplitude modulation self-sensing technique which makes use of the power amplifier current ripple was identified as the technique which has the most possibilities for further improvements in the self-sensing research field.

The different self-sensing schemes were implemented in simulation and performance measurements were obtained with cross-coupling included. From these results it was determined that certain components in the self-sensing schemes lead to large phase effects, which resulted in low robustness. A phase criterion was used to reduce or eliminate the phase effects as far as possible. The best robustness results were obtained from the self-sensing technique which had the lowest phase shifts in simulation.

The practical implementation feasibility of the self-sensing schemes were determined through the simulations. The gradient self-sensing scheme was eliminated due to the gradient sensitivity. It was found that the smallest amount of filtering largely affects the gradient. Due to noise in the practical system, filters could not be eliminated, thus it would be difficult to implement the gradient technique. All the other self-sensing schemes were evaluated in hardware and it was found that switching noise had a large effect on the stability of the self-sensing schemes. The self-sensing schemes which made use of FIR filters implemented on the FPGA were observed to be stable. The conclusion was made that switching noise coupled into all the signals even after analog filtering.

The two practical methods which were stable and from which performance measurements were obtained are the digitally filtered demodulation method and the DCM self-sensing method. The digitally filtered technique's sensitivity peaked at 14 dB which is too high for any application. The DCM self-sensing technique's sensitivity peak is however low enough (10.3 dB) for use in most AMB applications with low to medium rotational speeds.

The effect of cross-coupling was investigated by using a simplified reluctance network. From the analysis it was found that the current ripple component which is used for self-sensing was affected by the change in duty cycle. By using the 50 % PWM switching method the effect of cross-coupling was reduced .

6.2 Unique contributions

The original contributions of this work is listed from prominent to less prominent.

DCM self-sensing scheme is a new proposed self-sensing scheme. This method lends itself to the use of only the current ripple to estimate the rotor position. The 50 % PWM switching technique used in the DCM self-sensing technique reduces the nonlinear effects due to duty cycle variations. This method reduces component count and thus increases system robustness. The 50 % switching method also makes the DCM self-sensing technique less sensitive for cross-coupling effects. With the 50 % switching method the resolution can be increased to the maximum range of the ADC without using a BPF to extract the ripple component. By eliminating the BPF the resolution is increased without affecting the frequency contents. This method lends itself to low to mid frequency applications, since the bandwidth is approximately 200 Hz. From the sensitivity results, the sensitivity of the DCM self-sensing scheme is low enough (10.3 dB) for long-term operation according to the ISO 14839-3 standard.

A **comparative study** was done on the different self-sensing schemes. From the comparative study it was determined that the gain- and phase effects have a direct effect on the sensitivity of the self-sensing system. The lower the gain and phase deviation from zero dB and zero degrees respectively, the less sensitive the self-sensing schemes become. Two demodulation variations of the FFT demodulation method were implemented and the phase effects due to the demodulation process could be illustrated. From these two variations it was proved that the BPF used in the demodulation path increases the sensitivity.

The **practical implementation** of the self-sensing schemes can also be seen as a contribution, since with the practical implementation it was proved that self-sensing is a step closer to an integrated industrial system. The practical implementation proved also that the DCM self-sensing scheme and the digital demodulation method are practically implementable on a high current AMB system (0 to 10 A). It was also proved that self-sensing can be implemented on a coupled AMB system which include cross-coupling. Since a coupled stator is used the manufacturing cost can be reduced. The high current and coupled AMB system is also a step closer to an industrialized self-sensing system.
The current sensors used in hardware is off-the-shelf current sensors, which eliminates the development of bulky in-house sensing methods.
From the practical implementation it was also learnt that extreme care must be taken to reduce noise. Where possible, the signals must be digitized by using high speed ADCs and the signals must be digitally filtered to eliminate noise effects.

6.3 Future work

There is still a large amount of work to be done on self-sensing to make it robust for widespread industrial applications. All the self-sensing models are dependent on the magnetic material used and mechanical layout of the AMB system. This part will focus on future work identified from this research alone.

- The analog sample and hold scaling method used in the DCM self-sensing scheme must be replaced by the DAC method. This will eliminate the dynamics due to the negative gradient. If the analog sample and hold dynamics have such a large effect as suspected, the robustness may be increased by the DAC method. This may enable the self-sensing AMB system to operate at its designed control constants and stiffness in the practical system.
- The effect of cross-coupling on self-sensing techniques may be investigated. A compensation model may be derived which makes use of all the currents and position signals to estimate the position error due to cross-coupling more accurately.
- The stability robustness of self-sensing for parametric uncertainty in the controller and/or the plant should be investigated. This may explain why the stiffness in most self-sensing cases must be reduced to obtain stability.
- The calibration of a self-sensing system without the use of conventional position sensors. One advantage of self-sensing is that the rotor length can be reduced due to the elimination of sensing areas of conventional sensors. Currently, conventional sensors are still used to calibrate the self-sensing technique, thus sensing areas are not eliminated.
- The effect of saturation can be reduced by implementing a differential amplitude modulation self-sensing method which makes use of a current weighting function as used by Ranft [1]. Such a method will sense the position from the coil which has the smallest current flowing through the coil.

6.4 Closure

The aim of this thesis was to improve existing amplitude demodulation methods for the amplitude modulation self-sensing scheme. Two new self-sensing techniques were also introduced, which make use of only the current ripple. The effect of cross-coupling was included in the analysis. A comparative study of the simulation results of the different self-sensing schemes was done. The digital demodulation method and the DCM self-sensing scheme were implemented and practically evaluated.

In chapter 3 the different self-sensing schemes were discussed and some possible practical implications were identified. In chapter 4 the different demodulation methods were evaluated in simulation and it was found that the phase effect of the demodulation process affects the robustness of the self-sensing system. The DCM self-sensing scheme outperformed the rest of

the schemes in simulation. It was also found that the switching method of the power amplifiers in the DCM self-sensing scheme reduced the effect of cross-coupling.

In chapter 5 the digital demodulation method and the DCM self-sensing schemes were successfully implemented in hardware. The schemes were implemented on a radial bearing which suspended the vertical axis. The power amplifiers are rated at 7 A rms which makes it a relatively high current system for self-sensing, which is a step closer to an industrial application. It was found that switching noise have an enormous effect on the self-sensing schemes. The DCM method which performed extremely well in simulation also performed relatively well in practice. By reducing the stiffness of the AMB system the sensitivity was determined as a class B system. A class B system is acceptable of unrestricted long-term operation, which is adequate for most AMB systems.

An overall analytic model which includes all dynamics such as the power amplifier and material properties, will be useful to determine the maximum stiffness for a specific sensitivity. Such an analytic model will also give a better theoretical understanding of the operation of the self-sensing AMB system. There is still much room for improvement and self-sensing remains a challenging field.

Bibliography

[1] E. O. Ranft, "An improved model for self-sensing heteropolar active magnetic bearings," Ph.D. dissertation, North West University, Dec 2007.

[2] G. Schweitzer, H. Bleuler, and A. Traxler, *Active magnetic bearings: Basics, Properties and Applications of Active magnetic bearings*. Zurich: Authors Working Group, 1993.

[3] J. Boehm, R. Gerber, and N. Kiley, "Sensors for magnetic bearings," *IEEE Trancation on Magnetics*, vol. 29, p. 2962 2964, 1993.

[4] M. Brunet and B. Wagner, "Inovation: Self-sensing technology, simplified mechanical design," *In S2M News*, vol. number 5, 2005.

[5] A. Schammass, "A self-sensing active magnetic bearing: Modulation approach," Ph.D. dissertation, July 2003.

[6] N. Morse, R. Smith, B. Paden, and J. Antaki, "Position sensed and self-sensing magnetic bearing configurations and associated robustness limitations," in *Proceedings of the 37th IEEE Conference on Decision and Control*, Tampa, Florida USA, Dec 1998, pp. 2599 – 2604.

[7] E. Maslen, T. Iwasaki, and R. Mahmoodian, "Formal parameter estimation for self-sensing," in *Proceedings of the 10th International Symposium on Magnetic Bearings*, Martigny, Switzerland, Aug. 2006.

[8] A. Schammass, R. Herzog, and P. Bühler, "New results for self-sensing active magnetic bearings using modulation approach," *IEEE Transaction on Control Systems Technology*, vol. 13, pp. 509 – 516, 2005.

[9] L. Li, T. Shinshi, and A. Shimokohbe, "State feedback control for active magnetic bearings based on current change rate alone," *IEEE Transaction on Magnetics*, vol. 40, pp. 3512 – 3516, 2004.

[10] I. TC108/SC2/WG7, "Mechanical vibration: Vibration of rotating machinery equipped with active magnetic bearings, part 3: Evaluating of stability margin," *ISO standard, ISO 14839-3*, 2004.

[11] E. Maslen, "State-of-the-art and future directions for amb control and applications," in *Proceedings of the Sixth International Symposium on Magnetic Suspension Technology*, Turin, Italy, Oct 2001.

[12] A. Peijnenburg, J. Vermeulen, and J. van Eijk, "Magnetic levitation systems compared to conventional bearing systems," *MicroElectronic Egineering*, vol. 38, p. 1372 1375, 2006.

[13] C. Knospe, "Active magnetic bearings for machining applications," *Control Egineering Practice*, vol. 15, p. 307 313, 2005.

[14] M. Komori and C. Shiraishi, "Superconducting bearings assisted by self-sensing ambs in liquid nitrogen," *JSME International Journal*, vol. 46, pp. 397 – 402, 2003.

[15] P. Tsao, S. Sanders, and G. Risk, "A self-sensing homopolar magnetic bearing: Analysis and experimental results," in *Proceedings of the 1999 IEEE Industry Applications Conference - 34th IAS Annual Meeting*, 1999, pp. 2560–2565.

[16] N. Skricka and R. Market, "Improvements of the integration of active magnetic bearings," *Mechatronics*, vol. 12, pp. 1059 – 1068, 2002.

[17] M. Mirishita and H. Ito, "The self-gap-detecting electromagnetic suspension system with robust stability against variation of levitation mass," Taorima, Italy, May 2006.

[18] C. Choi and K. Park, "Self-sensing magnetic levitation using a lc resonant circuit," *Sensors and Actuators*, vol. A72, pp. 169 – 177, 1999.

[19] D. Vischer and H. Bleuler, "Self-sensing active magnetic levitation," *IEEE Trancation on Magnetics*, vol. 2, pp. 1276 – 1281, 1993.

[20] T. Mizuno and H. Bleuler, "Self-sensing magnetic bearing control systems design using the geometric approach," *Control Engineering Practice*, vol. 3, pp. 925 – 932, 1995.

[21] M. Sasaki, Y. Kobayashi, Y. Hori, and F. Fujisawa, "Active electromagnetic levitation control of a flexible beam by using disturbance observer," *International Journal of Applied Electromagnetics and Mechanics*, vol. 18, pp. 81 – 92, 2003.

[22] L. Kucera, "Robustness of self-sensing magnetic bearings," in *Proceedings of the MAG97*, Alexandria,VA, USA, 1997.

[23] E. Maslen, "Self-sensing for active magnetic bearings: overview and status," in *ISMB10*.

[24] T. Mizuno, T. Ishii, and K. Araki, "Self-sensing magnetic suspention using hysteresis amplifiers," *Control Engineering Practice*, vol. 6, pp. 1133 – 1140, 1998.

[25] A. Carlson, P. Crilly, and J. Rutledge, *Comunication Systems*. New York: McGraw-Hill, 2002.

[26] J. Yim, J. Kim, S. Sul, H. Ahn, and D. Han, "Sensorless position control of active magnetic bearings based on high frequency signal injection method," in *Proceedings of the Applied Power Electronics Conference and Exposition*, California, 2004, pp. 1351 – 1354.

[27] K. Sivadasan, "Analysis of self-sensing active magnetic bearings working on inductance measurements principle," *IEEE Transaction on Magnetics*, vol. 32, p. 329 334, 1996.

[28] M. Noh, "Self-sensing magnetic bearings driven by a switching power amplifier," Ph.D. dissertation, University of Virginia, January 1996.

[29] M. Noh and E. Maslen, "Self-sensing magnetic bearings using parameter estimation," *IEEE Transaction on Instrumentation and Measurement*, vol. 46, pp. 45–50, 1997.

[30] D. Montie, "Performance limitations and self-sensing magnetic bearings," Ph.D. dissertation, University of Virginia, January 2003.

[31] E. Maslen, D. Montie, and T. Iwasaki, "Robustness limitations in self-sensing magnetic bearings," *ASME, Dynamic Systems, Measurement, and Control*, vol. 128, pp. 197 – 203, 2006.

[32] Y. Toshiya, K. Yoshiyuki, O. Katsumi, and M. Osamu, "Self-sensing active magnetic bearings using a new pwm amplifier equipped with a bias voltage source," in *Proceedings of the 10th European Confrence on Power Electronics and Applications*, Toulouse, France, Sep 2003.

[33] M. Noh and E. Maslen, "Self-sensing magnetic bearings (part I)," in *Proceedings of the 5th International Symposium on Magnetic Bearings*, Kanazawa, Japan, Aug 1996, p. 95 100.

[34] ——, "Self-sensing magnetic bearings (part II)," in *Proceedings of the 5th International Symposium on Magnetic Bearings*, Kanazawa, Japan, Aug 1996, pp. 113 – 118.

[35] V. Iannello, "Sensorless position for an active magnetic bearing," US Patent 5 696 412, 1997.

[36] H. Dommel, "On modelling iron ore nonlinearities," *IEEE Transactions on Power Systems*, vol. 8, no 2, pp. 417–425, 1993.

[37] N. Skrika and R. Markert, "Influence of cross-axis sensitivity and coordinate coupling on self-sensing," in *Proceedings of the Sixth International Symposium on Magnetic Suspention Technology*, Turin, Italy, Oct 2001, pp. 179–184.

[38] B. Polajžer, "Design and analysis of an active magnetic bearing experimental system," Ph.D. dissertation, February 2003.

[39] B. Polajžer, G. Štumberger, J. Ritonja, D. Dolinar, O. Tezak, and K. Hameyer, "Impact of magnetic nonlinearities and cross coupling effects on properties of radial active magnetic bearings," *IEEE Transactions on Magnetics*, vol. 40, no2, pp. 798–801, 2004.

[40] M.Antila, "Electromechanical properties of radial active magnetic bearings," Ph.D. dissertation, Helsinki University of Technology, November 1998.

[41] E. Maslen, T. Iwasaki, and R. Mahmoodian, "Selfsensing magnetic bearings: development of a virtual probe," in *Proceedings of 2006 NSF Design, Service, and Manufacturing Grantees and Research Conference*, vol. 46, St. Louis, Missouri, 2006, pp. 179–184.

[42] D. Meeker, E. Maslen, and M. Noh, "An augmented circuit model for magnetic bearings including eddy currents, fringing, and leakage,," *IEEE Transactions on Magnetics*, vol. 32, no4, pp. 3219–3227, 1996.

[43] D. Jiles and D. Atherton, "Theory of ferromagnetic hysteresis," *Journal of Magnetism and Magnetic Materials*, vol. 61, no 1, pp. 48–60, 1986.

[44] H. Brachtendorf and R. Laur, "Modeling of hysteresis in magnetic cores with frequency-dependant losses," *Journal of Magnetism and Magnetic Materials*, vol. 183, pp. 305–312, 1998.

[45] G. Bertotti, *Hysteresis in Magnetism.* New York: Academic Press, 1998.

[46] E. Ifeachor and W. J. B, *Digital Signal Processing, Second Edition.* New York: Prentice Hall, 2002.

[47] F. Giordano, M. Weir, and W. Fox, *A First Course in Mathematical Modeling, Second Edition.* New York: Brooks/Cole, 1997.

[48] B. Hu and A. Micheal, "Robustness analysis of digital feedback control systems with time-varying sample periods," *Journal of The Franklin Institute*, vol. 337, pp. 117–130, 2000.

[49] M. Noh, D. Montie, and E. Maslen, "A simulation model for the analysis of transient magnetic bearing performance," in *Proceedings of the seventh International Symposuim on Magnetic bearings*, ETH Zurich, Switzerland, Aug 2000, pp. 177–181.

Appendix A

Cross-coupling

Figure A.1 shows a reluctance network of an eight pole radial magnetic bearing with a NSSNNSSN configuration.

For this analysis the magnetic material is assumed to be linear and fringing effects are neglected. Due to the linearity assumption and the symmetrical properties of a radial bearing, the reluctances of the network can be reduced to three material reluctances and four air gap reluctances. Since the magnetic circuit is equivalent to an electric circuit the mesh-current method

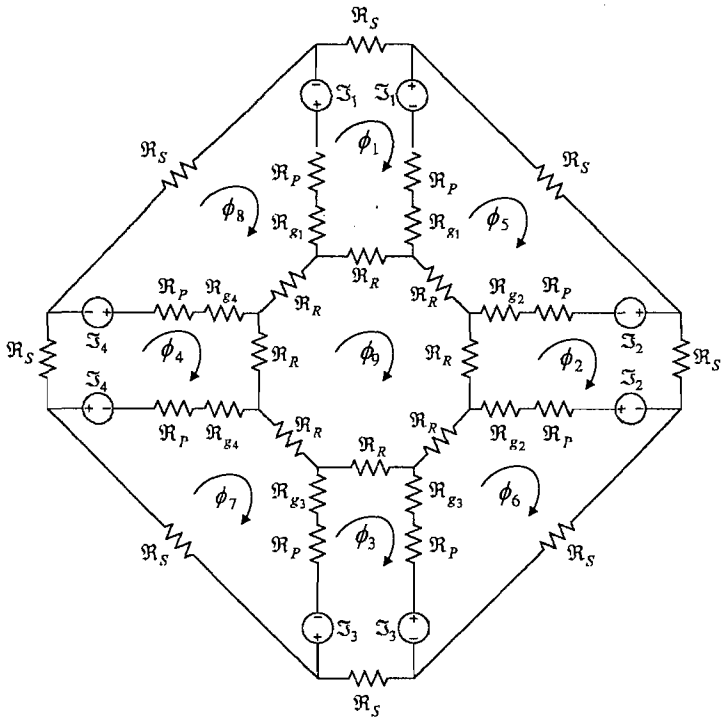

Figure A.1: Reluctance network

can be used to solve the network. Nine flux paths are identified and by applying Kirchhoff's voltage law around the nine meshes, nine equations are obtained as shown in (A.1).

$$
\begin{aligned}
&\phi_1(t)\left(\Re_s + 2\Re_{g_1}(t) + 2\Re_P + \Re_R\right) - \phi_5(t)\left(\Re_{g_1}(t) + \Re_P\right) - \phi_8(t)\left(\Re_{g_1}(t) + \Re_P\right)\\
&-\phi_9(t)\Re_R = -2\Im_1(t)\\
&\\
&-\phi_1(t)\left(\Re_{g_1}(t) + \Re_P\right) + \phi_5(t)\left(\Re_s + \Re_{g_1}(t) + \Re_{g_2}(t) + 2\Re_P + \Re_R\right)\\
&-\phi_2(t)\left(\Re_{g_2}(t) + \Re_P\right) - \phi_9(t)\Re_R = \Im_1(t) - \Im_2(t)\\
&\\
&-\phi_5(t)\left(\Re_{g_2}(t) + \Re_P\right) + \phi_2(t)\left(\Re_s + 2\Re_{g_2}(t) + 2\Re_P + \Re_R\right) - \phi_6(t)\left(\Re_{g_2}(t) + \Re_P\right)\\
&-\phi_9(t)\Re_R = 2\Im_2(t)\\
&\\
&-\phi_2(t)\left(\Re_{g_2}(t) + \Re_P\right) + \phi_6(t)\left(\Re_s + \Re_{g_3}(t) + \Re_{g_2}(t) + 2\Re_P + \Re_R\right)\\
&-\phi_3(t)\left(\Re_{g_3}(t) + \Re_P\right) - \phi_9(t)\Re_R = -\Im_2(t) + \Im_3(t)\\
&\\
&-\phi_6(t)\left(\Re_{g_3}(t) + \Re_P\right) + \phi_3(t)\left(\Re_s + 2\Re_{g_3}(t) + 2\Re_P + \Re_R\right) - \phi_7(t)\left(\Re_{g_3}(t) + \Re_P\right)\\
&-\phi_9(t)\Re_R = -2\Im_3(t)\\
&\\
&-\phi_3(t)\left(\Re_{g_3}(t) + \Re_P\right) + \phi_7(t)\left(\Re_s + \Re_{g_3}(t) + \Re_{g_4}(t) + 2\Re_P + \Re_R\right)\\
&-\phi_4(t)\left(\Re_{g_4}(t) + \Re_P\right) - \phi_9(t)\Re_R = \Im_3(t) - \Im_4(t)\\
&\\
&-\phi_7(t)\left(\Re_{g_4}(t) + \Re_P\right) + \phi_4(t)\left(\Re_s + 2\Re_{g_4}(t) + 2\Re_P + \Re_R\right) - \phi_8(t)\left(\Re_{g_4}(t) + \Re_P\right)\\
&-\phi_9(t)\Re_R = 2\Im_4(t)\\
&\\
&-\phi_4(t)(\Re_{g_4}(t) + \Re_P) + \phi_8(t)(\Re_s + \Re_{g_1}(t) + \Re_{g_4}(t) + 2\Re_P + \Re_R)\\
&-\phi_1(t)(\Re_{g_1}(t) + \Re_P) - \phi_9(t)\Re_R = \Im_1(t) - \Im_4(t)\\
&\\
&-\phi_1(t)(\Re_R) - \phi_2(t)(\Re_R) - \phi_3(t)(\Re_R) - \phi_4(t)(\Re_R) - \phi_5(t)(\Re_R) - \phi_6(t)(\Re_R)\\
&-\phi_7(t)(\Re_R) - \phi_8(t)(\Re_R) + \phi_9(t)(8\Re_R) = 0
\end{aligned}
\tag{A.1}
$$

The reluctance of the magnetic material paths are determined by (A.2),

$$\Re_S = \frac{l_s}{\mu_0\mu_r A_S}, \quad \Re_P = \frac{l_s}{\mu_0\mu_r A_P}, \quad \Re_R = \frac{l_s}{\mu_0\mu_r A_R} \tag{A.2}$$

where l_S, l_P and l_R are the magnetic material path lengths, A_S, A_P and A_R are the cross-sectional areas of the material, μ_r is assumed to be constant and $\Im_m(t)$ is the mmf and $m = 1,2,3,4$.

The reluctances of the air gaps are determined by (A.3),

$$\Re_{g_1}(t) = \frac{g_0+y(t)}{\mu_0 A_P}, \quad \Re_{g_3}(t) = \frac{g_0-y(t)}{\mu_0 A_P}, \quad \Re_{g_2}(t) = \frac{g_0+x(t)}{\mu_0 A_P}, \quad \Re_{g_4}(t) = \frac{g_0-x(t)}{\mu_0 A_P} \tag{A.3}$$

where g_0 is the air gap at center position and $x(t)$ and $y(t)$ are the change in position over time.

Equation (A.4) shows the nine equations written in matrix form. All components are time dependent (t), but is not shown in order to save space. By using the MATLAB® symbolic

toolbox the flux in each path can be determined by taking the inverse of the reluctance network and multiplying it with the *mmf* matrix,

$$\begin{bmatrix} \Re_{(1,1)} & \Re_{(1,2)} & 0 & 0 & 0 & 0 & 0 & \Re_{(1,8)} & \Re_{(1,9)} \\ \Re_{(2,1)} & \Re_{(2,2)} & \Re_{(2,3)} & 0 & 0 & 0 & 0 & 0 & \Re_{(2,9)} \\ 0 & \Re_{(3,2)} & \Re_{(3,3)} & \Re_{(3,4)} & 0 & 0 & 0 & 0 & \Re_{(3,9)} \\ 0 & 0 & \Re_{(4,3)} & \Re_{(4,4)} & \Re_{(4,5)} & 0 & 0 & 0 & \Re_{(4,9)} \\ 0 & 0 & 0 & \Re_{(5,4)} & \Re_{(5,5)} & \Re_{(5,6)} & 0 & 0 & \Re_{(5,9)} \\ 0 & 0 & 0 & 0 & \Re_{(6,5)} & \Re_{(6,6)} & \Re_{(6,7)} & 0 & \Re_{(6,9)} \\ 0 & 0 & 0 & 0 & 0 & \Re_{(7,6)} & \Re_{(7,7)} & \Re_{(7,8)} & \Re_{(7,9)} \\ \Re_{(8,1)} & 0 & 0 & 0 & 0 & 0 & \Re_{(8,7)} & \Re_{(8,8)} & \Re_{(8,9)} \\ \Re_{(9,1)} & \Re_{(9,2)} & \Re_{(9,3)} & \Re_{(9,4)} & \Re_{(9,5)} & \Re_{(9,6)} & \Re_{(9,7)} & \Re_{(9,8)} & \Re_{(9,9)} \end{bmatrix} \begin{bmatrix} \phi_1 \\ \phi_5 \\ \phi_2 \\ \phi_6 \\ \phi_3 \\ \phi_7 \\ \phi_4 \\ \phi_8 \\ \phi_9 \end{bmatrix}^T$$
$$= \begin{bmatrix} -2\Im_1 \\ \Im_1 - \Im_2 \\ 2\Im_2 \\ -\Im_2 + \Im_3 \\ -2\Im_3 \\ \Im_3 - \Im_4 \\ 2\Im_4 \\ \Im_1 - \Im_4 \\ 0 \end{bmatrix} \tag{A.4}$$

where $\Re_{(1,1)} = (\Re_s + 2\Re_{g_1}(t) + 2\Re_P + \Re_R)$,
$\Re_{(2,1)} = -(\Re_{g_1}(t) + \Re_P)$,
$\Re_{(2,2)} = (\Re_s + \Re_{g_1}(t) + \Re_{g_2}(t) + 2\Re_P + \Re_R)$,
$\Re_{(2,3)} = -(\Re_{g_2}(t) + \Re_P)$,
$\Re_{(2,9)} = -\Re_R$,
$\Re_{(3,2)} = (\Re_{g_2}(t) + \Re_P)$,
$\Re_{(3,3)} = (\Re_s + 2\Re_{g_2}(t) + 2\Re_P + \Re_R)$,
$\Re_{(3,4)} = -(\Re_{g_2}(t) + \Re_P)$,
$\Re_{(3,9)} = -\Re_R$,
$\Re_{(4,3)} = -(\Re_{g_2}(t) + \Re_P)$,
$\Re_{(4,4)} = (\Re_s + \Re_{g_3}(t) + \Re_{g_2}(t) + 2\Re_P + \Re_R)$,
$\Re_{(4,5)} = -(\Re_{g_3}(t) + \Re_P)$,
$\Re_{(4,9)} = -\Re_R$,
$\Re_{(5,4)} = -(\Re_{g_3}(t) + \Re_P)$,
$\Re_{(5,5)} = (\Re_s + 2\Re_{g_3}(t) + 2\Re_P + \Re_R)$,
$\Re_{(5,6)} = -(\Re_{g_3}(t) + \Re_P)$,
$\Re_{(5,9)} = -\Re_R$,
$\Re_{(6,5)} = -(\Re_{g_3}(t) + \Re_P)$,
$\Re_{(6,6)} = (\Re_s + \Re_{g_3}(t) + \Re_{g_4}(t) + 2\Re_P + \Re_R)$,
$\Re_{(6,7)} = -(\Re_{g_4}(t) + \Re_P)$,
$\Re_{(6,9)} = -\Re_R$,
$\Re_{(7,6)} = -(\Re_{g_4}(t) + \Re_P)$,
$\Re_{(7,7)} = (\Re_s + 2\Re_{g_4}(t) + 2\Re_P + \Re_R)$,
$\Re_{(7,8)} = -(\Re_{g_4}(t) + \Re_P)$,

$\Re_{(7,9)(t)} = -\Re_R,$
$\Re_{(8,1)} = -(\Re_{g_1}(t) + \Re_P),$
$\Re_{(8,7)} = -(\Re_{g_4}(t) + \Re_P),$
$\Re_{(8,8)} = (\Re_s + \Re_{g_1}(t) + \Re_{g_4}(t) + 2\Re_P + \Re_R),$
$\Re_{(8,9)} = -\Re_R,$
$\Re_{(9,1)} = -\Re_R,$
$\Re_{(9,2)} = -(\Re_R),$
$\Re_{(9,3)} = -\Re_R,$
$\Re_{(9,4)} = -\Re_R,$
$\Re_{(9,5)} = -\Re_R,$
$\Re_{(9,6)} = -\Re_R,$
$\Re_{(9,7)} = -\Re_R,$
$\Re_{(9,8)} = -\Re_R,$
$\Re_{(9,9)} = 8\Re_R.$

The flux through meshes 1, 2, 3 and 4 is of importance for this analysis. The mesh results obtained from the symbolic analysis are as follows,

$$\phi_k = G_{(k,l)}(t)\Im_1(t) + G_{(k,l)}(t)\Im_2(t) + G_{(k,l)}(t)\Im_3(t) + G_{(k,l)}(t)\Im_4(t) \tag{A.5}$$

where $G_{(k,l)}(t)$ is the gain due to the material reluctances, l is the l^{th} mesh which is investigated and k is the influence of the k^{th} mesh on the investigated mesh.